



Universiteit
Leiden
The Netherlands

Laser-generated toroidal helium plasmas

Kooij, V.L.

Citation

Kooij, V. L. (2021, April 28). *Laser-generated toroidal helium plasmas*. *Casimir PhD Series*. Retrieved from <https://hdl.handle.net/1887/3161377>

Version: Publisher's Version

License: [Licence agreement concerning inclusion of doctoral thesis in the Institutional Repository of the University of Leiden](#)

Downloaded from: <https://hdl.handle.net/1887/3161377>

Note: To cite this publication please use the final published version (if applicable).

Cover Page



Universiteit Leiden



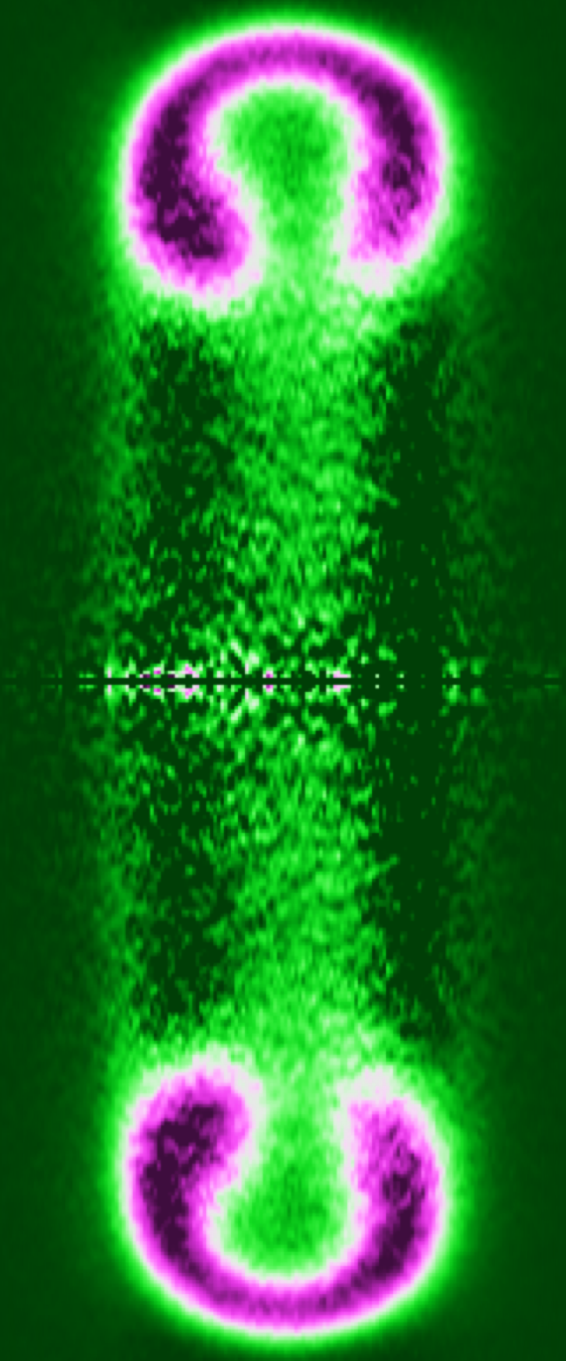
The handle <http://hdl.handle.net/1887/3161377> holds various files of this Leiden University dissertation.

Author: Kooij, V.L.

Title: Laser-generated toroidal helium plasmas

Issue date: 2021-04-28

Laser- generated toroidal helium plasmas



Vincent Kooij

Laser-generated toroidal helium plasmas

Proefschrift

ter verkrijging van
de graad van doctor aan de Universiteit Leiden,
op gezag van rector magnificus prof. dr. ir. H. Bijl,
volgens besluit van het college voor promoties
te verdedigen op woensdag 28 april 2021
klokke 16.15 uur

door

Vincent Laurens Kooij

geboren te Amsterdam
in 1975

Promotor: Prof. dr. D. Bouwmeester
Co-promotor: Dr. M.J.A. de Dood

Promotiecommissie: Prof. dr. P.J. Bruggeman (University of Minnesota, Minneapolis, USA)
Dr. W.A. Bongers (Dutch Institute for Fundamental Energy Research)
Prof. dr. E.R. Eliel
Prof. dr. M.P. van Exter

Casimir PhD series, Delft-Leiden 2021-01

ISBN 978-90-8593-467-7

An electronic version of this dissertation can be found at <https://openaccess.leidenuniv.nl>

This work has been made possible by financial support from the NWO Spinoza Prize awarded to prof. dr. D. Bouwmeester by the Dutch Research Council (NWO).

aan mijn ouders

Contents

Chapter 1	Introduction	9
Chapter 2	Generation and optical analysis of transient toroidal helium plasmas	13
2.1	Introduction	13
2.2	Experimental details	15
2.3	Toroidal plasma development	18
2.4	Numerical Abel inversion using transform techniques	26
2.5	Tomographic reconstruction and flow experiments	28
	Tomographic reconstruction	29
	Fluid flow visualisation	30
	Characteristic time scale	32
	Density of helium atoms in the centre of the toroidal plasma	34
	Flow experiment with a deliberately broken symmetry	36
	Plasma flow through a toroidal plasma	39
	Experiment with two closely spaced crossed breakdown plasmas	41
2.6	Oxygen impurity effects in helium plasma afterglows	41
2.7	Plasma kernel dynamics	45
2.8	Conclusion	49
Chapter 3	Shocks and successive laser pulse experiments	51
3.1	Introduction	51
3.2	Shocks and successive laser pulse experiments	52
3.3	Mach reflection and laser-induced breakdown plasmas	56
3.4	Conclusion	58
Chapter 4	Microwave analysis of transient toroidal helium plasmas	59
4.1	Introduction	59

4.2	Electromagnetic waves in plasma	61
	Plasma oscillations	61
	Drude-Lorentz model for electrical conductivity	62
	Electromagnetic waves in linear media	64
	Plasma complex permittivity and electromagnetic wave propagation	66
4.3	Microwave analysis of transient toroidal helium plasmas	68
	Examination of the microwave interferometer	69
	Microwave interferometric complex transmission measurements	74
	Full-wave finite-element complex transmission calculations	76
	Electron number density and electron collision rate determination	79
4.4	Conclusion	82
Chapter 5	Pulsed magnetron heating experiments on transient toroidal helium plasmas	85
5.1	Introduction	85
5.2	Design of the pulsed magnetron source	86
	The high-voltage magnetron pulser	87
	Integration of a microwave cavity into the plasma reactor	88
5.3	Pulsed magnetron heating experiments on transient toroidal helium plasmas	90
	Optical analysis of the pulsed magnetron heating experiments	90
	Characterisation of the pulsed magnetron source	94
5.4	Poloidal excitation temperature profile of transient toroidal helium plasmas	96
5.5	Conclusion and discussion	99
	Photographs of selected experimental set-ups	103
	Bibliography	107
	Samenvatting	117
	Curriculum Vitae	121
	Acknowledgements	123

1

Introduction

In just forty minutes, the amount of energy from the sun that strikes the earth is more than the annual energy consumption of the entire world.¹ This simple observation has been the sole motivator for the nuclear fusion endeavours of mankind. But half a century of devoted research efforts have not resulted in a reliable and break-even nuclear fusion power plant.

¹ Kopp et al. 2011; IEA 2017.

Still, nuclear fusion offers one of the possible answers to the quest for sustainable energy, which is widely considered to be one of the greatest challenges facing humanity in the forthcoming decades. Instrumental to nuclear fusion are plasmas with temperatures of the order of 100 million degrees Celsius, to allow thermonuclear reactions to take place. To sustain these thermonuclear reactions, the Lawson criterion² imposes a condition on the product of the plasma density n and the energy confinement time τ , as well as on the temperature. Plasma confinement is about satisfying this criterion, and the most prominent approach in contemporary nuclear fusion research is magnetic confinement fusion.

² F. F. Chen 1974, p. 281.

Soviet physicists already in the 1950s conceived the tokamak. These magnetic confinement devices employ strong magnetic fields to confine the high temperature plasma into the shape of a torus, and form the leading design for an economically viable nuclear fusion reactor.

Understanding the stability of magnetically confined plasmas is of fundamental importance to successful magnetic confinement fusion, and the topology of the confining fields proves to play a pivotal role.

The connection between stability and topology has been established in 1969, when Moffatt³ found that helicity—the quantity identified by Woltjer⁴ to be conserved in a plasma with infinite conductivity—is in fact a measure of the degree of linkage and knottedness of magnetic field lines.

³ Moffatt 1969.

⁴ Woltjer 1958.

Kamchatnov continued from the topological nature of this invariant, to construct a magnetic field configuration consisting of closed magnetic field lines that are all linked to each other.⁵ Therewith he obtained an analytical solution of the equations of magnetohydrodynamics,⁶ for an ideal incompressible fluid with infinite conductivity, describing a localized topological magnetic soliton.

The topological structure found by Kamchatnov was used by Rañada,⁷ and Irvine and Bouwmeester,⁸ to investigate linked and knotted beams of light, continued by Kedia et al.⁹ who found a set of analytical solutions to Maxwell's equations, whose electric and magnetic fields encompass all linked and knotted torus knots.¹⁰ This work was further expanded to optical vortices,¹¹ and linked and knotted gravitational radiation.¹²

Recently, the connection between stability and topology has been confirmed by magnetohydrodynamics simulations, demonstrating that a magnetic field with helicity reconfigures itself into a structure of foliated toroidal surfaces.¹³ These relaxed plasma configurations are not the familiar minimum energy configurations¹⁴ found by Taylor,¹⁵ but instead configurations where the magnetic pressure is balanced by the hydrostatic pressure.

These self-organising knotted magnetic structures are intrinsically stable and their configuration is essentially different from that of the tokamak. Namely, their hydrostatic pressure is minimal on the central circle of the foliated tori. The magnetic energy density of these knotted plasma structures is highly localised.

In the absence of electron and ion collisions, the tokamak conceived by the Soviet physicists should provide a stable plasma,¹⁶ yet experimentally the equilibrium is unstable and will lead to chaotic plasma dynamics. Mitigating these chaotic dynamics is instrumental in contemporary magnetic confinement fusion experiments.

However, instead of mitigating chaos, the self-organising knotted magnetic structures might intrinsically provide the sought after stability. Moreover, their apparent universality suggests that these equilibria may even emerge in astrophysical environments,¹⁷ alluding to a more fundamental importance.

Toroidal plasma structures have been observed in a vast range of experimental settings, including nanosecond discharges, laser ignition of flammable mixtures, high-power electric arcs, high-speed micro jets, and laser-induced breakdown plasmas.¹⁸ The research presented in this dissertation started with the observation of toroidal plasma structures

⁵ Kamchatnov 1982.

⁶ Magnetohydrodynamics studies the behaviour of electrically conducting fluids.

⁷ Rañada 1989.

⁸ Irvine et al. 2008.

⁹ Kedia et al. 2013.

¹⁰ A torus knot is a knot that lies on the surface of an unknotted torus.

¹¹ de Klerk et al. 2017.

¹² Thompson et al. 2014.

¹³ Smiet, Candelaresi et al. 2015.

¹⁴ The force-free configuration of minimum energy subject to conservation of helicity.

¹⁵ J. B. Taylor 1974.

¹⁶ F. F. Chen 1974, p. 285.

¹⁷ Smiet 2017; Smiet, de Blank et al. 2019.

¹⁸ Stepanyan et al. 2019; Dumitrache et al. 2017; Bradley et al. 2004; Bak, Im et al. 2014; Seward 2014; Gharib et al. 2017; Nassif et al. 2000; Harilal et al. 2015; Bak, Wermer et al. 2015

that are far more symmetrical than those reported in the aforementioned studies. These plasma structures were generated using laser-induced breakdown plasmas, created in quiescent atmospheric pressure helium gas at room temperature. Their self-confined toroidal nature, and atmospheric pressure ambient conditions, provide an interesting setting for investigating the numerically predicted,¹⁹ and intrinsically stable, self-organising knotted magnetic structures.

¹⁹ Smiet, Candelaresi et al. 2015.

The long-term objective is the realisation of such self-organising knotted magnetic structures in the laboratory. This dissertation is an account of the first steps towards this goal, discussing the prime features responsible for the development of the laser-generated toroidal helium plasmas, along with their prime plasma parameters. Furthermore, the research on counteracting the transient nature of these toroidal plasmas is discussed, a property that evidently hinders the realisation of the self-organising magnetic structures.

The research starts off in chapter 2, where for the entire evolution of a toroidal plasma, tomographically reconstructed, poloidal radiant intensity profiles are presented that clearly visualise the formative fluid flow of the toroidal structure. These observations also reveal a new splitting of the toroidal plasma during the final phase of its evolution. Based on elementary thermodynamic principles, a model is developed that establishes a characteristic time scale at which structure is expected to form. This time scale is confirmed by measurements of the density of helium atoms in the centre of the toroidal plasma. By deliberately breaking the symmetry of the flow responsible for the development of the toroidal structure, the model for the formation of this structure is confirmed. The pulsating plasma observed at the beginning of the creation of a laser-induced breakdown plasma is discussed last. This repeating dynamics possibly contributes to the formation of the two-lobe structure visible in the plasma kernel.

In chapter 3, a novel interpretation of high-speed Schlieren images is presented, where a Mach reflection of shocks is visible, formed by the two-lobe plasma kernel of a laser-induced breakdown plasma. The enhanced strength of this shock is linked to the asymmetrical fluid flow necessary for the development of a toroidal plasma. The propagation of the shock is directly visualised by a novel technique, whereby a second laser-induced breakdown plasma is used as a probe. With this technique, the existence of a low density cavity, formed in the wake of the shock, is also confirmed.

Chapter 4 addresses the plasma parameters of the toroidal helium

plasmas. By combining interferometric measurements using 57 GHz microwave radiation with detailed full-wave finite-element calculations, the electron number density and the electron collision rate are estimated for the entire evolution of a toroidal plasma. The microwave interferometric set-up used to measure the complex transmission coefficient is discussed in detail. Furthermore, a method is described, in which the finite-element calculations are used as a map between the measured transmission coefficient and the desired plasma parameters. In support, a number of fundamental concepts from plasma physics are reviewed.

To counteract the transient nature of the toroidal helium plasmas, a sub-microsecond rise time 1.75 kW pulsed magnetron source has been designed, for which the detailed design is presented in chapter 5. This magnetron source has been used in preliminary experiments aimed at heating the plasma by absorption of microwave radiation. During these experiments, the electrical characteristics of the magnetron source have been determined. The toroidal plasma is subjected to a high power 2.460 GHz microwave pulse, a frequency commonly used for industrial microwave sources. To apply the microwave pulse to the toroidal plasma, a 2.465 GHz iris coupled rectangular microwave cavity has been designed. The shift in frequency of 5 MHz anticipates on the detuning of the cavity due to the presence of plasma. The effect of the microwave pulse on the toroidal plasma, as well as the dark space that is observable between the microwave generated plasma and the toroidal plasma, are discussed. Finally, a poloidal excitation temperature profile of the toroidal plasma, including the additional plasma structure generated by the microwave pulse, is presented. This temperature profile has been determined by applying a standard Boltzmann analysis to two, tomographically reconstructed, poloidal radiant intensity profiles, obtained from images recorded at two different wavelengths.

Most images presented in this work have been captured through a 10 nm bandpass filter, enclosing one (or a multiplet) of the atomic helium emission lines, in order to facilitate quantitative analyses.

At the end of this dissertation, [photographs](#) have been included, to give a more vivid impression of selected experimental set-ups used for our research.

Lastly, it is noted that the electronic version of this dissertation provides [hyperlinks](#), recognisable by their purple coloured text.

Generation and optical analysis of transient toroidal helium plasmas

We experimentally studied laser-generated, atmospheric pressure, transient toroidal helium plasmas. For the entire evolution of these toroidal plasmas, we present tomographically reconstructed, poloidal radiant intensity profiles, that clearly visualise the formative fluid flow. A new splitting of the toroidal plasma is observed during the final phase of its evolution. We present a model based on elementary thermodynamic principles that establishes a characteristic time scale at which structure is expected to develop, supported by measurements of the density of helium atoms in the centre of the toroidal plasma. We report on the repeated creation of plasma observed during the creation of a laser-induced breakdown plasma, which possibly contributes to the formation of the two-lobe structure visible in its plasma kernel. We briefly touch upon a possible application of the laser-generated toroidal helium plasmas in the study of self-organising knotted magnetic structures.

2.1 Introduction

In contemporary nuclear fusion research, magnetic confinement fusion is generally regarded as the most prominent approach. Understanding the stability of these magnetically confined plasmas is therefore of fundamental importance, and the topology of the confining fields proves to play a pivotal role.

The connection between stability and topology has been established in 1969, when Moffatt found that helicity, the quantity identified by Woltjer to be conserved in a plasma with infinite conductivity,¹ is in fact a measure of the degree of linkage and knottedness of magnetic field lines.²

Recently, the connection between stability and topology has been confirmed by magnetohydrodynamics simulations, demonstrating that an initially helical magnetic field reconfigures itself into a configuration

The work presented in this chapter is in preparation for publication in the *Journal of Plasma Physics*.

¹ Woltjer 1958.

² Moffatt 1969.

³ Smiet, Candelaresi et al. 2015.

of foliated toroidal surfaces.³ These self-organising knotted magnetic structures are intrinsically stable, and their configuration is essentially different from that of a tokamak, in that their hydrostatic pressure is minimal on the central circle of the foliated tori. The magnetic energy density of these knotted plasma structures is highly localised.

⁴ Stepanyan et al. 2019; Dumitrache et al. 2017; Bradley et al. 2004; Bak, Im et al. 2014; Seward 2014; Gharib et al. 2017; Nassif et al. 2000; Harilal et al. 2015; Bak, Wermer et al. 2015.

As already mentioned in the introduction of this dissertation, toroidal plasma structures have been observed in a vast range of experimental settings, including nanosecond discharges, laser ignition of flammable mixtures, high-power electric arcs, high-speed micro jets, and laser-induced breakdown plasmas.⁴ In the course of our earlier exploratory investigations using laser-induced breakdown plasmas, we observed toroidal plasma structures that are far more symmetrical than those reported in the aforementioned studies.

An example of the development of these toroidal plasmas, generated in quiescent atmospheric pressure helium gas at room temperature, is presented in figure 2.1. Their self-confined toroidal nature and atmospheric pressure ambient conditions provide an interesting setting for investigating the numerically predicted and intrinsically stable self-organising knotted magnetic structures in plasma.⁵

⁵ Smiet, Candelaresi et al. 2015.

In this chapter we investigate the prime features responsible for the development of these laser-generated toroidal helium plasmas. We present tomographically reconstructed, poloidal radiant intensity profiles, for the entire evolution of a toroidal plasma, with which the formative fluid flow is clearly visualised. A new splitting of the toroidal

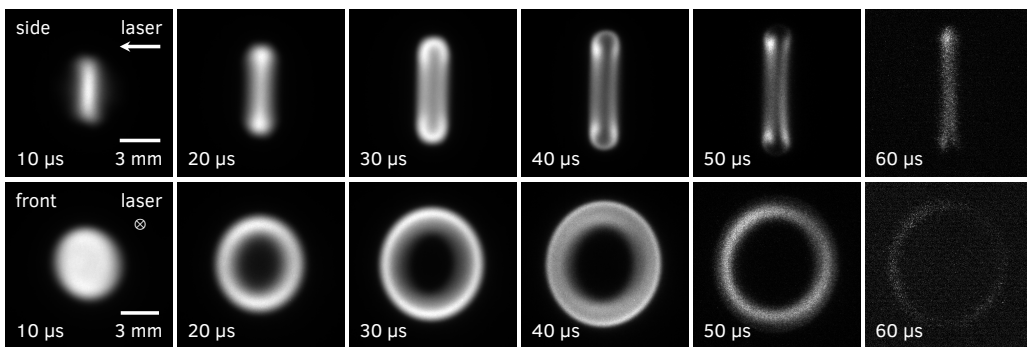


Figure 2.1: Development of a toroidal plasma due to a single laser-induced breakdown plasma, generated in quiescent atmospheric pressure helium gas at room temperature. Side view images (top row) and front view images (bottom row) have been captured at increasing times (left to right) after the breakdown laser pulse. All images have been averaged over 50 exposures and captured through a 10 nm bandpass filter with a centre wavelength of 590 nm. The front view images show slightly oval plasma structures due to a necessary skewed viewing direction. All images have been individually normalised to their maximum intensity to respect the large dynamic range in intensity of the entire development. See section 2.3 for further experimental details.

plasma is observed during the final phase of its evolution.

The characteristic time scale observed in the development of the toroidal plasma will be explained by an intuitive model based on elementary thermodynamic principles. The time scale thus obtained is supported by the evolution of the density of helium atoms in the centre of the toroidal plasma, measured with the use of a second laser-induced breakdown plasma.

An essential element in the development of the toroidal plasmas is the symmetric repletion of a low density cavity, generated in the wake of the shock formed by a laser-induced breakdown plasma. In support, we present flow experiments where the symmetrical experimental setting is deliberately broken, and analyse the resulting fluid flow using tomographically reconstructed, poloidal radiant intensity profiles.

We briefly discuss the repeated creation of plasma observed during the creation of a laser-induced breakdown plasma. These repeating dynamics possibly contributes to the formation of the two-lobe structure visible in the plasma kernel.

2.2 Experimental details

A simplified schematic⁶ of the pulsed high power optical set-up used in the presented experiments is shown in figure 2.2. Two Q-switched Nd:YAG lasers (Quanta-Ray GCR-3 and Continuum NY61-10) provide

⁶ For a more lively impression of the experimental set-up we refer to photo 1 on page 103.

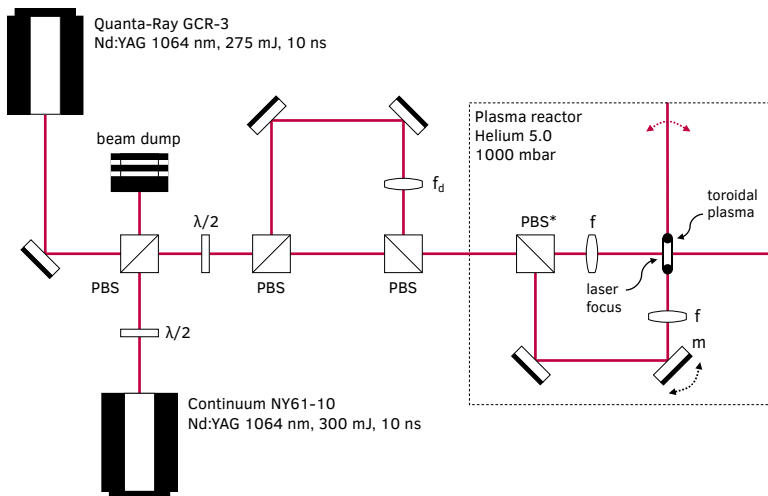


Figure 2.2: Simplified schematic of the pulsed high power optical set-up. PBS: polarising beam splitter, PBS^{*}: removable polarising beam splitter, $\lambda/2$: half-wave plate, f : focusing lens, f_d : lens to slightly displace the focus inside the plasma reactor, m : rotating mirror. For a more lively impression of the experimental set-up we refer to photo 1 on page 103.

high power laser pulses with a wavelength of 1064 nm, a temporal pulse length of approximately 10 ns, and a beam width of 8 mm. The pulse energy is adjustable between 0 and 275 mJ (or 300 mJ for the Continuum NY61-10) which is accomplished by routing the laser pulse through two attenuators (not shown) each consisting of a half-wave plate and a polarising beam splitter. The laser pulse energy is measured using a laser power meter (Ophir Nova II and PE50BF-C) just before entering the plasma reactor.

Particular experiments demand successive laser pulses to be generated with intervals as short as a few tens of nanoseconds. This can be accomplished by using both lasers simultaneously and combining their laser beam paths. This is achieved by rotating the polarisation of the laser pulses from one laser by 90° using a half-wave plate and combining both pulses using a polarising beam splitter. The combined beam path carries horizontally polarised (p-polarised) laser pulses from the Quanta-Ray laser and vertically polarised (s-polarised) laser pulses from the Continuum laser.

Before the laser pulses enter the plasma reactor, the combined beam path is split and recombined again, to provide a means of modifying the vertically polarised laser pulses, just before they enter the plasma reactor (see figure 2.2). In section 2.5, this possibility is used to slightly displace the focus of the vertically polarised laser pulses inside the plasma reactor, with respect to the focus of the horizontally polarised laser pulses, using a diverging plano-concave lens f_d with a focal length of 2 m. With this adjustment, it is possible to simultaneously create two closely spaced plasmas and study the effect they have on each other.

Inside the plasma reactor, the laser pulses are focused into quiescent atmospheric pressure 5.0 grade helium gas using a 1" plano-convex lens with a focal length of 50 mm (Thorlabs LA1131-YAG) to produce a laser-induced breakdown plasma.

For experiments visualising shocks using a second laser-induced breakdown plasma,⁷ a removable polarising beam splitter inside the plasma reactor is used to split-off the vertically polarised laser pulses, which are subsequently focused at a 90° angle with respect to the original beam path (see figure 2.2). This angle can be adjusted slightly using a piezoelectric inertia actuator, making it possible to use one laser to scan through a plasma created earlier using the other laser.

The Q-switch and flash lamp trigger signals for both lasers are generated by a digital delay generator (Stanford Research Systems DG645) and an in-house designed FPGA (field-programmable gate array) based reconfigurable pulse generator. The flash lamps operate

⁷ These experiments will be presented in chapter 3.

at a repetition rate of 10 Hz while the Q-switches operate at a reduced repetition rate of 2.5 Hz.

The radiant intensity⁸ of the plasma decreases orders of magnitude during its evolution from a laser-induced breakdown plasma to the final toroidal plasma. When studying the toroidal plasma, emission from the initial and very bright breakdown plasma can cause artefacts in the recorded images. The reduced repetition rate minimises unnecessary emission leaking through the MCP (micro-channel plate⁹) of the ICCD (intensified CCD) camera (Princeton Instruments PI-MAX 512) while attaining the maximum possible image capture rate.

The ICCD camera receives a trigger from the digital delay generator before the Q-switch is triggered, so that it is possible to image the onset of a laser-induced breakdown plasma.

The digital delay generator also generates a trigger signal for a 1 GHz bandwidth oscilloscope (LeCroy LT584L) used for precise timing analysis, and for recording the temporal profile of the laser pulse and plasma emission using a 150 ps rise time Si photo detector (Thorlabs DET025AFC). The timing resolution of the integral set-up for plasma creation and observation is approximately 4 ns.

The imaging set-up (not shown) consists of two achromatic 4f lens configurations¹⁰ (Thorlabs AC508-300-A and AC508-400-A) capable of simultaneously imaging the side and front view of the toroidal plasma by combining both views through a 50/50 non-polarising beam splitter. The front view is necessary skewed by approximately 26° to avert blocking of the high power laser beam by the imaging optics.

The images recorded by the ICCD camera are single shot. During an experiment, plasma is repeatedly created, and every recorded image is captured from a distinct plasma. Due to small fluctuations visible in the single shot images, and to increase the signal to noise ratio, most images presented in this work have been averaged over 50 repetitions.

All images used for quantitative analysis are corrected for flat field, background emission, dark frame, and bias frame. The background correction is performed using the edge columns of the recorded image as a reference, to simultaneously correct for both stray light and diffuse reflections from within the imaging system.

The necessity to perform a flat field correction is nicely illustrated in figure 2.3, where we can see that our flat field image exhibits variations as large as 15%. The honeycomb structure that is visible throughout the image is not unique to our camera, and has been reported previously¹¹ in the literature.

To illustrate the effect of the flat field correction on quantitative

⁸ Radiant intensity is defined as the energy emitted per unit time per unit solid angle.

⁹ A micro-channel plate is closely related to an electron multiplier. In ICCD cameras it acts as image intensifier and nanosecond time scale shutter.

¹⁰ A 4f lens configuration consists of two identical lenses sharing one focal plane (also called the Fourier plane) and provides unit magnification.

¹¹ Williams et al. 2007.

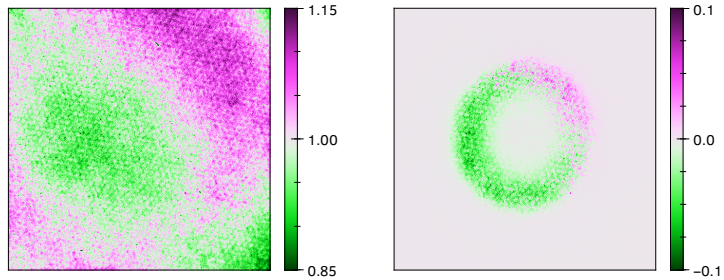


Figure 2.3: (left) Flat field image of our ICCD camera shown in false colour. Note the honeycomb structure that is visible throughout the image. (right) For a typical image of a toroidal plasma, this image shows the difference between the original and flat field corrected image, normalised to the maximum intensity of the original image.

measurements, figure 2.3 shows, for a typical image of a toroidal plasma, the difference between the original and flat field corrected image, normalised to the maximum intensity of the original image. It is clear that variations of up to 10% can be observed.

Imaging the extensive range of radiant intensities of the plasma during its evolution from a laser-induced breakdown plasma to the final toroidal plasma, is accomplished by attenuating the plasma emission using neutral density filters, rather than changing the gain or exposure time of the ICCD camera. This averts possible non-linear behaviour of the ICCD camera contaminating the quantitative measurements.

Density gradients in the helium gas can be visualised¹² using a high-speed Schlieren¹³ imaging system, consisting of a low-power 4 mW collimated 632.8 nm helium-neon laser beam (Uniphase 1121P), and a knife edge positioned at the shared focal plane of the 4f lens system used for imaging the side view of the toroidal plasma. A laser line filter (Thorlabs FL632.8-10) has been used to block most plasma emission. The remaining emission that is still visible through the laser line filter is corrected by subtracting images that have been captured while the helium-neon laser was switched off.

2.3 Toroidal plasma development

The observed self-organising toroidal plasmas emerge solely due to a single laser-induced breakdown plasma, created in quiescent atmospheric pressure helium gas at room temperature. These toroidal structures are plasma afterglows¹⁴ despite the fact that they exhibit intricate structure. This section presents an overview of the evolution leading to these plasma structures. A more detailed description of the prime features will be presented in the following sections.

¹² These experiments will be presented in chapter 3.

¹³ See for a treatise on Schlieren imaging Settles 2001 and references therein.

¹⁴ A plasma afterglow is the radiation emitted from a cooling plasma when the source of ionisation is removed.

In figures 2.4–2.6 the evolution of a single laser-induced breakdown plasma for a laser pulse energy of 250 mJ is presented.¹⁵ These plasmas have been created in quiescent 5.0 grade helium gas at a pressure of 1002 mbar, using a 1" plano-convex lens with a focal length of 50 mm. The images have been recorded using an ICCD camera viewing the plasma orthogonal to the laser propagation direction (side view) and from a slight angle with respect to the laser propagation direction (front view) as explained in section 2.2. Due to the necessary skewed viewing direction, the front view images show slightly oval plasma structures.

All images have been recorded using a fixed gate width of 250 ns and a fixed gain of 255, to avert possible non-linear behaviour of the ICCD camera contaminating the quantitative measurements. Because during its evolution the radiant intensity of the plasma decreases orders of magnitude (see figures 2.7 and 2.9) neutral density filters have been used to attenuate the plasma emission to avert overexposure of the ICCD camera. Overlapping series of images have been recorded, which later have been glued together to obtain a single series of images spanning the complete evolution of the plasma. This is illustrated in figure 2.7, where different series for a given laser pulse energy are alternately represented by line segments and markers. Because the least intense sequences have been recorded without a neutral density filter, series of different laser pulse energies can be compared with each other. Moreover, all images presented in this work have been individually normalised to

¹⁵ Similar evolution is observed for pulse energies of 50, 100, and 200 mJ. Although this work primarily reports on plasmas created with a pulse energy of 250 mJ, this section also presents measurements of the spectral radiant intensity and linear dimensions for plasmas created with a pulse energy of 50, 100, and 200 mJ, and reports on the similar morphology of toroidal plasmas generated with different pulse energies.

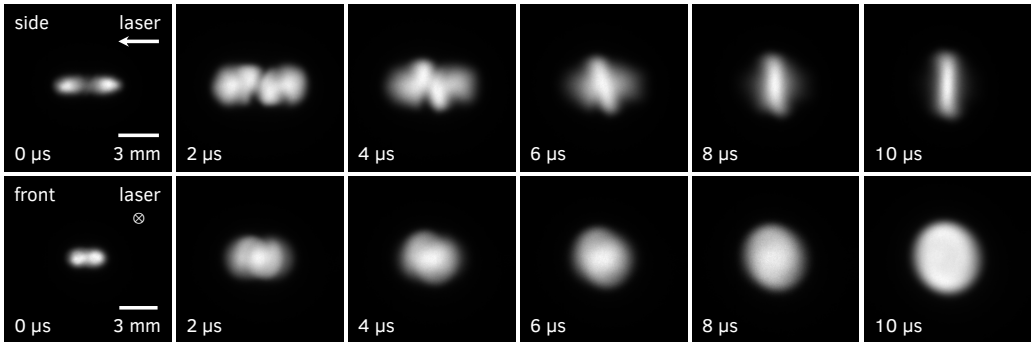


Figure 2.4: First part (0–10 μ s) of the development of a toroidal plasma due to a single laser-induced breakdown plasma created in quiescent atmospheric pressure helium gas at room temperature. Side view images (top row) and front view images (bottom row) have been captured at increasing times (left to right) after the breakdown laser pulse. All images have been averaged over 50 exposures and captured through a 10 nm bandpass filter with a centre wavelength of 590 nm. The front view images show slightly oval plasma structures due to a necessary skewed viewing direction. All images have been individually normalised to their maximum intensity to respect the large dynamic range in intensity of the entire development. Laser pulse energy: 250 mJ, focal length focussing lens: 50 mm, gas pressure: 1002 mbar, ICCD camera gate width: 250 ns.

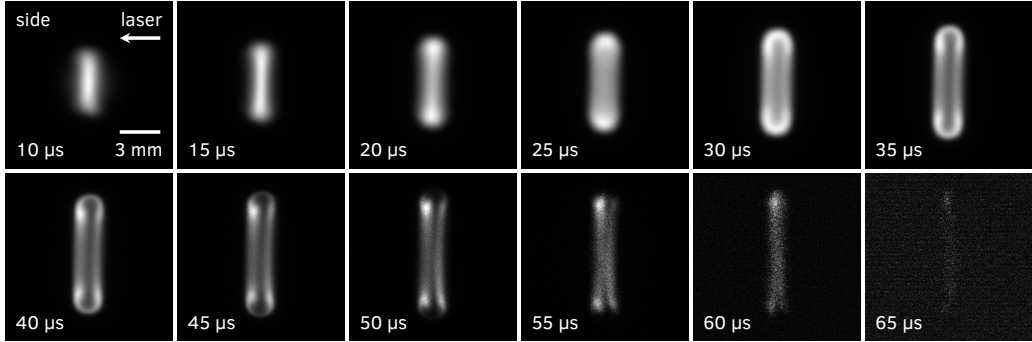


Figure 2.5: Development and subsequent dissolution of a toroidal plasma due to a single laser-induced breakdown plasma. Side view images have been captured at increasing times (left to right, top to bottom) after the breakdown laser pulse. Note that all images have been individually normalised to their maximum intensity to respect the large dynamic range in intensity of the entire development. The images are a continuation of the development presented in figure 2.4 and have been captured using identical experimental settings as those presented there.

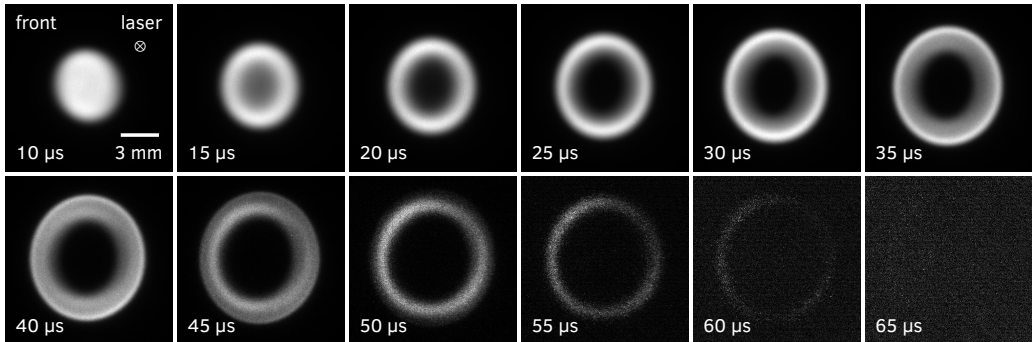


Figure 2.6: Development and subsequent dissolution of a toroidal plasma due to a single laser-induced breakdown plasma. Front view images have been captured at increasing times (left to right, top to bottom) after the breakdown laser pulse. The images show slightly oval plasma structures due to a necessary skewed viewing direction. Note that all images have been individually normalised to their maximum intensity to respect the large dynamic range in intensity of the entire development. The images are a continuation of the development presented in figure 2.4 and have been captured using identical experimental settings as those presented there.

their maximum intensity to respect the large dynamic range in intensity of the entire development.

The self-organising toroidal plasmas are alike most laboratory plasmas¹⁶ in the sense that they are optically thin¹⁷ and exhibit a line spectrum.¹⁸ Preliminary high-speed spectra recorded using a prism spectrograph coupled to the imaging system of the ICCD camera have shown that most emission originates from neutral atomic helium. In order to facilitate quantitative analysis all images therefore have been captured through a 10 nm bandpass filter with a centre wavelength of 590 nm (Thorlabs FB590-10). This bandpass filter encloses the atomic helium emission lines at 587.6 nm originating from the $1s3d^3D-1s2p^3P$ multiplet transitions.¹⁹ Moreover, to block out-of-band emission a 750 nm short-pass filter (Thorlabs FESH0750) has been used.

It has been noted that all images recorded by the ICCD camera are captured from independent laser-induced breakdown events. The gradual development of the images presented in figures 2.4–2.6 shows

¹⁶ Cooper 1966, pp. 37, 41; Hutchinson 2002, pp. 221–222, 252.

¹⁷ Rybicki et al. 1979, pp. 12–14; Cooper 1966, pp. 41, 90.

¹⁸ Hutchinson 2002, p. 252; Smerlak 2011; Rybicki et al. 1979, p. 17; Schregel et al. 2016; Carbone et al. 2016.

¹⁹ Kramida et al. 2019.

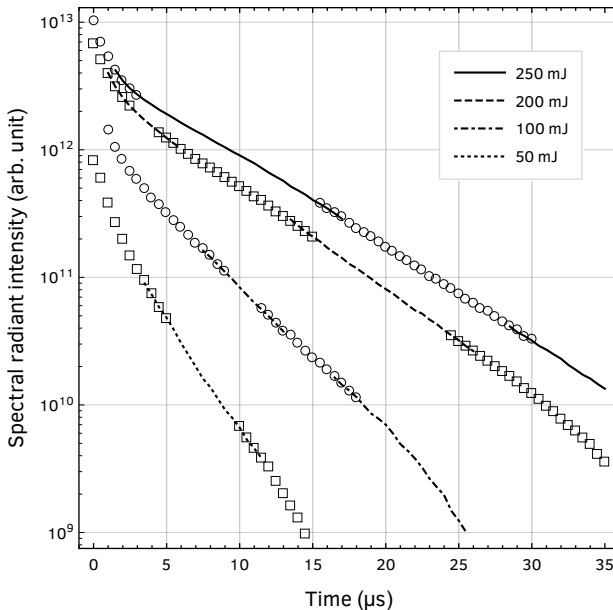


Figure 2.7: Spectral radiant intensity of a laser-induced breakdown plasma created with a pulse energy of 50, 100, 200, and 250 mJ. Overlapping series of images have been recorded, that later have been glued together to obtain a single series of images spanning the complete evolution of the plasma. This graph shows the overlapping series of recordings for a given laser pulse energy, alternately represented by line segments and markers. Note the different time span compared to figure 2.9. This graph is based on the same recordings as those used for figures 2.4–2.6.

that the plasma evolution is very reproducible. Due to small fluctuations visible in the single shot images, and to increase the signal to noise ratio, most notably during the faint afterglow, all images have been averaged over 50 repetitions.

The evolution visible in figures 2.4–2.6 clearly shows the emergence of a toroidal plasma structure from 10 μs onward. Previous laser-induced breakdown studies have reported similar plasma structures,²⁰ most notably in nitrogen and air. Likewise, recent studies on laser ignition of flammable alkane-air mixtures reported the emergence of toroidal flame kernels.²¹

An almost perfect plasma torus²² has been formed around 20 μs , which is seen to evolve into an eroded toroid prior to splitting into two halves. This is a new observation and a strong indication that, although the emerged plasma structure is of toroidal nature, it does not exhibit vorticity like the well-known vortex rings²³ or the structures reported in previous studies.²⁴

A probable explanation is the symmetry of the breakdown plasma. In figure 2.4 one can see that our laser-induced breakdown plasma at 0 μs exhibits a two-lobe structure which is highly symmetrical with respect to the focal plane. Numerical studies on the fluid dynamical effects of laser energy deposition show²⁵ that the generation of vorticity found in these systems stems from the asymmetrical tear-drop shape of the breakdown plasma. This suggests that our highly symmetrical breakdown plasma inhibits the generation of vorticity in our toroidal plasma. In section 2.5 a three-dimensional tomographic reconstruction of the plasma will be presented that visualises the symmetrical fluid flow responsible for the emergence of the toroidal structure.

It has been noted that the two-lobe structure of our breakdown plasma does not concord with the cited studies on laser-induced breakdown plasmas. However, they have been reported in recent studies on the onset and dynamics of plasma kernels.^{26,27}

Another marked difference between the presented evolution and the cited laser-induced breakdown studies is the characteristic time scale. In our experiment, after 20 μs , an almost perfect plasma torus has been formed, whereas in the cited studies this takes much longer. For example, in Harilal²⁸ where toroidal structures of similar size in air are studied, this occurs after 50 μs .

An intuitive explanation can be found in the density dependence of the speed of sound in gasses. Because the speed of sound in a gas and the mean speed of its constituents are of the same order of magnitude²⁹ it is tenable that they dictate how fast density variations equilibrate. For

²⁰ Nassif et al. 2000; Harilal et al. 2015; Bak, Wermer et al. 2015.

²¹ Dumitrache et al. 2017; Bradley et al. 2004; Bak, Im et al. 2014.

²² At this point it is well to distinguish between a toroid, a surface or solid formed by rotating a closed curve about a line which lies in the same plane but does not intersect it, and a torus, in which the closed curve is a circle.

²³ Akhmetov 2009.

²⁴ Dumitrache et al. 2017; Nassif et al. 2000; Harilal et al. 2015; Bradley et al. 2004.

²⁵ Ghosh et al. 2008; Morsy et al. 2002.

²⁶ Nishihara et al. 2018; Alberti, Munafò, Pantano et al. 2019a.

²⁷ In section 2.7 plasma kernel dynamics and the two-lobe structure will be addressed in more detail.

²⁸ Harilal et al. 2015.

²⁹ Jeans 1940, p. 57.

an ideal gas, the speed of sound is given by³⁰

$$c = \sqrt{\gamma \frac{p}{\rho}}$$

where p is the pressure, ρ the mass density, and γ the (constant) ratio of specific heats c_p/c_v . Substitution of tabulated values³¹ at standard temperature and pressure³² reveals that the speed of sound in helium is 2.9 times higher than in air, which is in agreement with our observations. In section 2.5 we will present an intuitive model and derive the observed time scale from elementary thermodynamic principles.

The evolution presented in figures 2.4–2.6 reveals the emergence of features in common with earlier reported laser-induced breakdown studies.³³ These can be summarised as follows.

0 μs — A laser-induced breakdown plasma has been created due to the avalanche ionisation of the helium gas. Multi-photon ionisation provides the initial seed electrons necessary to ignite the avalanche³⁴. Subsequent inverse bremsstrahlung absorption heats³⁵ the plasma, creating a high pressure and high temperature plasma kernel whose rapid expansion leads to the formation of a shock.³⁶

1 μs — The plasma kernel continues to expand, while the shock detaches from the kernel and propagates into the quiescent ambient gas, creating a low density cavity in its wake. The shock is not visible in the presented images. See section 3.2 for high-speed Schlieren images visualising the shock up to 4 μs.

2–8 μs — The plasma is squeezed in longitudinal direction (see linear dimensions shown in figure 2.8) due to gas flowing back to the plasma kernel along the symmetry axis. While the plasma is compressed in longitudinal direction it continues to expand in the transverse direction.

10 μs — A plasma pillbox has been formed due to the longitudinal compression and the evolution enters a more quiescent phase.

20 μs — An almost perfect plasma torus has emerged. The flow returning along the symmetry axis squeezed a hole into the plasma pillbox. The plasma torus is approximately 6.5 mm in diameter and 2 mm thick (see figure 2.8) for a laser pulse energy of 250 mJ.

30–40 μs — Due to our highly symmetrical breakdown plasma, the squeezing flow approaches the plasma from both sides equally. These flows will collide in the centre of the torus and expand into a plane orthogonal to the symmetry axis, pushing the plasma outward.³⁷ The plasma torus evolves into a deformed and eroded toroidal plasma.

50 μs — The flow deforming and eroding the toroidal plasma continues and dissects the toroidal plasma into two halves.

³⁰ Landau et al. 1987, p. 318.

³¹ Haynes 2014.

³² Standard temperature and pressure is defined as 273.15 K and 10⁵ Pa.

³³ Nassif et al. 2000; Harilal et al. 2015; Bak, Wermer et al. 2015.

³⁴ Raizer 1991, p. 155.

³⁵ Miziolek et al. 2006, p. 171.

³⁶ Y. Chen et al. 2000; Harilal et al. 2015; Ghosh et al. 2008.

³⁷ See section 2.5 for a three-dimensional tomographic reconstruction of the plasma visualising these flows.

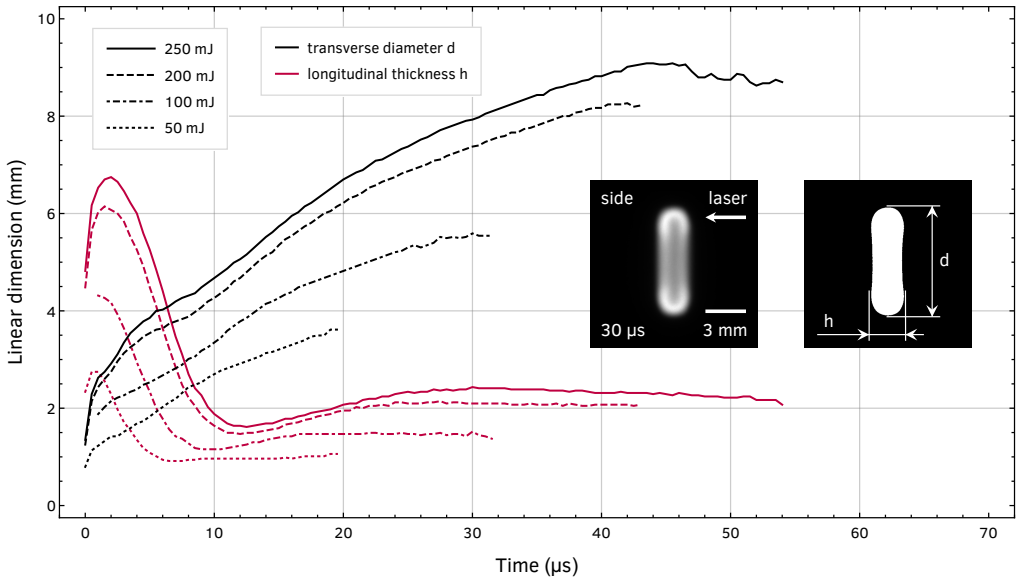


Figure 2.8: Linear dimensions of a laser-generated toroidal plasma for laser pulse energies of 50, 100, 200, and 250 mJ. This graph shows the transverse diameter (orthogonal to the laser propagation direction) and longitudinal thickness of the axis-oriented smallest bounding box of the side view images after binarisation by cluster variance maximization (Otsu’s algorithm). The inset shows a typical toroidal plasma and its binarised image together with the definitions for transverse diameter and longitudinal thickness. This graph is based on the same recordings as those used for figures 2.4–2.6.

60 μs — The toroidal plasma dissolves and is no longer visible. This does not necessarily mean that a quiescent state has been reached, gas flow may still be present.

³⁸ Spectral radiant intensity is defined as the energy emitted per unit time per unit solid angle per unit wavelength.

The spectral radiant intensity³⁸ of the plasma during its evolution is presented in figure 2.9. As noted in the beginning of this section, the quantitative measurements have been captured through a bandpass filter enclosing the atomic helium emission lines at 587.6 nm. It is remarkable, considering the huge change in size and morphology of the plasma, that the radiant intensity decreases purely exponentially. Moreover, two exponential sections can be observed, where the second section is decreasing even faster than the first. In section 2.5 we link this increase in the exponential decay rate to the restored density in the surrounding area of the toroidal plasma.³⁹

³⁹ Oxygen impurities due to the contamination of our plasma reactor also affects the decay rate. See section 2.6 for details.

To conclude this section, we present in figure 2.10 a series of images showing that the generation of a toroidal plasma is robust over a wide range of laser pulse energies. We presumed that a comparable moment in the evolution of a toroidal plasma is the intersection of the two fitted

exponential sections of the spectral radiant intensity shown in figure 2.9. The similar morphology of the images at these moments confirms that this intersection is indeed a comparable moment in the evolution of a toroidal plasma. The apparent relation between laser pulse energy and time will become clearer in section 2.5.

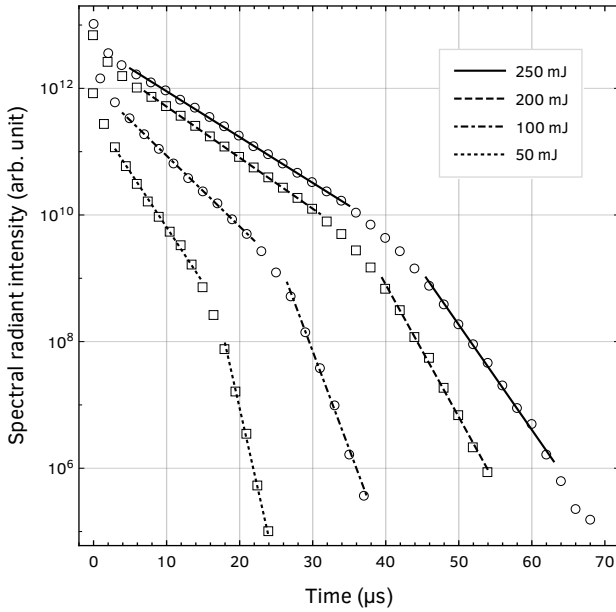


Figure 2.9: Spectral radiant intensity of a laser-induced breakdown plasma created with a pulse energy of 50, 100, 200, and 250 mJ. Measurements have been recorded at a 500 ns interval but for clarity fewer are shown (markers). Purely exponential decay is visible for both sections of the spectral radiant intensity curve. Each section has been fitted to an exponential (line segments). Note the different time span compared to figure 2.7. This graph is based on the same recordings as those used for figures 2.4–2.6.

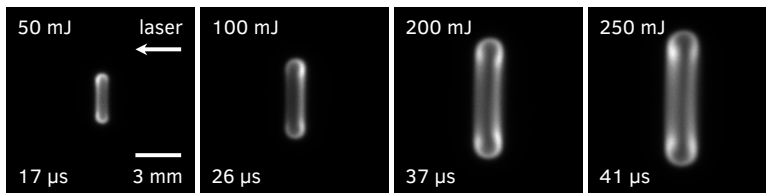


Figure 2.10: Toroidal plasmas generated with a pulse energy of 50, 100, 200, and 250 mJ. The images show that the generation of a toroidal plasma is robust over a wide range of laser pulse energies. The images are from a comparable moment in the evolution of a toroidal plasma (see text for details) and are based on recordings captured using similar experimental settings as those presented in figures 2.4–2.6.

2.4 Numerical Abel inversion using transform techniques

In the previous section we presented a self-organising toroidal plasma emerging solely due to a single laser-induced breakdown plasma. We attributed the generation of this toroidal structure to fluid flow along the symmetry axis of the plasma. Useful for the visualisation of this fluid flow is a three-dimensional tomographic reconstruction of the toroidal plasma. This section presents a novel numerical method, based on transform techniques for the Abel inversion,⁴⁰ that will be used to perform this reconstruction.

⁴⁰ Hutchinson 2002, p. 141; Hanson 1993; Dribinski et al. 2002; Pretzler et al. 1992; Smith et al. 1988.

A three-dimensional tomographic reconstruction is feasible because of two characteristics of our toroidal plasma that are helpful to us. It has been noted before that our toroidal plasmas are optically thin plasmas. This means that the observations we make, and the images we record, are two-dimensional projections of the three-dimensional toroidal plasma. Moreover, if we concentrate on the side view images, recorded orthogonal to the symmetry axis of the toroidal plasma, we can appreciate the fact that these images are projections of an axially symmetric object, owing to the symmetrical nature of our experiment. These characteristics provide the necessary conditions⁴¹ to employ Abel inversion and obtain a three-dimensional tomographic reconstruction.

⁴¹ Cooper 1966, p. 96.

If we assume that the symmetry axis is oriented horizontally with respect to the recorded images, each column of these images originates from the projection of a slice through the toroidal plasma, obtained orthogonal to its symmetry axis.

Let the symmetry axis coincide with the z-axis and let $f(x, y, z)$ be the radiant intensity distribution. Then axial symmetry implies

$$f(x, y, z) = f(r, z)$$

where $f(r, z)$ represents the poloidal radiant intensity profile of our toroidal plasma (see figure 2.11), $r^2 = x^2 + y^2$, and z labels the aforementioned slice through the toroidal plasma. The projection $p(x, z)$ of the toroidal plasma onto the x-axis is given by



Figure 2.11: Schematic of the poloidal plane of a toroidal object (shown as a torus) as used in this work.

$$p(x, z) = \int_{-\infty}^{\infty} f(x, y, z) dy$$

or, using axial symmetry, by

$$p(x, z) = 2 \int_{|x|}^{\infty} f(r, z) \frac{r}{\sqrt{r^2 - x^2}} dr \tag{2.1}$$

⁴² Cooper 1966, p. 96–97; Abel 1826; Arfken et al. 1995, p. 929.

which is the Abel transform⁴² of $f(r, z)$. Note that the projection $p(x, z)$

represents the side view image recorded by our ICCD camera. In order to reconstruct the poloidal radiant intensity profile $f(r, z)$ we need to invert, for every slice z , the projection $p(x, z)$.

Let $p(x, z) \equiv p(x) \equiv p$ and $f(r, z) \equiv f(r) \equiv f$ to emphasise that the inversion is performed slicewise and let \hat{A} be the Abel transform operator. Then we may write equation 2.1 as

$$p = \hat{A}f. \quad (2.2)$$

The direct inversion of the Abel transform⁴³ involves the derivative of the projection p and is therefore rather sensitive to experimental noise in the recorded images.⁴⁴ Several techniques exist that mitigate this problem,⁴⁵ including the projection slice theorem.^{46,47} In the presence of circular symmetry, the projection slice theorem reduces to a basic theorem relating the Abel, Fourier and Hankel transforms⁴⁸

$$\hat{H}\hat{F}\hat{A} = \hat{I} \quad (2.3)$$

where \hat{H} , \hat{F} , and \hat{A} are respectively the zero-order Hankel, Fourier, and Abel transform operators, and \hat{I} is the identity operator. Written as an integral equation in g we have

$$\int_0^\infty dk J_0(\alpha k) k \frac{1}{2\pi} \int_{-\infty}^\infty dx e^{-ikx} 2 \int_{|x|}^\infty dr \frac{r}{\sqrt{r^2 - x^2}} g(r) = g(\alpha)$$

where J_0 is the zero-order Bessel function of the first kind.⁴⁹ The zero-order Hankel, Fourier, and Abel transforms are readily identified.^{50,51,52}

The Hankel transform is computationally challenging,⁵³ but if we realise that the Hankel transform is reciprocal,⁵⁴ that is, $\hat{H}\hat{H} = \hat{I}$, we can deduce from equation 2.3 that

$$\hat{F}\hat{A}\hat{F}\hat{A} = \hat{I}$$

and, therewith we may write equation 2.2 as

$$f = \hat{F}\hat{A}\hat{F}p \quad (2.4)$$

providing a novel theorem for the inversion of the Abel transform, readily calculable using the following numerical methods. Note that the Abel transform assumes circular symmetry, deviations thereof affect the inversion.⁵⁵

The Fourier transform can be calculated using the following method. Let the sequence $\{p_n\}_{n \in \mathbb{Z}}$ be a discrete representation of a projection p . By definition the sequence $\{p_n\}$ is even in n , consequently the discrete

⁴³ Cooper 1966, p. 96.

⁴⁴ Griem 1997, p. 241; Hutchinson 2002, p. 143; Dribinski et al. 2002.

⁴⁵ Smith et al. 1988; Dribinski et al. 2002; Pretzler 1991.

⁴⁶ Bracewell 1956.

⁴⁷ The projection slice theorem, a fundamental relation in computed tomography, relates a one-dimensional slice of a two-dimensional Fourier transform to a one-dimensional Fourier transform of a one-dimensional projection.

⁴⁸ Bracewell 1956, p. 209.

⁴⁹ Arfken et al. 1995, p. 632.

⁵⁰ Arfken et al. 1995, pp. 846, 852; Bracewell 1956, p. 206.

⁵¹ The connection to the projection slice theorem is revealed by realising that the Hankel transform is identical to the two-dimensional Fourier transform of a radially symmetric function.

⁵² The applied Fourier transform uses the quantum mechanical sign convention, where a wave propagating in the k direction for $\omega > 0$ is represented by $e^{ik \cdot x - i\omega t}$.

⁵³ Candel 1981.

⁵⁴ Arfken et al. 1995, p. 648; Bracewell 1956, p. 207.

⁵⁵ Smith et al. 1988; Pretzler et al. 1992.

Fourier transform $\{f_k\}_{k \in \mathbb{Z}}$ of $\{p_n\}$ is even in k . If we assume that the subsequence $\{p_n\}_{n \geq 0}$ has length $N \in \mathbb{N}$, the discrete Fourier transform can be calculated using the type-I discrete cosine transform⁵⁶ given by

$$f_k = \frac{1}{2N-2} \left[p_0 + (-1)^k p_{N-1} + 2 \sum_{n=1}^{N-2} p_n \cos \left(\frac{\pi}{N-1} kn \right) \right].$$

⁵⁶ A discrete cosine transform has the advantage that it is guaranteed to be real valued.

The Abel transform can be calculated using the following method. Let the sequence $\{f_k\}_{k \in \mathbb{Z}}$ be an even sequence in k and assume that the subsequence $\{f_k\}_{k \geq 0}$ has length $N \in \mathbb{N}$. The discrete Abel transform $\{p_n\}_{n \in \mathbb{Z}}$ of $\{f_k\}$ can be calculated using the direct summation

$$p_n = \sum_{m=-N+1}^{N-1} \tilde{f}(\sqrt{n^2 + m^2})$$

where \tilde{f} is an interpolation of the sequence $\{f_k\}$. For our tomographic reconstruction a third order polynomial interpolation will be used.

2.5 Tomographic reconstruction and flow experiments

In the previous sections we introduced a self-organising toroidal plasma emerging solely by virtue of a single laser-induced breakdown plasma. We attributed the generation of this toroidal structure to fluid flow along the symmetry axis of the plasma. This fluid flow can be interpreted as flow replenishing a low density cavity, created in the wake of the shock generated by the breakdown plasma.

The existence of this cavity will be confirmed in section 3.2 where we present high-speed Schlieren images visualising the shock, and show that, because of the presence of this low density cavity, the creation of a laser-induced breakdown plasma will be suppressed in experiments with successive laser pulses.

Useful for the visualisation of the aforementioned fluid flow is a three-dimensional tomographic reconstruction of the toroidal plasma. In this section we present the poloidal radiant intensity profile⁵⁷ of our toroidal plasma, obtained through such a reconstruction, and infer the fluid flow from the motion of the plasma emission in the poloidal plane.

The characteristic time scale of the dynamics involved is explained by an intuitive model based on elementary thermodynamic principles. In conclusion, we will present flow experiments with a deliberately broken symmetry, confirming our hypotheses on the generation of the toroidal structure.

⁵⁷ See figure 2.11 for a schematic of the poloidal plane of a toroidal object as used in this work.

Tomographic reconstruction

A three-dimensional tomographic reconstruction of the toroidal plasma is feasible because of two helpful characteristics. We noted before that the toroidal plasmas are axially symmetric and optically thin plasmas. Moreover, we explained in section 2.4 that these characteristics provide the necessary conditions to employ Abel inversion⁵⁸ and to obtain a poloidal radiant intensity profile of the toroidal plasma.

⁵⁸ Cooper 1966, p. 96.

Figure 2.12 presents the evolution of the poloidal radiant intensity profile, showing the development and subsequent dissolvment of the toroidal plasma. These images have been obtained by Abel inversion⁵⁹ of the individual columns of the recorded side view images presented in figure 2.5. To assess whether the reconstruction is trustworthy, we compare, in the same figure, the poloidal radiant intensity profile with the corresponding front view images. We see that in the toroidal phase a dark region is noticeable in the centre of the front view images, which is confirmed by the dark region around the symmetry axis in the tomographically reconstructed images.

⁵⁹ The Abel inversion has been calculated using equation 2.4 and the numerical methods outlined in section 2.4.

The symmetry axis itself is highly sensitive to noise arising from a nearly singular condition in the reconstruction. This can be understood intuitively from the fact that the contribution from annuli near the symmetry axis is small compared to the contribution from annuli at larger distances.⁶⁰ This manifests itself in an accumulation of noise near the symmetry axis in the reconstructed images. To suppress artefacts arising from this noise, the one pixel wide symmetry axis has been

⁶⁰ Hanson 1993, p. 694; Griem 1997, p. 241.

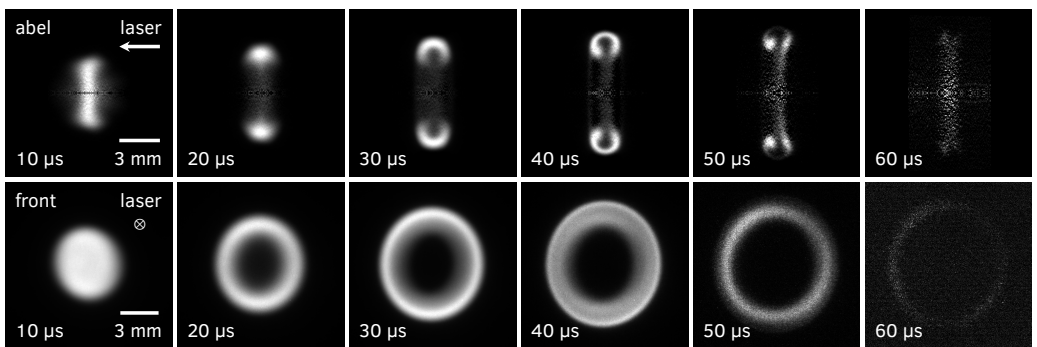


Figure 2.12: Evolution of the poloidal radiant intensity profile of a laser-generated toroidal plasma (top row) obtained through a three-dimensional tomographic reconstruction using the images presented in figure 2.5, together with the corresponding front view images (bottom row) to assess the reliability of the tomographic reconstruction. The front view images are identical to those shown in figure 2.6 and show slightly oval plasma structures due to a necessary skewed viewing direction. The images have been captured at increasing times (left to right) after the breakdown laser pulse. Note that the images have been individually normalised to their maximum intensity to respect the large dynamic range in intensity of the entire evolution. The images are based on the same recordings as those used for figures 2.4–2.6.

blackened in the reconstructed images. This is most visible at 10–15 μs .

Because the Abel inversion outlined in section 2.4 must be applied to an even sequence, the recorded side view images were symmetrised by discarding the top half of each image, to then apply the Abel inversion to the individual columns of the remaining bottom half. This geometrically motivated symmetrisation can be improved⁶¹ by a precise calculation of the position of the symmetry axis.

⁶¹ Pretzler et al. 1992.

Fluid flow visualisation

For the visualisation of the fluid flow responsible for the development of the toroidal plasma, we present in figure 2.13 contrast enhanced false colour images that better visualise the core of the toroidal plasma. To

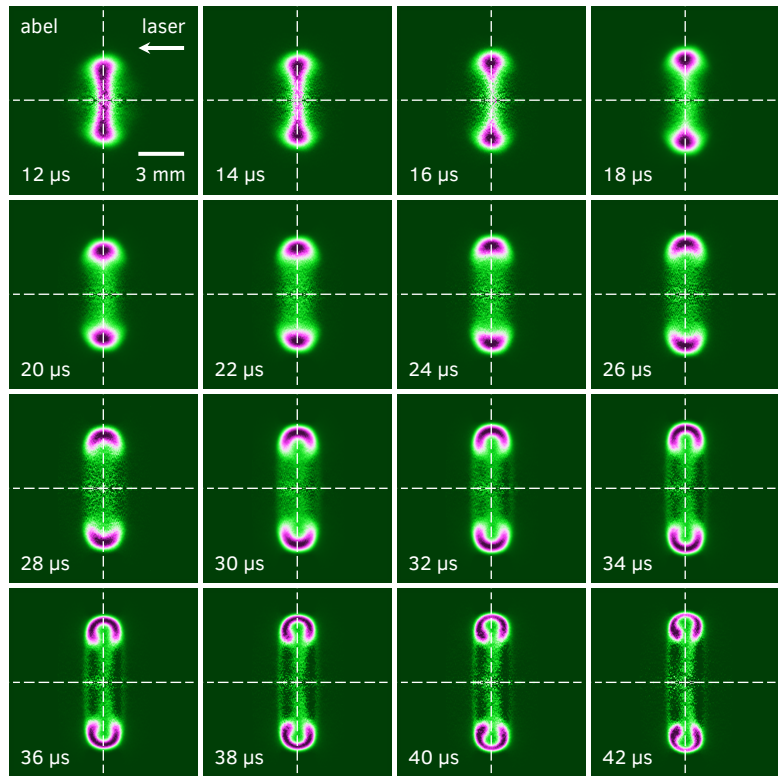


Figure 2.13: Fluid flow responsible for the development of a toroidal plasma. The contrast enhanced false colour images have been obtained through a three-dimensional tomographic reconstruction of the toroidal plasma and clearly visualises its core (purple). The fluid flow is inferred from the motion of the plasma emission. The longitudinal compression initially forming the plasma pillbox completely pinches off its centre at 18 μs thereby generating a toroidal plasma structure (see text for details). The images have been captured at increasing times after the breakdown laser pulse. Note that the images have been individually normalised to their maximum intensity to respect the large dynamic range in intensity of the entire evolution. The images are based on the same recordings as those used for figures 2.4–2.6.

assess whether the false colour images introduce artefacts or distort the images, we compare in figure 2.14, selected false colour images with their original and reconstructed black and white images. The images are consistent and do not show unexpected behaviour. Note however that the contrast enhanced images show slightly larger plasma structures than the black and white images. This comparison also nicely illustrates the necessity to perform a tomographic reconstruction, in order to observe features that are unobservable in the original images.

Figure 2.13 shows that the longitudinal compression forming the plasma pillbox mentioned in section 2.3 continues along the symmetry axis of the plasma structure (the symmetry axis is represented by the horizontal dashed line in the images). Eventually, at $18 \mu\text{s}$, the squeezing fluid flow, which at the same time repletes the aforementioned low density cavity, completely pinches off the centre of the plasma pillbox, thereby generating a toroidal plasma. Moments later, around $20\text{--}22 \mu\text{s}$, we observe an almost perfect plasma torus.

Due to our highly symmetrical breakdown plasma, the squeezing fluid flow that approaches the plasma from both sides is of approximate equal strength. These fluid flows will collide in the centre of the toroidal

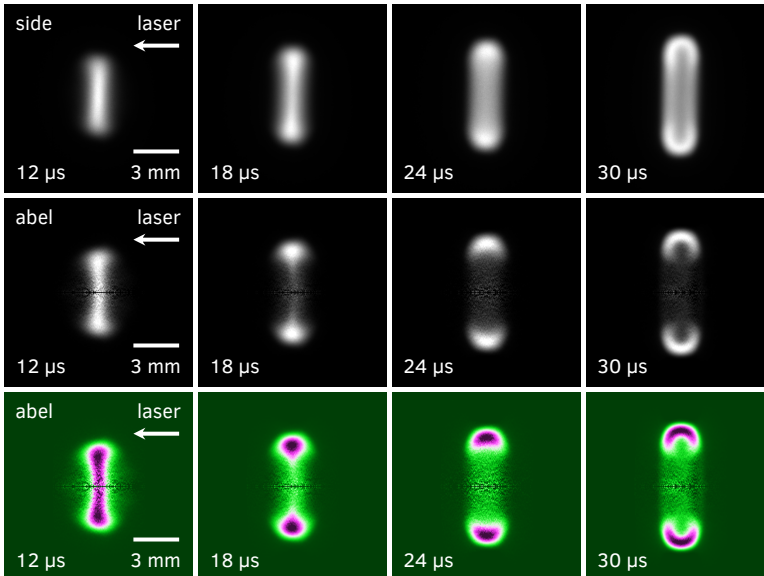


Figure 2.14: Comparison of selected contrast enhanced false colour images of the tomographically reconstructed, poloidal radiant intensity profile (bottom row) with the corresponding black and white (centre row) and original side view images (top row) to assess whether the false colour images introduce artefacts or distort the images. The false colour images (bottom row) are identical to those shown in figure 2.13. This comparison also illustrates the necessity to perform a three-dimensional tomographic reconstruction, in order to observe subtle features that are unobservable in the original side view images.

plasma, and spread out into the symmetry plane orthogonal to the symmetry axis, thereby pushing the plasma outward. This flow becomes visible from 24 μs onward, and deforms and erodes the toroidal plasma even further. This manifests itself as a horseshoe shaped plasma in the poloidal radiant intensity profile.

An estimate of the speed of the aforementioned fluid flow is easily obtained from the presented images. When we consider the fluid flow in the plane orthogonal to the symmetry axis, in the images between 24 μs and 42 μs , a fluid flow speed of 95 ± 3 m/s is obtained.

To interpret this speed it is helpful to compare it with the speed of sound in a gas, or more aptly, with the mean thermal speed of its constituents given by^{62,63}

$$v = \sqrt{\frac{8}{\pi} \frac{kT}{m}} \quad (2.5)$$

where k is the Boltzmann constant, T the gas temperature, and m the mass of an atom or molecule of the gas. Substitution of tabulated values⁶⁴ for helium at a temperature of 300 K results in a mean thermal speed of 1260 m/s.

The observed fluid flow speed is therefore approximately one tenth of the mean thermal speed. Since, by then, the toroidal plasma is fairly developed, the density in its centre has been partially restored as a result of the repleting fluid flow.⁶⁵ So the observed fluid flow does not expand into vacuum, but into a region with a partially restored density. The reduced fluid flow speed therefore seems reasonable. At earlier times, the fluid flow is not visible, but its speed will be higher because the density in the centre of the toroidal plasma is still reduced.

Characteristic time scale

So far we have presented a tomographically reconstructed poloidal radiant intensity profile that ably visualises the fluid flow responsible for the development of the toroidal plasma, and found that the flow speeds involved are akin to the mean thermal speed of the helium atoms. The observed characteristic time scale for the development of the toroidal plasma can be explained by following on from the foregoing through a simple model based on elementary thermodynamic principles.

Although this model will provide a characteristic time scale at which structure is expected to develop, it will not explain the mechanisms responsible for the development of the toroidal plasma. The asymmetric fluid flow necessary for this structure will be addressed in section 3.3.

⁶² Jeans 1940, p. 42.

⁶³ Note that these speeds are of the same order of magnitude, see Jeans 1940, p. 57.

⁶⁴ Haynes 2014.

⁶⁵ The number density by that time is approximately $0.7 n_0$. See figure 2.17 for details.

To model the evolution of a low density cavity, created in the wake of a shock generated by a laser-induced breakdown plasma, we assume that the volume of the breakdown plasma is infinitesimally small and that the laser pulse energy as a whole is converted to kinetic energy of the fluid surrounding the breakdown plasma.⁶⁶ Moreover, following on from our assumption that this model will not explain structure formation, we assume that the work done on the fluid is spherically symmetric in nature.

Inevitably a low density cavity will form, which continues to expand until all kinetic energy of the fluid is converted to potential energy of the cavity. At this stage the fluid is motionless. If we then assume that the successive repletion of the cavity is solely dictated by the thermal motion of the constituents of the fluid⁶⁷ we can infer a characteristic time scale by dividing the extremum of the radius of the cavity by the mean thermal speed of the constituents of the fluid. The evolution portrayed is illustrated in figure 2.15 and can be expressed mathematically as follows.

Let E be the laser pulse energy and assume that it as a whole is converted to work done on a fluid with ambient pressure p . Moreover, assume that the volume of the breakdown plasma is infinitesimally small and that the work $p dV$ done on the fluid is spherically symmetric in nature. Then we may write

$$E = \int p dV = \frac{4}{3} \pi R^3 p$$

where R is the extremum of the radius of the low density cavity.

Let τ be the characteristic time scale, defined as the time between breakdown and the collapse of the cavity, and further assume that the expansion and repletion are of equal duration. Then we have

$$\tau = 2 \frac{R}{v}$$

where v is the mean thermal speed defined by equation 2.5. Using the

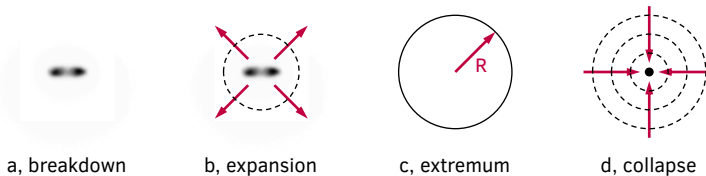


Figure 2.15: Schematic of the evolution of a low density cavity generated by a laser-induced breakdown plasma. The evolution of the cavity can be differentiated into four phases: breakdown, expansion, extremal radius, and collapse (see text for details). The repleting fluid flow is responsible for the generation of the toroidal plasma and dictates a characteristic time scale in the development of its structure.

⁶⁶ For laser pulse energies well above breakdown threshold, over 85% of the energy will be absorbed by the breakdown plasma, see Harilal et al. 2015; Y. Chen et al. 2000.

⁶⁷ This obviously is a coarse but nevertheless insightful approximation. A better one based on fluid dynamics has already been found by Besant 1859, p. 170 and Rayleigh 1917. See also Sinibaldi et al. 2019.

⁶⁸ Landau et al. 1987, P. 318.

⁶⁹ Note that T is the temperature of the ambient fluid.

⁷⁰ Haynes 2014.

equation of state $p/\rho = kT/m$ for an ideal gas^{68,69} the characteristic time scale τ may be written as

$$\tau = \frac{1}{2} \sqrt[3]{3} \left(\frac{\pi}{2}\right)^{\frac{1}{6}} E^{\frac{1}{3}} \rho^{\frac{1}{2}} p^{-\frac{5}{6}}$$

where ρ is the mass density of the fluid. Substitution of tabulated values⁷⁰ for helium at a temperature of 300 K results in a characteristic time scale of 13.4 μs for a laser pulse energy of 250 mJ. This is in agreement with the observations presented in figure 2.13 where at 16 μs the replenishing fluid flow approaches the symmetry plane orthogonal to the symmetry axis.

The calculated time scale is lower than observed experimentally because, as explained earlier, the observed fluid flow speed is lower than the mean thermal speed. The difference we find here is smaller than in the previous subsection because this value has been obtained at an earlier moment in the evolution, when the density in the cavity was restored to a lesser extent.

Density of helium atoms in the centre of the toroidal plasma

The characteristic time scale just obtained can be confirmed by a measurement of the evolution of the number density in the centre of the toroidal plasma. Using a second laser-induced breakdown plasma as a probe, created using an additional high power Nd:YAG laser, the spectral radiant intensity of this breakdown plasma can be used as a measure of the local number density, when correlated with calibration measurements separately obtained in quiescent helium gas at known number densities. Figure 2.16 presents selected images that illustrate this probing with a second laser-induced breakdown plasma.

The evolution of the number density in the centre of the toroidal plasma, obtained in the above manner, is presented in figure 2.17, and

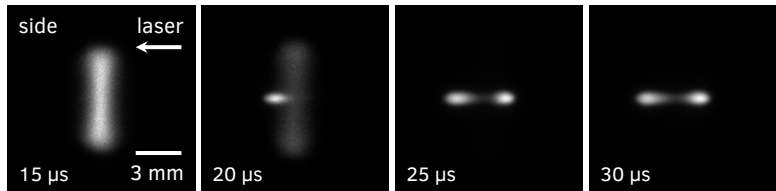


Figure 2.16: Second laser-induced breakdown plasma used to measure the number density in the centre of the toroidal plasma. (15 μs) Toroidal plasma with indiscernible (suppressed) second breakdown plasma. (20 μs) Visible second breakdown plasma with faintly visible toroidal plasma. (25 and 30 μs) Clearly visible second breakdown plasma, with toroidal plasma too faint to discern. Note that the images have been individually normalised to their maximum intensity. The images are based on the same recordings as those used for figure 2.17.

shows that the number density starts to replete within 20 μs after the breakdown laser pulse. This is in agreement with the model presented in the previous section. Unfortunately, the measurements obtained at earlier times are not reliable due to the presence of the bright plasma pillbox, which interferes with the measurement of the intensity of the probing breakdown plasma.

A notable observation can be made regarding the time-dependent exponential decay rate of the spectral radiant intensity of the toroidal plasma. As already noted in section 2.3, two exponential sections can be observed, where the second section is decreasing even faster than the first. This has already been observed in figure 2.9, but is likewise visible in figure 2.17.

The time-dependent decay rate presented in figure 2.17 shows that, at approximately 30 μs the decay rate starts to increase rapidly. This is roughly 10 μs later than when the density in the centre of the toroidal plasma starts to increase. Note that in this figure, the region where the measurement noise becomes prominent, indicated by a decrease in the

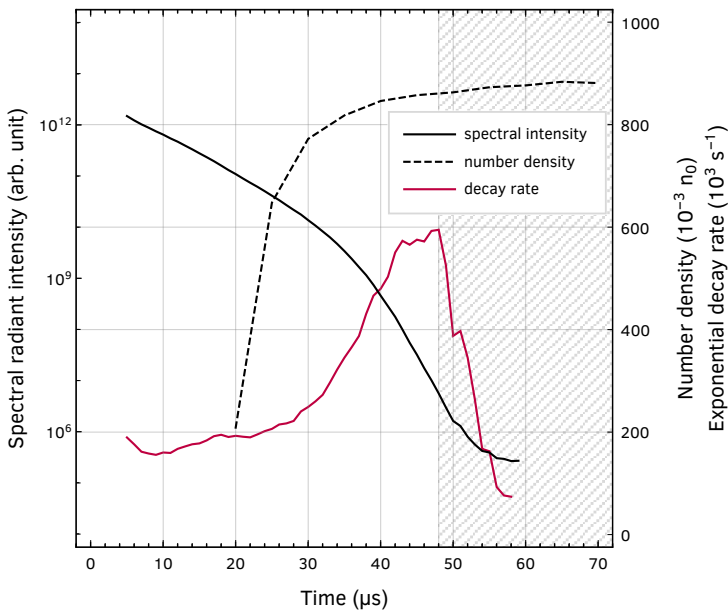


Figure 2.17: Number density in the centre of the toroidal plasma (dashed line) measured using a second laser-induced breakdown plasma as a probe. The number density starts to increase at approximately 20 μs as a result of the repleting fluid flow responsible for the generation of the toroidal plasma. Note the (delayed) correlation between the increase in the time-dependent exponential decay rate (purple line) of the spectral radiant intensity curve (black line) and the increase in number density. The region where the measurement noise becomes prominent is indicated by a grey shading. This graph is based on recordings captured using similar experimental settings as those presented in figures 2.4–2.6. Loschmidt constant $n_0 = 2.65 \cdot 10^{25} \text{ m}^{-3}$ is the number density of an ideal gas at standard temperature and pressure.

time-dependent decay rate, is highlighted by a grey shading.

The delayed increase in the decay rate can be understood by realising that the density measurements are performed at the symmetry axis, in the centre of the toroidal plasma, while the time-dependent exponential decay rate is derived from the spectral radiant intensity of the toroidal plasma, originating from a considerable distance from the symmetry axis. This is likewise confirmed by observing that the poloidal radiant intensity profile of the toroidal plasma, presented in figure 2.13, clearly starts its deformation into a horseshoe shaped plasma precisely when the decay rate starts to increase.

Flow experiment with a deliberately broken symmetry

Until now we have argued that, as a result of the highly symmetrical nature of our laser-induced breakdown plasma, the replenishing fluid flow responsible for the development of the toroidal plasma, approaches the plasma from both sides equally. However, even though the breakdown plasma presented in figure 2.4 appears very symmetric, it in fact is not. This can be appreciated from the slight asymmetry visible in the poloidal radiant intensity profile presented in figure 2.13, where the asymmetry is most clearly visible from $38 \mu\text{s}$ onward.

When a toroidal plasma is generated with a different laser pulse energy, this asymmetry is likewise observed, albeit occasionally reflected in the symmetry plane. This alternating asymmetry is clearly visible in figure 2.18. A slight imbalance in the generation of a laser-induced breakdown plasma appears to result in a slightly asymmetric fluid flow replenishing the low density cavity.

To confirm our interpretation regarding the symmetric repletion of the low density cavity, by the fluid flow responsible for the development of the toroidal structure, we performed flow experiments where the

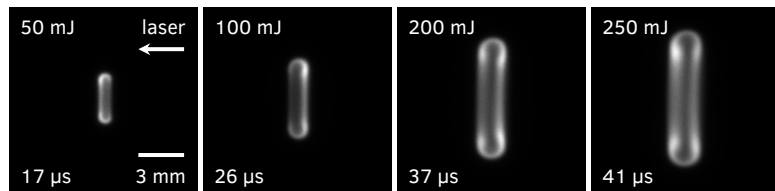


Figure 2.18: Slight asymmetry visible in the symmetry plane orthogonal to the symmetry axis of a toroidal plasma due to an imbalance of the fluid flow responsible for its development. The toroidal plasmas have been generated with a pulse energy of 50, 100, 200, and 250 mJ and show an alternating asymmetry with different laser pulse energies. The images are based on recordings captured using similar experimental settings as those presented in figures 2.4–2.6 and are a reproduction of figure 2.10.

symmetry in the plane orthogonal to the symmetry axis is deliberately broken. This symmetry breaking has been realised by placement of a metal sheet close to the laser focus, through which the laser pulse is allowed to pass, through a small 2.8 ± 0.1 mm hole. The distance of the metal sheet to the laser focus was 6.0 ± 0.1 mm, sufficient to avert contact with the focussed laser pulse.

The poloidal radiant intensity profile, again obtained through a three-dimensional tomographic reconstruction of the toroidal plasma, is presented in figure 2.19. In figure 2.20 selected contrast enhanced false colour images are presented, together with the original and reconstructed black and white images, to assess whether the false colour images introduce artefacts in the reconstructed images. This comparison

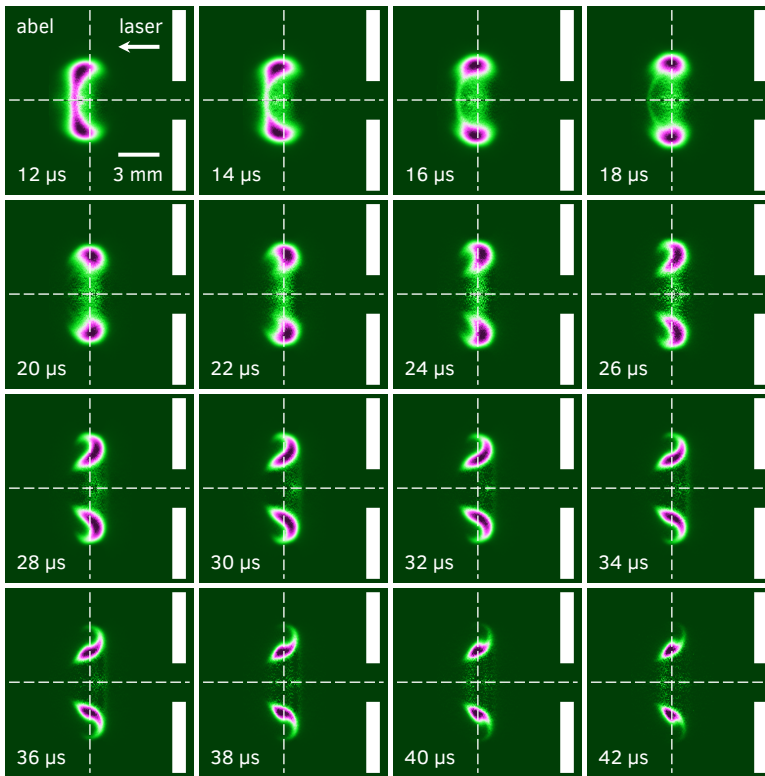


Figure 2.19: Development of a toroidal plasma with a deliberately broken symmetry by means of a metal sheet (two white rectangles) close to the laser focus. The metal sheet has a 2.8 mm hole through which the laser pulse passes and is shown to scale. The fluid flow is inferred from the motion of the plasma emission. Note the revolving motion of the plasma core (purple) testimonial to the presence of vorticity. The contrast enhanced false colour images have been obtained through a three-dimensional tomographic reconstruction of the toroidal plasma. The images have been captured at increasing times after the breakdown laser pulse. Note that the images have been individually normalised to their maximum intensity to respect the large dynamic range in intensity of the entire evolution. The images are based on recordings captured using similar experimental settings as those presented in figures 2.4–2.6.

once more illustrates the necessity to perform a three-dimensional tomographic reconstruction in order to observe subtle features that are unobservable in the original images.

Note that in the presented images we have depicted the metal sheet to scale as two white rectangles. The symmetry axis is represented by the horizontal dashed line, while the vertical dashed line is identical to the aforementioned symmetry plane orthogonal to the symmetry axis. Both dashed lines cross at the laser focus in the centre.

The detailed evolution of the poloidal radiant intensity profile can best be understood by anticipating the consequences of the placement of the symmetry breaking metal sheet. When we consider the expanding low density cavity from our model presented earlier in this section, we can expect that the expansion along the symmetry axis will be obstructed by the symmetry breaking metal sheet. This obstruction prevents the low density cavity to extend beyond the metal sheet. Consequently, we expect that the repleting fluid flow from beyond the metal sheet, flowing through the small 2.8 mm hole, will commence in advance with respect to the repleting flow due to the collapse of the cavity. Due to this asymmetry, the two repleting flows are expected to

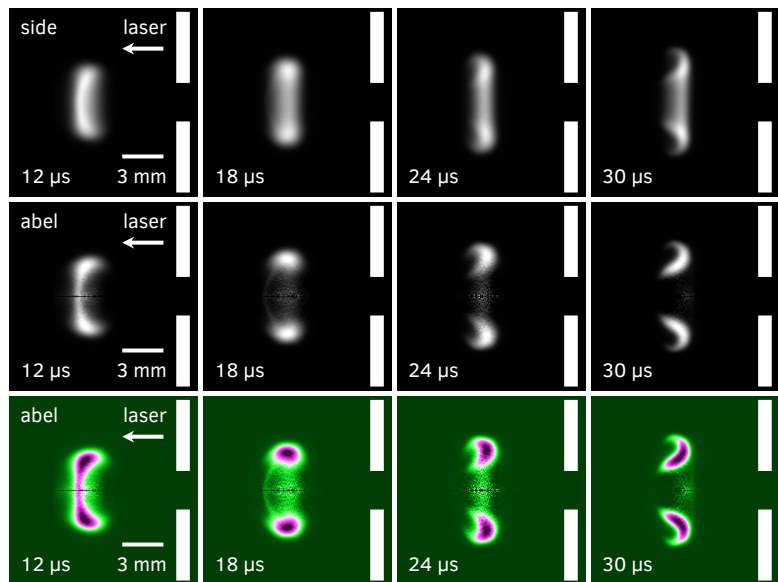


Figure 2.20: Comparison of selected contrast enhanced false colour images of the tomographically reconstructed, poloidal radiant intensity profile (bottom row) and the corresponding black and white (centre row) and original side view images (top row) to assure the false colour images do not introduce artefacts or deform the original images. The false colour images (bottom row) are identical to those shown in figure 2.19. This comparison again illustrates the necessity to perform a three-dimensional tomographic reconstruction in order to observe subtle features that are unobservable in the original images.

collide, not in the centre of the toroidal plasma, as in figure 2.13, but further away from the metal sheet. Accordingly, the flow is expected to spread out, not in the symmetry plane of the original experiment, which is represented by the vertical dashed line in figure 2.19, but at a distance to that plane.

Our foregoing anticipation is confirmed by the evolution presented in figure 2.19. The plasma pillbox is seen to be pushed aside due to the fluid emanating from the hole in the metal sheet. The same fluid flow subsequently pushes a hole into the plasma pillbox, which at 16 μs , a few microseconds earlier than in our symmetric experiment presented in figure 2.13, completely pierces through the centre of the plasma pillbox, thereby again forming a toroidal structure.

The colliding fluid flows are difficult to distinguish in the beginning, but start to appear at 22 μs as a distinct notch in the poloidal profile. This notch corresponds to the earlier observed horseshoe shaped plasma in the original experiment. We see that the fluid flow is not spreading out into a plane, but instead into a cone. This can be expected because the fluid flow replenishing the cavity has a larger extent than the fluid flow emanating through the hole in the metal plate.

Lastly, as a result of the colliding fluid flows, the toroidal plasma is observed to rotate. This is a testimony of the presence of vorticity. Numerical studies on the fluid dynamical effects of laser energy deposition have shown⁷¹ that the generation of vorticity found in these systems stems from the asymmetry of the breakdown plasma, whereas in our case the origin lies in the asymmetric experimental setting.

⁷¹ Ghosh et al. 2008; Morsy et al. 2002.

Plasma flow through a toroidal plasma

In one of our preliminary experiments, we utilised the ability of our experimental set-up to create a second laser-induced breakdown plasma in close proximity of a previously generated toroidal plasma. This has been realised by displacing the focus of the laser pulses of a second Nd:YAG laser, using a diverging plano-concave lens as explained in the experimental details in section 2.2.

Figure 2.21 presents selected images of the evolution of a second laser-induced breakdown plasma, created in close proximity of a toroidal plasma which is in development at that time. In each image, a side view (top half) and a slightly skewed front view (bottom half) are presented simultaneously. The principal laser-induced breakdown plasma, which develops into the toroidal plasma, is shown in green false colour in the first two images, to be able to distinguish it from the second

breakdown plasma. Note that in the second image, at $8.1 \mu\text{s}$, the toroidal plasma is very faint, to make it visible it has been combined with a separately obtained green false colour image of the toroidal plasma.

First, a laser-induced breakdown plasma is created at $0 \mu\text{s}$. Then, $8 \mu\text{s}$ later, while the toroidal plasma is still in development, a second laser-induced breakdown plasma is created by the second Nd:YAG laser. This second breakdown plasma is created with reduced power, to still be able to observe the toroidal plasma that is steadily decreasing in intensity.

From the evolution presented in figure 2.21, it is clear that the second breakdown plasma is drawn through the centre of the toroidal plasma generated by the principal breakdown plasma. This attests to fluid flow through the centre of the toroidal plasma, and implies that the low density cavity responsible for the generation of the toroidal structure, repletes in an asymmetric way. This can be understood when

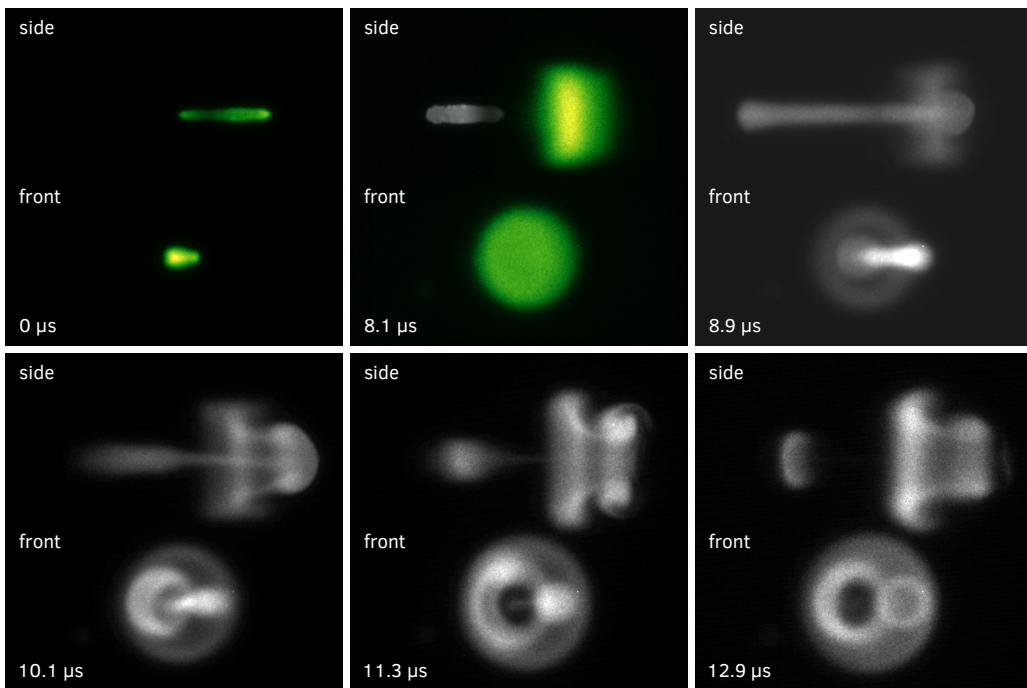


Figure 2.21: Selected images of the evolution of a second laser-induced breakdown plasma, created at $8 \mu\text{s}$, and in close proximity of a toroidal plasma which is in development at that time. In each image, a side view (top half) and a slightly skewed front view (bottom half) are presented simultaneously. The principal laser-induced breakdown plasma, which develops into the toroidal plasma, is shown in green false colour in the first two images, to be able to distinguish it from the second breakdown plasma. Note that in the second image, at $8.1 \mu\text{s}$, the toroidal plasma is very faint, to make it visible it has been combined with a separately obtained green false colour image of the toroidal plasma. The images have been individually normalised to their maximum intensity, and are based on recordings captured using similar experimental settings as those presented in figures 2.4-2.6.

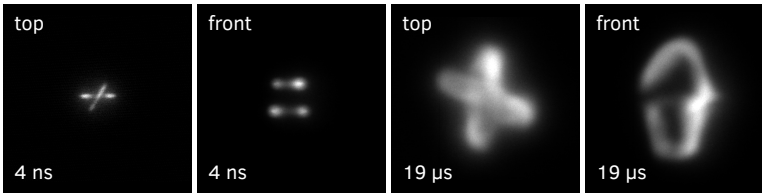


Figure 2.22: Crossed plasma arches (right pair, top and front view) developing as a result of two simultaneously created laser-induced breakdown plasmas (left pair, top and front view). The closely spaced and crossed breakdown plasmas have been created at a distance of 1.5 mm from each other therewith breaking the conventional symmetrical setting that generates a toroidal plasma.

we realise that the principal breakdown plasma presented at $0 \mu\text{s}$ is very asymmetric, and is further supported by our interpretation of the asymmetric repletion of the low density cavity presented in the previous subsection. The fluid flow along the symmetry axis is also found to have a considerable range, testified by the fact that in the last image, at $12.9 \mu\text{s}$, three toroidal plasmas can be observed.

Experiment with two closely spaced crossed breakdown plasmas

We end this section by presenting an experiment where the symmetrical experimental setting is broken by simultaneously creating two closely spaced crossed laser-induced breakdown plasmas. This experiment was originally conducted in an attempt to create two linked toroidal plasmas, but with the insights gained in this section we can understand why we observed the two plasma arches presented in figure 2.22, instead of the naively expected linked toroidal plasmas.

We have seen that during the evolution of a single laser-induced breakdown plasma, the fluid flow repleting the low density cavity, which at the same time reshapes the breakdown plasma, predominantly manifests itself along the symmetry axis through the centre of the low density cavity. Having two closely spaced crossed breakdown plasmas, this flow will manifest itself in the plane separating these two breakdown plasmas. As a result, instead of developing into two toroidal plasmas, the two breakdown plasmas are pushed outward by the repleting fluid flow, thereby forming two separate plasma arches.

2.6 Oxygen impurity effects in helium plasma afterglows

In the previous sections we observed that the spectral radiant intensity of a laser-induced breakdown plasma decreases purely exponentially over the better part of its evolution. This is remarkable given the huge

change in size and morphology over time and may be indicative of local plasma chemistry.

In this regard, the contamination of our plasma reactor by oxygen impurities, as a result of the desorption of air from the reactor walls, may be a probable cause. For electrons are assumed to be responsible for the plasma emission through collisional excitation of neutral atomic helium, and the attachment of electrons to oxygen molecules is a known mechanism for removing electrons.⁷² Incidentally, because of the attachment of electrons to oxygen molecules, the electron density decreases exponentially over time.

⁷² Chanin et al. 1962; Raizer 1991, p. 63.

Alternative mechanisms for the decay of electrons exist, in particular recombination and ambipolar diffusion.⁷³ However, by recombination, the electron density decreases according to the power-law t^{-1} , and for ambipolar diffusion, the electron density decreases exponentially only when the electrons diffuse to the walls of the reactor. The latter is not likely in our experiment considering the fact that the size of our plasma is a factor 20 smaller than the diameter of our reactor.

⁷³ Raizer 1991, pp. 52, 60, and 67.

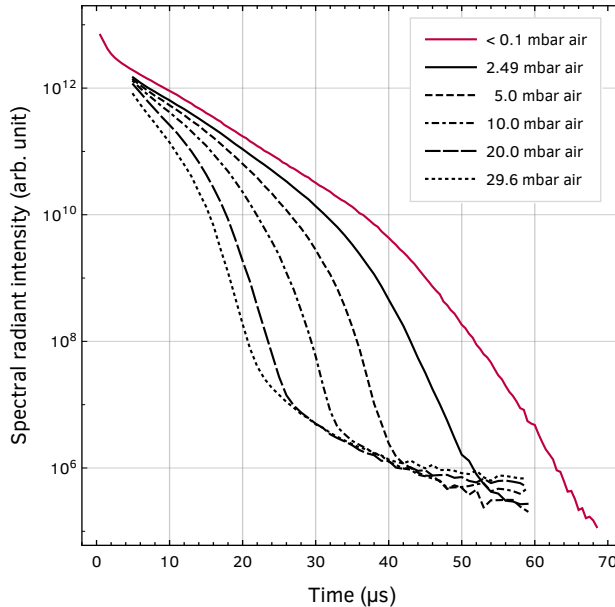


Figure 2.23: Spectral radiant intensity of a laser-induced breakdown plasma created in quiescent atmospheric pressure helium-air mixtures using a laser pulse energy of 250 mJ demonstrating the effect of contamination of our plasma reactor. The graph shows the spectral radiant intensity for different partial pressures while maintaining a total pressure of 1000 mbar. The separately obtained pure helium measurement (purple line) is identical to the 250 mJ measurement presented in figure 2.9. This graph is based on recordings captured using similar experimental settings as those presented in figures 2.4–2.6.

To examine the aforesaid hypothesis concerning the attachment of electrons to oxygen molecules, figure 2.23 presents the spectral radiant intensity of a laser-induced breakdown plasma created in quiescent atmospheric pressure helium-air mixtures, for different partial air pressures, while maintaining a total pressure of 1000 mbar. We noted before that two exponential sections can be observed, where the second section is decreasing even faster than the first. In section 2.5 we linked this increase in the time-dependent exponential decay rate to a restored density in the surrounding area of the toroidal plasma.

In figure 2.23 we also observe that, at a higher partial air pressure, the spectral radiant intensity is decreasing faster. Furthermore, we see that the instant that the exponential decay rate starts to increase, is also brought forward, implying that the fluid flow changes as well.

In figure 2.24, we present the time-dependent exponential decay rate that has been derived from the spectral radiant intensity. Clearly a plateau at 5–10 μs can be observed for all partial air pressures.

The average value of the time-dependent exponential decay rate for these plateaus is presented in figure 2.25 as a function of the partial air pressure. A linear relation can be observed between the decay rate

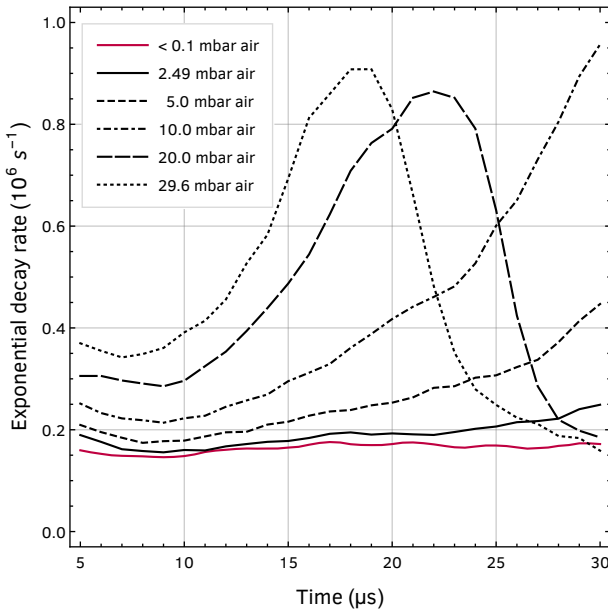
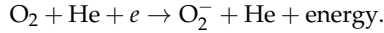


Figure 2.24: Time-dependent exponential decay rate derived from the spectral radiant intensity presented in figure 2.23. The time-dependent exponential decay rate has been calculated under the assumption of pure exponential decay between neighbouring time steps. Note the plateaus at 5–10 μs that can be observed for all partial air pressure measurements.

and the partial air pressure in the reactor. The constant contribution in this linear relation is unaccounted for and we propose that this may be caused by the slow cooling of the plasma.

For low energy electrons (<1 eV) the attachment of electrons to oxygen molecules is primarily a three-body reaction given by⁷⁴

⁷⁴Chanin et al. 1962; Raizer 1991, p. 63.



The rate of change of the electron density may then be written as

$$\frac{dn_e}{dt} = -\lambda n_e = -k n_{\text{He}} n_{\text{O}_2} n_e$$

where λ is the exponential decay rate, k the three-body attachment coefficient, and n_e , n_{He} , and n_{O_2} are, respectively, the electron, helium atom, and oxygen molecule number densities. Using this relation we can validate the linear dependence presented in figure 2.25.

Let us reasonably assume that around 5–10 μs the helium number density n_{He} in the surrounding area of the toroidal plasma is not higher

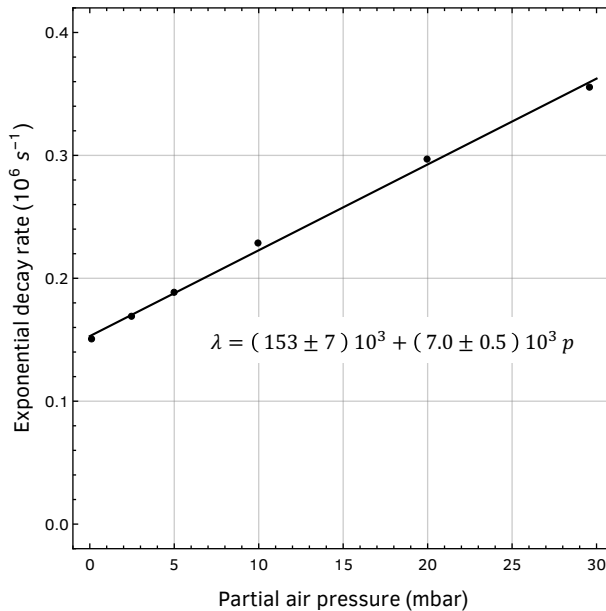


Figure 2.25: Averaged time-dependent exponential decay rate as a function of partial air pressure for the plateaus observed in figure 2.24. The time-dependent exponential decay rate of the plateaus has been fitted against a linear function (black line).

than $0.1 n_0$ with n_0 the equilibrium density.^{75,76} If we furthermore use $k = 2.5 \cdot 10^{-30} \text{ cm}^6 \text{ s}^{-1}$ as an average value for the three-body attachment coefficient⁷⁷ we find for the exponential decay rate a value of $0.11 \cdot 10^6 \text{ s}^{-1}$ at 30 mbar partial air pressure.⁷⁸

In figure 2.25 we see that at a partial air pressure of 30 mbar, the contribution to the time-dependent exponential decay rate originating from the presence of air in the plasma reactor is $0.21 \cdot 10^6 \text{ s}^{-1}$. This is of the same order of magnitude as the calculated value.

The above analysis shows that the purely exponential decay of the spectral radiant intensity is, in part, attributable to the contamination of our plasma reactor by oxygen impurities. For ultra pure helium in a baked out plasma reactor we, of course, still expect the plasma to decay. The constant contribution observed in the time-dependent exponential decay rate is unaccounted for in this analysis, and we propose that this may be caused by the slow cooling of the plasma.

Although the above analysis seems fairly conclusive, it is based on a simplified model of what is in fact a complex dynamical process and might need modification. It has been shown that meta-stable and Rydberg states are present in atmospheric pressure helium afterglow plasmas.⁷⁹ Therefore, the assumed linear relationship between the neutral atomic helium emission line intensity and the electron density might need modification. In this regard, a power-law relationship has been reported in the literature.⁸⁰ Coincidentally, in this case the decay will still continue to be exponential, although with a modified decay rate. Furthermore, it has been shown that a zero dimensional kinetic model of a pure helium plasma exhibits exponential decay of the electron density,⁸¹ which provides an explanation for the constant contribution observed in the time-dependent exponential decay rate.

2.7 Plasma kernel dynamics

So far, we have been mainly concerned with examining the evolution of toroidal plasmas generated by a single laser-induced breakdown plasma. We visualised and interpreted the responsible fluid flow, and throughout these discussions the highly symmetrical nature of the two-lobe breakdown plasma proved to be of some importance.

Experimental laser-induced breakdown studies,⁸² just as numerical studies on the fluid dynamical effects of laser energy deposition,⁸³ likewise report similar toroidal structures, but instead observed highly asymmetrical tear-drop shaped breakdown plasmas.

More recent studies addressing the onset and dynamics of plasma

⁷⁵ See figure 2.17 for details.

⁷⁶ Loschmidt constant $n_0 = 2.65 \cdot 10^{25} \text{ m}^{-3}$ is the number density of an ideal gas at standard temperature and pressure.

⁷⁷ Chanin et al. 1962.

⁷⁸ Note that air contains approximately 21% oxygen, see Haynes 2014.

⁷⁹ Schregel et al. 2016; Carbone et al. 2016; Nedanovska et al. 2015.

⁸⁰ Stevefelt et al. 1971, p. 10.

⁸¹ Nedanovska et al. 2015.

⁸² Nassif et al. 2000; Harilal et al. 2015; Bak, Wermer et al. 2015; Dumitrache et al. 2017; Bradley et al. 2004; Bak, Im et al. 2014.

⁸³ Ghosh et al. 2008; Morsy et al. 2002.

⁸⁴ Nishihara et al. 2018; Alberti, Munafò, Pantano et al. 2019a.

⁸⁵ See Nishihara et al. 2018 and references therein.

⁸⁶ Alberti, Munafò, Pantano et al. 2019b.

⁸⁷ Alberti, Munafò, Koll et al. 2020; Alberti, Munafò, Pantano et al. 2019b.

kernels, however, do report plasmas with a two-lobe structure similar to those observed in our experiments.⁸⁴ Different mechanisms have been identified, including self-focussing, lens aberration, and hydrodynamic instabilities,⁸⁵ but the onset and dynamics of plasma kernels is still not very well understood.⁸⁶

The lately reported kernels⁸⁷ even show a striking resemblance to the laser-induced breakdown plasmas observed in our experiments. To relate these observations to each other, this section presents high temporal resolution images of our breakdown plasma, compares them to the lately reported plasma kernels, and correlates photo detector measurements of the laser pulse intensity with intensity measurements obtained through integration of the recorded images.

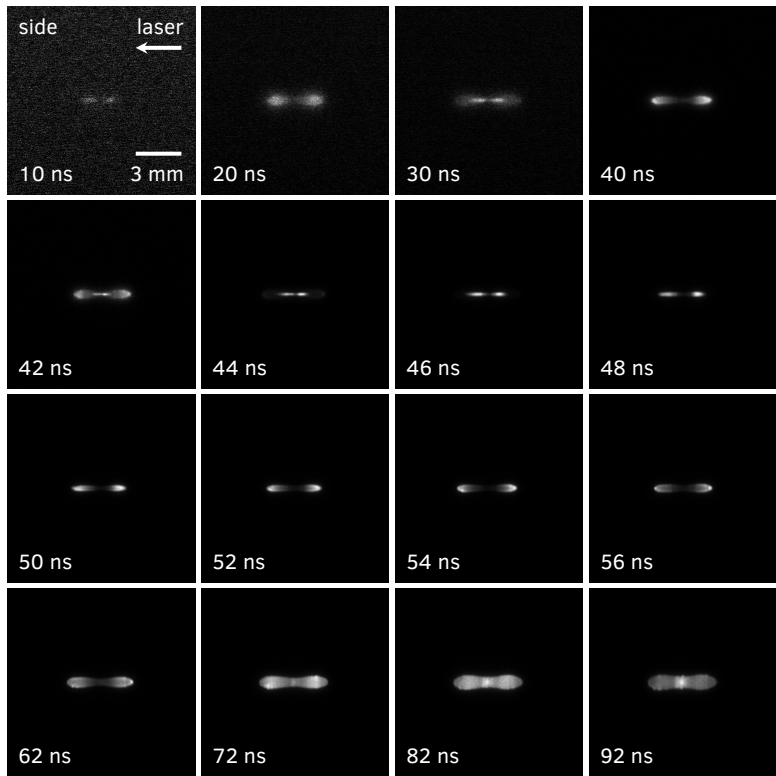


Figure 2.26: Early development of a laser-induced breakdown plasma showing the repeating dynamics of the two-lobe structure in the plasma kernel. The high temporal resolution side view images have been captured at increasing times after the laser trigger. Note that $t = 0$ has no physical meaning and is arbitrarily chosen. (10–20 ns) Small and faint expanding two-lobe plasma. (30–40 ns) Another smaller but brighter expanding two-lobe plasma. (42–92 ns) Another, even smaller and brighter, expanding two-lobe plasma which will develop into the principal breakdown plasma (see text for details). The images have been individually normalised to their maximum intensity. Laser pulse energy: 275 mJ, focal length focussing lens: 50 mm, helium gas pressure: 1000 mbar, bandpass filter: none, ICCD camera gate width: 2 ns, ICCD camera image averaging: none.

In figure 2.26 we present a selection of images recorded with an exposure time of 2 ns while using a laser pulse energy of 275 mJ. The images have been captured at increasing times after the laser trigger and without using a bandpass filter. Note that $t = 0$ bears no physical meaning and is arbitrarily chosen.

The integrated intensity of the recorded images is presented in figure 2.27, together with separately obtained intensity measurements using a photo detector. Synchronisation of the integrated intensity with the measurements obtained using the photo detector has been done by correlating their intensity curves and translating the photo detector measurements in the time domain until they overlap.

The intensity measurements show a 4 ns delay between the emission of the principal breakdown plasma and the laser pulse, before it relaxes exponentially over greater time scales. Remarkably, tens of nanoseconds before the main laser pulse is observed, a faint plasma is visible in the recorded images. We attribute this to the formation of the giant pulse in our Q-switched Nd:YAG laser. Initially the photon density starts at a

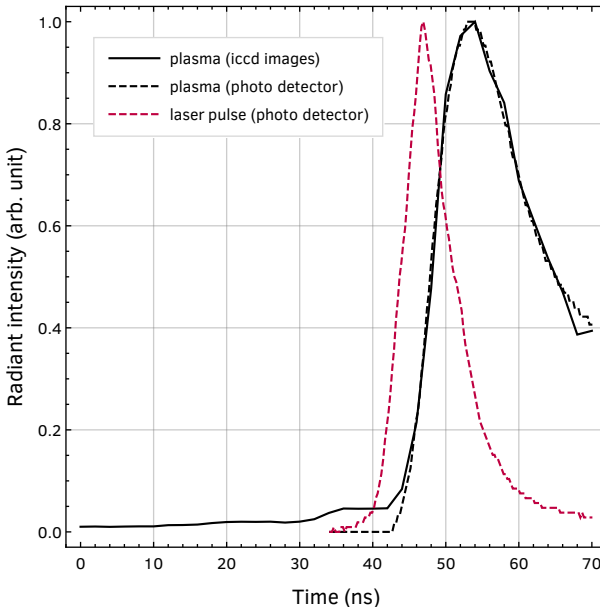


Figure 2.27: Radiant intensity of the plasma kernel (dashed black line) and laser pulse (dashed purple line) recorded through a photo detector, overlaid with the integrated intensity of the plasma kernel images presented in figure 2.26 (solid black line). Note the 4 ns delay between the laser pulse and the emission of the principal breakdown plasma. The intensity traces have been individually normalised to their maximum intensity and averaged over 100 recordings. The temporal axis represents time after the laser trigger. Note that $t = 0$ has no physical meaning and is arbitrarily chosen, but identical to the plasma kernel images presented in figure 2.26.

⁸⁸ Wagner et al. 1963.

low value, and then grows at an approximately exponential rate before forming the giant pulse.⁸⁸ During the exponential growth, the photon density is small compared to the giant pulse, but it can nevertheless be sufficient to induce breakdown and create a faint plasma. The photo detector does not observe this weak emission, most probably due to a minor misalignment or an incorrect bias setting of the detector.

In the images presented in figure 2.26, a small and faint two-lobe plasma is discernible some 30 ns before the advent of the main laser pulse. This two-lobe plasma slightly expands for 20 ns, after which a second, smaller but brighter, two-lobe plasma is observed, within the already present plasma. This plasma likewise expands for 12 ns, after which, once again, an even smaller but still brighter, two-lobe plasma is observed at 42 ns, marking the beginning of the main laser pulse. At the end of the laser pulse, the two-lobe plasma fills up and emission is observed from the entire elongated plasma. This is clearly visible in the recorded images from 72 ns onward.

⁸⁹ Raizer 1991, p. 155.

⁹⁰ Miziolek et al. 2006, p. 171.

⁹¹ Alberti, Munafò, Pantano et al. 2019a; Y. Chen et al. 2000; Harilal et al. 2015; Ghosh et al. 2008.

In general a laser-induced breakdown plasma is created as a result of avalanche ionisation, where multi-photon ionisation provides the initial seed electrons necessary to ignite the avalanche.⁸⁹ Subsequent inverse bremsstrahlung absorption heats the plasma⁹⁰ creating a high pressure and high temperature plasma kernel whose rapid expansion leads to the formation of a shock.⁹¹ The repeating dynamics observed in our plasma kernel possibly contributes to the formation of the two-lobe structure by successively creating small low density cavities, thereby increasing the breakdown threshold and inhibiting the creation of additional plasma in the central region.

⁹² Alberti, Munafò, Koll et al. 2020; Alberti, Munafò, Pantano et al. 2019b; Alberti, Munafò, Pantano et al. 2019a.

The plasma kernels presented in this work strikingly resemble the images reproduced in figure 2.28, which have recently been reported in studies on the onset and dynamics of plasma kernels.⁹² The non-equilibrium three-temperature plasma model presented therein is in good agreement with experimental observations and accounts for multi-

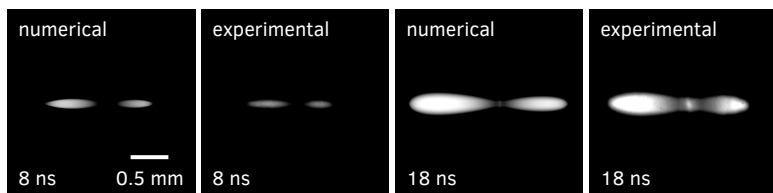


Figure 2.28: Laser-induced breakdown plasmas created in quiescent atmospheric pressure air. The two-lobe plasma kernels strikingly resemble the kernels presented in figure 2.26. These images are reproduced from a numerical and experimental study on plasma kernel dynamics (Alberti, Munafò, Koll et al. 2020) with permission of the Institute of Physics Publishing.

photon ionisation, inverse bremsstrahlung absorption, chemical kinetics, shock dynamics, and radiation propagation. Despite addressing laser-induced breakdown in air, which necessitates a chemical kinetics component accounting for the plasma chemistry of the constituents of air, their model is still in good agreement with our observations.

2.8 Conclusion

In this chapter, we have examined self-organising toroidal plasmas, generated solely by a single laser-induced breakdown plasma, created in quiescent atmospheric pressure helium gas at room temperature. We addressed many aspects of its development and found the generation to be robust over a wide range of laser pulse energies.

We tomographically reconstructed the poloidal radiant intensity profile of a toroidal plasma for its entire evolution, using a novel numerical method based on transform techniques for the Abel inversion. We used this reconstruction to visualise the fluid flow responsible for the development of the toroidal structure, and presented a first observation of the eroding and splitting of the toroidal plasma caused by the symmetrical nature of the two-lobe plasma kernel.

The origin of this flow is found to stem from the fluid flow replenishing the low density cavity, created in the wake of a shock generated by the laser-induced breakdown plasma. In support of the existence of this cavity, we measured the evolution of the density of helium atoms in the centre of the toroidal plasma, with the use of a second laser-induced breakdown plasma.

We established a characteristic time scale at which structure is expected to develop. For a laser-induced breakdown plasma, created in quiescent atmospheric pressure helium gas at room temperature using a laser pulse energy of 250 mJ, the characteristic time scale is found to be approximately 16 μs , in agreement with our calculated value of 13.4 μs .

We found that the symmetrical nature of the toroidal plasma stems from the symmetrical fluid flow replenishing the low density cavity, which is supported by flow experiments where the symmetrical experimental setting is deliberately broken by placement of a metal sheet close to the laser focus. By breaking the symmetry, vorticity has been introduced in the toroidal plasma.

We presented nanosecond temporal resolution recordings of the evolution of the plasma kernel, and observed a novel repeated creation of plasma that we attribute to the formation of the giant pulse in the Q-switched Nd:YAG laser. This repeating dynamics contributes to the

formation of the two-lobe structure of the plasma kernel.

The observed laser-generated transient toroidal helium plasmas are robust toroidal structures created under atmospheric pressure ambient conditions. These properties indicate that they provide an interesting setting for investigating the self-organising knotted magnetic structures in plasma introduced at the outset of this chapter.

To strengthen our understanding of the development of the toroidal plasmas, our next steps will include measurements that further support the existence of the aforementioned low density cavity, and measurements that characterise the plasma parameters of the toroidal plasmas, like the electron number density and the electron collision rate. These experiments will be presented in chapters 3 and 4 of this dissertation.

3

Shocks and successive laser pulse experiments

In our studies on laser-generated, atmospheric pressure, transient toroidal helium plasmas, the low density cavity generated by the laser-induced breakdown plasma proved pivotal. Here, we present a novel technique whereby a second laser-induced breakdown plasma is used as a probe, to directly visualise the propagation of the shock generated by the principal breakdown plasma, and to confirm the existence of the low density cavity formed in its wake. In high-speed Schlieren images, we observe a Mach reflection of shocks, formed by the two-lobe plasma kernel of the principal breakdown plasma, whose enhanced strength is linked to the asymmetrical fluid flow necessary for the development of a toroidal plasma.

3.1 Introduction

In our studies on the development of toroidal helium plasmas generated by a single laser-induced breakdown plasma, the low density cavity generated by this breakdown plasma turned out to be a pivotal element. The existence of this cavity has been made plausible by our model presented in section 2.5, which provided a characteristic time scale at which structure is expected to develop, and in the same section, albeit indirectly, by measurements of the density of helium atoms in the centre of the toroidal plasma.

The repletion of the low density cavity plays a formative role, and we observed that a slight asymmetry in the plasma kernel results in a slightly imbalanced fluid flow along the symmetry axis. However, it remained unanswered why the symmetry of the fluid flow necessary for the development of a toroidal plasma, is so severely broken.

In this chapter we present two methods that have been used to directly visualise the low density cavity. In addition to standard high-speed Schlieren imaging,¹ we visualise the propagation of the shock

The work presented in this chapter is in preparation for publication in the *Journal of Plasma Physics*.

¹ Settles 2001.

generated by the principal breakdown plasma, and confirm the existence of the low density cavity formed in its wake, using a novel technique whereby a second laser-induced breakdown plasma has been used as a probe. This successive breakdown plasma has been generated by a second high power Nd:YAG laser.

In the presented high-speed Schlieren images, we observe a Mach reflection of shocks, formed by the two-lobe plasma kernel of the principal breakdown plasma, and link the enhanced strength of Mach reflections to the asymmetrical fluid flow necessary for the development and successive splitting of the toroidal plasmas.

3.2 Shocks and successive laser pulse experiments

In figure 3.1 we present images that have been obtained using the aforementioned technique whereby a second laser-induced breakdown plasma is used as a probe. At the time of interest, and delayed with respect to the principal breakdown laser pulse, a second breakdown plasma is created by a second high power Nd:YAG laser. The creation and subsequent evolution of this plasma is highly sensitive to the local number density, which is dictated by the principal breakdown plasma. Plasma creation is even completely suppressed in regions of low density. In figure 3.1, at zero delay, both breakdown plasmas can be observed simultaneously. When the delay is increased, the edge of the low density

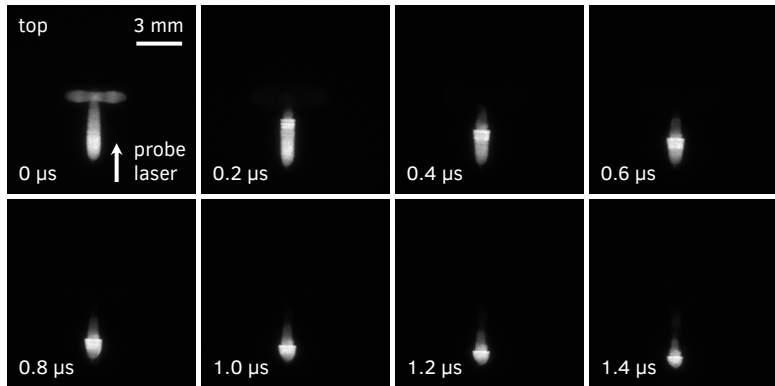


Figure 3.1: Propagation of a shock generated by a laser-induced breakdown plasma, visualised using a second laser-induced breakdown plasma as a probe. The top view images have been captured at increasing times after the principal breakdown laser pulse. Simultaneously, a second breakdown plasma has been created to visualise the shock, which manifests itself in the sharp and clear edge visible in the second breakdown plasma. Note that at 0 μs both the principal and second breakdown plasmas are visible. The images have been individually normalised to their maximum intensity. Principal laser pulse energy: 275 mJ, focal length focussing lens: 50 mm, helium gas pressure: 1000 mbar, bandpass filter: none, ICCD camera image averaging: 10, ICCD camera gate width: 2 ns.

cavity, which manifests itself in the sharp and clear edge visible in the second breakdown plasma, propagates in the subsequent images.

In the presented images, the second breakdown plasma has been created at a distance to the principal breakdown plasma, but when the second plasma would have been created at the same position as the principal plasma, it is completely suppressed for a range of delays. This suppression was already observed during the density measurements presented in section 2.5, and is likewise reported in the literature.²

The propagating shock generated by a laser-induced breakdown plasma resembles the blast wave generated by a nuclear explosion,³ and is likewise observed in supernova remnants.⁴ Basic blast wave theory was independently proposed by Taylor, Von Neumann, and Sedov,⁵ and assumes an instantaneous energy release into an infinitesimally small volume. Following the energy release, the motion of the shock is described by a power-law time dependence, which for spherical symmetry takes the form of a $t^{0.4}$ dependence.⁶

In figure 3.2 we present the position of the propagating shock that has been visualised in figure 3.1, together with its shock Mach number. The position of the shock has been fitted against a power-law and shows that

² Bak, Im et al. 2014; Bak, Wermer et al. 2015.

³ G. I. Taylor 1950a; G. I. Taylor 1950b; Bethe et al. 1958.

⁴ Shu 1992, p. 230; Cioffi 1990.

⁵ G. I. Taylor 1950a; Bethe et al. 1958; Sedov 1959.

⁶ Sedov 1959, p. 213; Zel'dovich et al. 1966, p. 93; G. I. Taylor 1950a.

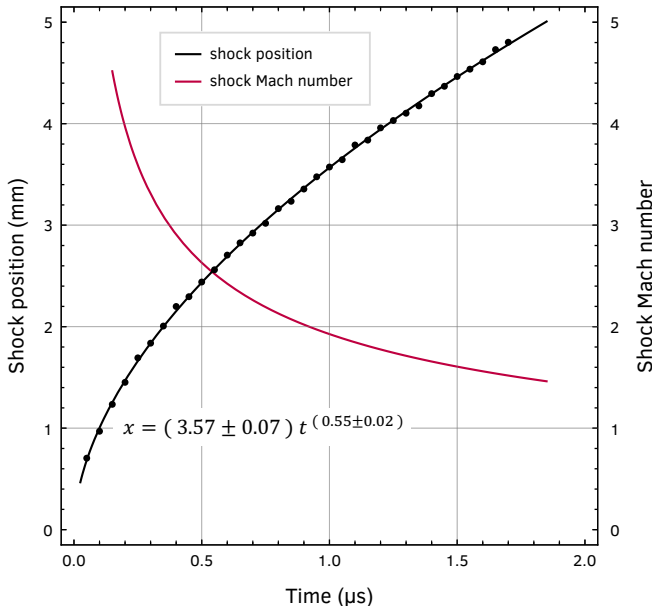


Figure 3.2: Shock position and shock Mach number derived from the visualised shock propagation presented in figure 3.1. The shock position (black dots) has been fitted against a power-law function (black line) and the shock Mach number (purple line) has been obtained by differentiation of the fitted shock position. The speed of sound in the present experimental setting is approximately 1020 m/s.

the shock propagates with an exponent of 0.55 ± 0.02 . The discrepancy with blast wave theory can be explained from the observation that our plasma kernel exhibits a two-lobe structure, which rudimentary can be seen as a two-dimensional explosion, where a $t^{0.5}$ dependence is expected.⁷ Moreover, blast wave theory assumes an instantaneous energy release and neglects internal heat transfer phenomena, including radiation and ionisation, both of which require more sophisticated models.⁸ Earlier studies reported a time dependence of $t^{0.6}$ during the interval between breakdown and the end of the laser pulse,⁹ and a t^1 dependence can be observed during the free expansion phase of a supernova remnant.¹⁰ If we interpret our $t^{0.55}$ dependence as the signature of a driven and reinforced shock, the relaxation of meta-stable helium atoms might be the source of the driving energy.

The shock Mach number presented in figure 3.2 has been obtained by differentiation of the fitted shock position, and during the early expansion speeds of up to Mach 4 can be observed. The speed of sound in the present experimental setting is approximately 1020 m/s. When the shock Mach number becomes equal to one, this marks the end of the shock expansion, and the shock proceeds at sonic speeds.¹¹ For the shock Mach number presented in figure 3.2 this occurs at $4.3 \mu\text{s}$, which qualitatively matches the characteristic time scale of $6.7 \mu\text{s}$ found using our model presented in section 2.5.

Similar to the method used to visualise the propagating shock, we can visualise the entire shock by sweeping the second breakdown plasma through the shock. In figure 3.3 we present

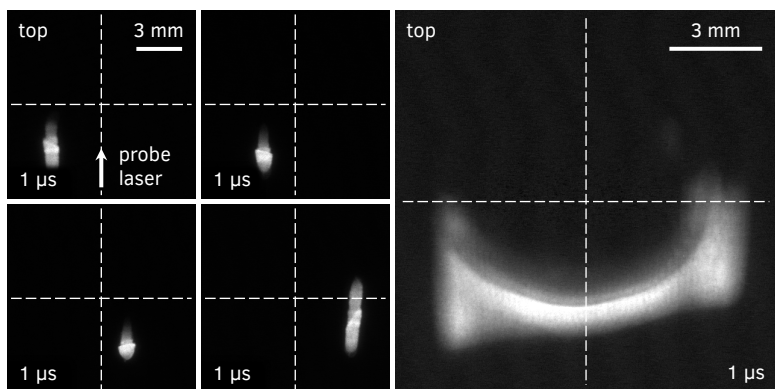


Figure 3.3: Shock generated by a laser-induced breakdown plasma visualised using a second laser-induced breakdown plasma as a probe. (left quartet) The top view images have been captured $1 \mu\text{s}$ after the principal breakdown laser pulse while sweeping the second breakdown plasma through the shock. (right) The entire shock has been visualised by combining all captured images. The images have been individually normalised to their maximum intensity and are based on recordings captured using identical experimental settings as those presented in figure 3.1.

these measurements for a delay of $1 \mu\text{s}$. By combining all individually captured images, we obtain a representative image of the shock. Note that only half of the low density cavity is visible because of the limited extent of the breakdown plasma created by the second laser.

Complementary to the novel visualisation technique presented above, we visualised the expanding low density cavity, and thereby the propagating shock, using high-speed Schlieren imaging. This technique is sensitive to the first derivative of the density, in the direction normal to a knife edge positioned at the shared focal plane of the $4f$ lens system used for imaging the side of the toroidal plasma.¹² In figure 3.4 we present these Schlieren images. Note that in the bottom half of the figure, the breakdown plasma has been moved out of sight, to the right of the image, to be able to image the propagating shock at later times.

¹² Settles 2001.

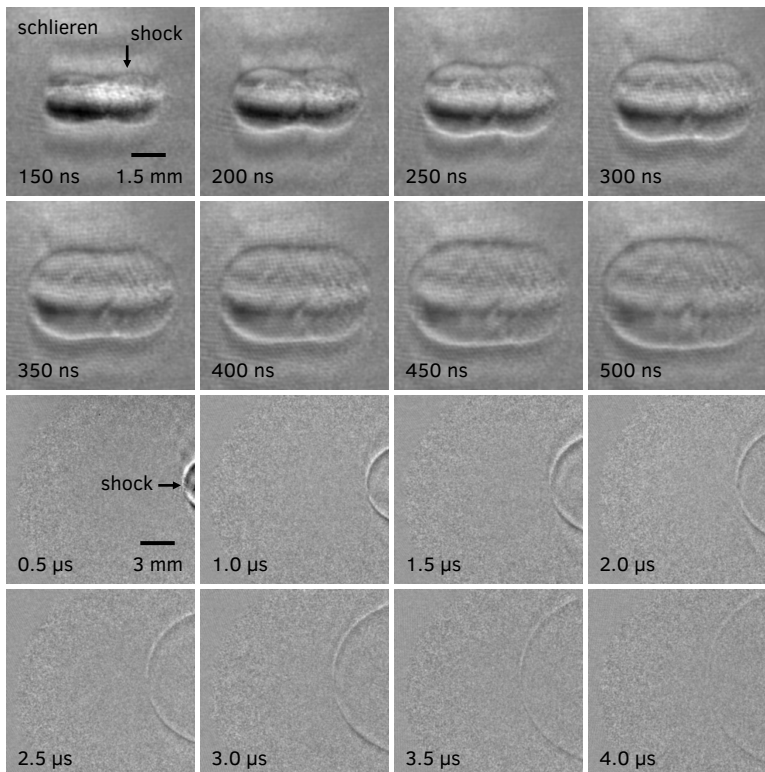


Figure 3.4: Propagation of a shock generated by a laser-induced breakdown plasma, visualised using high-speed Schlieren imaging with a helium-neon laser source. Note that in the bottom half of the figure the breakdown plasma has been moved out of sight to the right of the image. The images have been captured at increasing times after the breakdown laser pulse and are corrected for the remaining plasma emission still visible through the Schlieren imaging system (see text for details). This correction is not perfect as is apparent from the structure still visible within the shock. The images are based on recordings captured using similar experimental settings as those presented in figure 3.1.

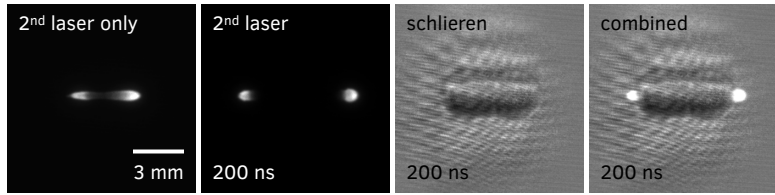


Figure 3.5: Plasma and high-speed Schlieren images have been combined (right) to show that a second laser-induced breakdown plasma (2^{nd} laser) is created on the edge of a shock (schlieren) generated by a laser-induced breakdown plasma created earlier (not shown). Without a previously generated breakdown plasma the second breakdown plasma shows its regular two-lobe structure (2^{nd} laser only).

The presented Schlieren images have been corrected for the remaining plasma emission still visible through the helium-neon laser line filter, by subtracting images that have been captured while the helium-neon laser of the Schlieren imaging system was switched off. This process is not perfect, as is apparent from the structure resembling the two-lobe plasma kernel, still visible within the shock.

We end this section by presenting an experiment where we combine images of a laser-induced breakdown plasma with high-speed Schlieren images of a shock, generated by a laser-induced breakdown plasma created earlier. When we compare the leftmost two images in figure 3.5, obtained respectively with and without the first breakdown plasma present, we observe that the second breakdown plasma is expelled outward. The combined plasma and high-speed Schlieren image shows that the second plasma is expelled outward, exactly to the point where the shock separates the low density cavity from the ambient gas.

3.3 *Mach reflection and laser-induced breakdown plasmas*

When we revisit the plasma kernel images presented in figure 2.26, and the radiant intensity of these images in figure 2.27, we observe that around 54 ns the plasma emission is at its brightest. Precisely at this moment, the plasma kernel exhibits a two-lobe structure consisting of two almost isolated bright plasmas. These two bright lobes are two high pressure and high temperature plasmas, both rapidly expanding and both leading to the formation of a shock. The imprint of these two lobes was already visible in the high-speed Schlieren images presented in figure 3.4, most notably around 250 ns, where we can observe two overlapping spherical shocks.

We reproduced this Schlieren image in figure 3.6. A notable feature that can be observed is a Mach reflection. At a sufficiently oblique

intersection of two shocks, a new third shock is generated, which has a higher strength and which propagates faster than the primary shocks.¹³ The two shocks join to form a third shock, the Mach reflection. Because the Mach reflection significantly increases the strength of the shock, it was studied by Reines and Von Neumann to determine the optimum height of burst of an atomic bomb, to provide the greatest possible destructive effect on the ground.¹⁴

In figure 3.6 we also reproduced, alongside our high-speed Schlieren image of the two interacting shocks, a historical image by Mach et al.,¹⁵ and their resemblance is striking. In their measurements, Mach et al. visualised the interaction of two almost spherical shocks, generated using two electric sparks.

With the obtained insights we revisit the numerical studies on the onset and dynamics of plasma kernels,¹⁶ and reproduce a selection of their simulations in figure 3.7. Although slightly asymmetric, these images also show a striking similarity with our high-speed Schlieren image, and hence with the shock interaction imaged by Mach et al. These simulations show that a Mach reflection indeed represents a stronger and more dense shock, as is noted by the authors,¹⁷ but they have not identified it as a Mach reflection. In a laser-induced breakdown spectroscopy study,¹⁸ a Mach reflection due to the reflection of a shock on a brass surface has been identified.

The fact that a Mach reflection represents a stronger shock, provides

¹³ Krehl and Van der Geest 1991.

¹⁴ Krehl and Van der Geest 1991; Glasstone et al. 1977.

¹⁵ Mach et al. 1890; Krehl 2011, p. 97.

¹⁶ Alberti, Munafò, Pantano et al. 2019a; Alberti, Munafò, Pantano et al. 2019b; Alberti, Munafò, Koll et al. 2020.

¹⁷ Alberti, Munafò, Pantano et al. 2019a.

¹⁸ Cristoforetti et al. 2006.

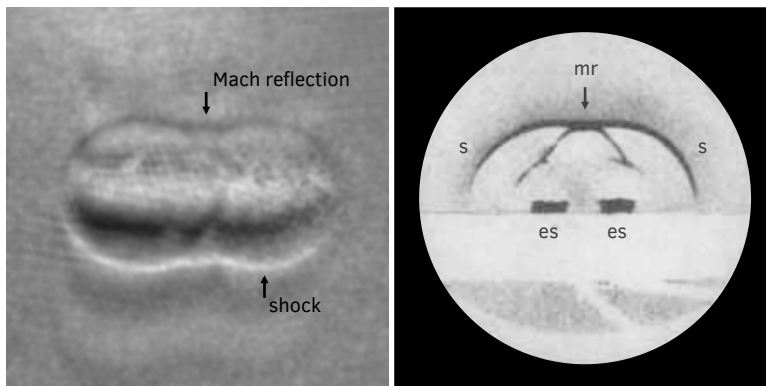


Figure 3.6: Mach reflection due to the interaction of two shocks generated by the two-lobe plasma kernel of a single laser-induced breakdown plasma created in atmospheric pressure helium gas. (left, reproduced from figure 3.4) High-speed Schlieren image of a breakdown plasma captured 250 ns after the breakdown laser pulse. (right) The very first ever visualisation by Ernst Mach of the interaction of two shocks and generation of a Mach reflection. Mach et al. generated the two nearly spherical shocks (s) using two electric sparks (es) near a glass plate. The interacting shocks generate a third shock known as a Mach reflection (mr). This image is reproduced from Mach et al. 1890, with permission of John Wiley and Sons. Copyright 1890 Wiley-VCH Verlag.

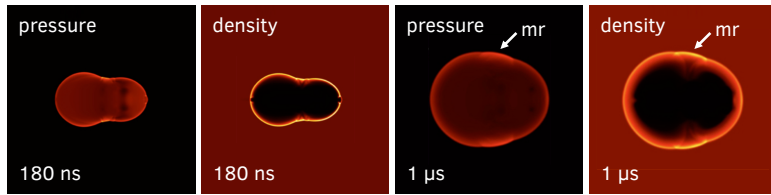


Figure 3.7: Mach reflection visualised by a simulation of the plasma kernel. (left pair) Pressure and density images from early in the development of a plasma kernel. Although slightly asymmetric the images strikingly resemble the high-speed Schlieren image presented in figure 3.6. (right pair) Pressure and density images of a further developed plasma clearly showing the Mach reflection (mr). The images are not to scale. For a numerical interpretation of the images we refer to the original publication. These images are reproduced from Alberti, Munafo, Pantano et al. 2019a, with permission of the American Institute of Aeronautics and Astronautics.

an explanation for the asymmetric fluid flow repleting the low density cavity, which is necessary for our understanding of the development of toroidal plasmas. The higher intensity of the Mach reflection breaks the symmetry, and as a consequence the repleting fluid flow orthogonal to the symmetry axis commences at a later time.

3.4 Conclusion

In this chapter we examined the low density cavity that proved to play a pivotal role in the development of laser-generated toroidal plasmas.

We directly confirmed the existence of this low density cavity using high-speed Schlieren imaging, and presented a novel technique in which we used a second laser-induced breakdown plasma as a probe.

Using this technique, we directly visualised the propagating shock formed by the laser-induced breakdown plasma, and confirmed the existence of the low density cavity in its wake. We found that the motion of the shock is described by a power-law time dependence with an exponent of 0.55 ± 0.02 , approximately corresponding to the behaviour of a two-dimensional explosion.

The two-lobe structure of the plasma kernel is found to generate two spherical shocks. A novel interpretation shows that these shocks interact to generate a Mach reflection. The enhanced strength of this Mach reflection provides an explanation for the asymmetric fluid flow necessary for the development of toroidal plasmas.

4

Microwave analysis of transient toroidal helium plasmas

We experimentally studied laser-generated, atmospheric pressure, transient toroidal helium plasmas using 57 GHz microwave radiation. By combining interferometric measurements with detailed full-wave finite-element calculations, we estimate, with sub-microsecond temporal resolution, the electron number density and the electron collision rate, for the entire evolution of a toroidal plasma. We discuss in detail the microwave interferometric set-up used to measure the complex transmission coefficient, and explain a method whereby the finite-element calculations are used as a map between the measured transmission coefficient and the desired plasma parameters. We briefly discuss an improvement of this method by which a tomographically reconstructed, poloidal intensity profile, based on optical recordings, can be used to better model the toroidal plasma in the finite-element calculations.

4.1 Introduction

In the previous chapters we have examined self-organising toroidal plasmas, generated by a laser-induced breakdown plasma in quiescent atmospheric pressure helium gas at room temperature. We proposed that these transient toroidal helium plasmas might be a first step towards the experimental realisation of self-organising knotted magnetic structures in plasma.¹ Furthermore, the apparent universality of these structures suggests that they may provide the sought after stability in magnetic confinement fusion experiments, and that they might emerge naturally in astrophysical environments.²

The prime plasma parameters of interest in any plasma experiment are the electron number density and the electron collision rate. In this chapter, aimed at obtaining these parameters for the entire evolution of our transient toroidal helium plasma, we present interferometric measurements using 57 GHz microwave radiation, and detailed full-

¹ See section 2.1.

² Smiet 2017; Smiet, de Blank et al. 2019.

wave finite-element calculations of our interferometric set-up.

The microwave interferometric measurements encode information on the complex permittivity of our toroidal plasma, from which we can derive an estimate of the electron number density and the electron collision rate using the Drude-Lorentz model for electrical conductivity.

Alternative techniques that complement the microwave techniques presented here are Rayleigh and Thomson scattering.³ Motivated by the expertise present in our group we opted to use microwave technology. Although the spatial resolution is not expected to be comparable to that of Rayleigh and Thomson scattering, which additionally provides information on the electron temperature in a more direct fashion, our choice was equally motivated by our long-term objective to sustain the toroidal plasma through heating using microwave technology. We do expect that our method will depend very critically on the geometry of the plasma when cut-off electron densities are encountered.

The biggest challenges in our study of transient toroidal helium plasmas are their limited lifetime, which is considerably less than 100 μs , and their limited size, which is of the same order of magnitude as the wavelength of the utilised microwave radiation. The latter implies that the complex transmission coefficient measured by the microwave interferometer depends in a non-trivial way on the complex permittivity of the toroidal plasma.

Our⁴ approach to solving these two difficulties is to combine the interferometric measurements with detailed full-wave finite-element calculations. We will discuss the microwave interferometric set-up used to measure the complex transmission coefficient in detail first, and then explain a method whereby the finite-element calculations are used as a map between the measured transmission coefficient and the sought after plasma parameters.

In our calculations of the complex transmission coefficient we have approximated the toroidal plasma by a torus of fixed size and uniform complex permittivity. In further simplifying our calculations, we used tori of two sizes that are representative for the evolution of our toroidal plasma. For each of these different sized tori, full-wave finite-element calculations have been performed for a range of values for the complex permittivity, or equivalently, for a range of electron number densities and electron collision rates.

These simplifications obviously are a course approximation, but it does provide us with a tractable means to obtain an estimate for the plasma parameters with high temporal resolution. To improve upon this we suggest a method by which a tomographically reconstructed,

³ Pokrzywka et al. 2012; Nedanovska et al. 2015.

⁴ The described method for determining the electron number density and electron collision rate was developed by F.M.A. Smits and has been implemented and utilised in close collaboration with the author of this dissertation.

poloidal intensity profile, based on optical recordings, can be used to better model the toroidal plasma in the finite-element calculations.

The toroidal plasmas studied in this work have been generated by a single laser-induced breakdown plasma, in quiescent atmospheric pressure helium gas at room temperature, using a laser pulse energy of 250 mJ.

4.2 *Electromagnetic waves in plasma*

Prior to concentrating on the measurement techniques employed to determine the plasma parameters of the toroidal plasma, it is instructive to introduce some fundamental concepts from plasma physics, and discuss in a more general manner the propagation of electromagnetic waves in plasma.

Plasma oscillations

One of the intricate properties of plasma is the rapid oscillation of its electrons.⁵ The origin of these plasma oscillations can be understood⁶ by considering electrons that are displaced with respect to the uniform ion charge density. It is assumed that, because of their larger mass, the ions form a uniform and stationary charge density. As a consequence of the electron displacement, the resulting electric field will accelerate the electrons back to their original position. However, due to their acquired momentum, the electrons will overshoot and start to oscillate around their equilibrium position, with a characteristic frequency known as the plasma frequency. We can express this mathematically as follows.

The balance of momentum⁷ for the electron fluid in a cold plasma⁸ is given by

$$m_e n_e \frac{D\mathbf{u}_e}{Dt} = -en_e E \quad (4.1)$$

where m_e is the electron mass, n_e the electron number density, \mathbf{u}_e the electron fluid velocity, e the elementary charge, E the electric field, and $D/Dt = \partial/\partial t + \mathbf{u}_e \cdot \nabla$ the material derivative. In this equation we recognise Newton's second law of motion and the Lorentz force in absence of a magnetic field.

We assume that the electron density n_e can be separated into an equilibrium density n_0 and a small density perturbation n_1 . Then the electric field is given by

$$\nabla \cdot \mathbf{E} = -\frac{e}{\epsilon_0} n_1. \quad (4.2)$$

⁵ Tonks et al. 1929.

⁶ Here we loosely follow F. F. Chen 1974, p. 70; Wesson 2004, p. 38.

⁷ Chorin et al. 1993, p. 6.

⁸ For a cold plasma the $-\nabla p$ pressure term in the balance of momentum is negligible.

After taking the divergence of equation 4.1 and eliminating $\nabla \cdot E$ through equation 4.2 we have

$$m_e \frac{\partial}{\partial t} \nabla \cdot \mathbf{u}_e = \frac{e^2}{\epsilon_0} n_1 \quad (4.3)$$

where the quadratic term $(\mathbf{u}_e \cdot \nabla) \mathbf{u}_e$ originating from the material derivative has been neglected as a consequence of our perturbative approach.

⁹Chorin et al. 1993, p. 11.

The conservation of mass⁹ for the electron fluid is given by

$$\frac{D}{Dt} m_e n_e + m_e n_e \nabla \cdot \mathbf{u}_e = 0. \quad (4.4)$$

When we realise that $\partial n_0 / \partial t = 0$ and $\nabla n_0 = 0$, and neglect quadratic terms, then we may write

$$\frac{\partial n_1}{\partial t} + n_0 \nabla \cdot \mathbf{u}_e = 0. \quad (4.5)$$

Substitution of $\nabla \cdot \mathbf{u}_e$ from equation 4.5 into equation 4.3 results in the differential equation of a simple harmonic oscillator for the electron density perturbation n_1

$$\frac{\partial^2 n_1}{\partial t^2} = -\omega_p^2 n_1$$

where ω_p is the plasma frequency given by

$$\omega_p \equiv \sqrt{\frac{n_0 e^2}{\epsilon_0 m_e}}. \quad (4.6)$$

Note that we cannot explain the plasma oscillations from single particle motion alone, it is necessary to consider the electrons as a fluid. This can be understood when we realise that although the electric field is created as a result of a small perturbation n_1 it is the whole electron fluid with density n_0 that will be set in motion. The plasma frequency therefore only depends on the equilibrium electron number density n_0 . It is one of the most fundamental parameters of plasma physics.

Drude-Lorentz model for electrical conductivity

In deriving the plasma frequency we have neglected collisions between electrons and ions, and between the electrons themselves for that matter. These collisions however are responsible for many intricate plasma transport processes, and electrical conductivity is one of them. Without diving into a detailed discourse explaining electrical conductivity, it is possible to convey the essentials through an elementary model first

proposed by Drude.¹⁰

Let us assume once more that, because of their larger mass, the ions form a uniform and stationary density. The electrons will consequently be solely responsible for the transport of electrical current through the plasma. Electrical conductivity manifests itself most recognisable through Joule heating, where the electrons, through collisions, lose kinetic energy to the ions and neutrals. Assume there is some unknown instantaneous collision mechanism maintaining local thermodynamic equilibrium, and that the probability per unit time for such a collision to take place equals $1/\tau$. Maintaining local thermodynamic equilibrium simply means that immediately after each collision, the electron velocity is solely prescribed by the local temperature and is therefore independent of the velocity just before the collision. Further assume that between collisions the electrons only interact with an externally applied electric field and that other interactions can be neglected.¹¹

The assumption of local thermodynamic equilibrium implies that the momentum lost per electron per collision is equal to $m_e \mathbf{u}_e$. We also assumed that the probability per unit time an electron experiences a collision is equal to $1/\tau$ implying a relaxation or collision time of τ . Consequently, the rate of change of momentum of the electron fluid is given by $m_e n_e \mathbf{u}_e / \tau$. The balance of momentum for the electron fluid for a cold plasma is then given by¹²

$$m_e n_e \frac{D\mathbf{u}_e}{Dt} = -en_e \mathbf{E} - \frac{m_e n_e \mathbf{u}_e}{\tau}.$$

This equation simply states that the effect of the electron collisions is to introduce a frictional damping term, in addition to the electromagnetic driving term introduced in the derivation of the plasma frequency. Using the conservation of mass given by equation 4.4 we have¹³

$$\begin{aligned} \frac{\partial}{\partial t} (m_e n_e \mathbf{u}_e) &= -\nabla \cdot (m_e n_e \mathbf{u}_e) \mathbf{u}_e \\ &\quad - m_e n_e (\mathbf{u}_e \cdot \nabla) \mathbf{u}_e - en_e \mathbf{E} - \frac{m_e n_e \mathbf{u}_e}{\tau}. \end{aligned}$$

Neglecting quadratic terms in \mathbf{u}_e and assuming that the electron density n_e equals the equilibrium electron density n_0 results in

$$\frac{\partial}{\partial t} (m_e n_0 \mathbf{u}_e) = -en_0 \mathbf{E} - \frac{m_e n_0 \mathbf{u}_e}{\tau}.$$

Since the current density \mathbf{j} is defined as $\mathbf{j} \equiv -en_0 \mathbf{u}_e$ we may write

$$\frac{\partial}{\partial t} \mathbf{j} = \epsilon_0 \omega_p^2 \mathbf{E} - \frac{\mathbf{j}}{\tau}$$

where ω_p is the plasma frequency defined in equation 4.6. When we

¹⁰ Drude 1900.

¹¹ The electron-ion interaction is not completely neglected, it is still implicitly assumed that the electrons remain confined to the quasi-neutral plasma. See Ashcroft et al. 1976, p. 4.

¹² F. F. Chen 1974, p. 56.

¹³ Chorin et al. 1993, p. 7.

¹⁴ Throughout this chapter we use the quantum mechanical sign convention, where a wave propagating in the k direction for $\omega > 0$ is represented by $e^{ik \cdot x - i\omega t}$.

assume that solutions have a harmonic time dependence $e^{-i\omega t}$ we can write $E(t) = E e^{-i\omega t}$ and $j(t) = j e^{-i\omega t}$, and find that¹⁴

$$j = \sigma(\omega)E$$

which is Ohm's law of electrical conductivity, where $\sigma(\omega)$ is the electrical conductivity given by

$$\sigma(\omega) = \frac{\sigma_0}{1 - i\omega\tau} \quad \text{where} \quad \sigma_0 = \epsilon_0 \omega_p^2 \tau = \frac{n_0 e^2 \tau}{m_e}. \quad (4.7)$$

At zero frequency, the electrical conductivity $\sigma(\omega)$ reduces to the direct-current Drude conductivity σ_0 .

Electromagnetic waves in linear media

The propagation of electromagnetic waves is an extensive subject about which many works have been written.¹⁵ For the purpose of this section we will only consider the propagation of plane electromagnetic waves in linear media and underline the equivalence of describing linear media by, for example, the dispersion relation, the complex permittivity, or the electrical conductivity.

¹⁵ See for example Jackson 1998; Griffiths 1999, and references therein.

For uniform isotropic linear media the Maxwell equations¹⁶ for a charge-free infinite medium are

¹⁶ Jackson 1998, pp. 238 and 295. For uniform isotropic linear media the commonly used fields D and H can be written as $D = \epsilon E$ and $B = \mu H$. In that context H is called the magnetic field and B is called the magnetic induction.

$$\begin{aligned} \nabla \cdot E &= 0 & \nabla \times E &= -\frac{\partial B}{\partial t} \\ \nabla \cdot B &= 0 & \nabla \times B &= \mu j + \mu \epsilon \frac{\partial E}{\partial t} \end{aligned}$$

where the permeability μ and the permittivity ϵ describe our linear medium and may in general be complex functions. When we assume that solutions have a harmonic time dependence $e^{-i\omega t}$ we can write $E(t) = E e^{-i\omega t}$, $B(t) = B e^{-i\omega t}$ and $j(t) = j e^{-i\omega t}$, and the Maxwell equations turn into

$$\begin{aligned} \nabla \cdot E &= 0 & \nabla \times E &= i\omega B \\ \nabla \cdot B &= 0 & \nabla \times B &= \mu j - i\mu \epsilon \omega E. \end{aligned}$$

When we take the curl of the equation for $\nabla \times E$ and eliminate $\nabla \times B$, then we can write

$$\nabla \times (\nabla \times E) = \mu \epsilon \omega^2 E + i\mu \omega j.$$

Using the vector calculus identity $\nabla \times (\nabla \times A) = \nabla(\nabla \cdot A) - \nabla^2 A$,

realising $\nabla \cdot \mathbf{E}$ is equal to zero, and substituting Ohm's law of electrical conductivity^{17,18} $\mathbf{j} = \sigma(\omega)\mathbf{E}$, we arrive at the Helmholtz wave equation

$$\nabla^2 \mathbf{E} + \mu\epsilon \left(1 + i \frac{\sigma}{\epsilon\omega}\right) \omega^2 \mathbf{E} = 0.$$

A possible solution is a plane electromagnetic wave $e^{i\mathbf{k}\cdot\mathbf{x}-i\omega t}$ propagating in the \mathbf{k} direction for $\omega > 0$. From the Helmholtz wave equation we then find the requirement that the wave number $k = |\mathbf{k}|$ and the frequency ω are related by

$$k^2 = \mu\epsilon \left(1 + i \frac{\sigma}{\epsilon\omega}\right) \omega^2.$$

This is the dispersion relation for electromagnetic waves propagating in uniform isotropic linear media.

Generally, a dispersion relation relates the wave number k of a propagating wave to its frequency ω , and is universally written as $\omega(k) = v(k)k$, where $v(k)$ is the propagation speed or phase velocity.¹⁹ It is important to realise that the propagation of electromagnetic waves in linear media is completely determined by the dispersion relation and that it represents all properties of our linear medium, regardless of whether they originate from the permeability μ , the permittivity ϵ , or the electrical conductivity σ . It is merely a choice by which measure we wish to represent our linear medium.

As an example, assume our medium lacks both polarisation as well as magnetic²⁰ properties, implying $\epsilon = \epsilon_0$ and $\mu = \mu_0$, and that we opt to represent its electrical conductivity σ solely by an equivalent complex permittivity $\tilde{\epsilon}$, hence $\tilde{\mu} = \mu_0$ and $\tilde{\sigma} = 0$. Then we can write the dispersion relation of our medium and its equivalent representation respectively as

$$k^2 = \mu_0\epsilon_0 \left(1 + i \frac{\sigma}{\epsilon_0\omega}\right) \omega^2$$

and

$$k^2 = \mu_0\tilde{\epsilon}\omega^2. \quad (4.8)$$

Evidently we have

$$\tilde{\epsilon} = \epsilon_0 \left(1 + i \frac{\sigma}{\epsilon_0\omega}\right) \quad (4.9)$$

which provides an equally apt representation of our electrically conductive linear medium in terms of an equivalent complex permittivity.

¹⁷ We assume that a dc magnetic field is absent so Ohm's law may be applied. In the presence of a dc magnetic field this is no longer true as the Hall effect and magneto-resistance become important.

¹⁸ The Drude-Lorentz model has been derived assuming a constant electric field \mathbf{E} . It is not evident that the electrical conductivity thus found is applicable in our context of a spatially varying electric field. However, if the electric field does not vary appreciably over distances comparable to the electron mean free path, we can write the current density \mathbf{j} as $\mathbf{j}(\mathbf{r}, \omega) = \sigma(\omega)\mathbf{E}(\mathbf{r}, \omega)$. See Ashcroft et al. 1976, p. 17.

¹⁹ An associated quantity, the complex refractive index n , relates the propagation speed in free space ($\mu = \mu_0$, $\epsilon = \epsilon_0$, and $\sigma = 0$) to the propagation speed in the linear medium, and can be defined through $n \equiv k/k_0$, where $k_0 \equiv \omega\sqrt{\mu_0\epsilon_0}$ is the wave number in free space. Because k and n are on an equal footing, for the sake of clarity, we deliberately omit the complex refractive index n .

²⁰ In magnetic media the permeability μ is no longer equal to the permeability μ_0 of free space as a result of the induced magnetisation in response to an external magnetic field.

The wave number k and the equivalent complex permittivity $\tilde{\epsilon}$ are related through the equivalent dispersion relation 4.8 and universally their real and imaginary parts are explicitly written

$$k \equiv k' + i k''$$

$$\tilde{\epsilon} \equiv \tilde{\epsilon}' + i \tilde{\epsilon}''.$$

²¹ In terms of the complex refractive index n introduced earlier we have $n = \sqrt{\tilde{\epsilon}/\epsilon_0}$.

From the equivalent dispersion relation 4.8 we have²¹

$$k = k_0 \sqrt{\frac{\tilde{\epsilon}}{\epsilon_0}}$$

where $k_0 \equiv \omega \sqrt{\mu_0 \epsilon_0}$ is the wave number in free space. The principal square root can be expressed algebraically²² so we can write²³

²² Abramowitz et al. 1972, p. 17.

²³ There exists ambiguity regarding the sign of the imaginary part of the principal square root and the imaginary parts of k and $\tilde{\epsilon}$. Here $k'' > 0$ and $\tilde{\epsilon}'' > 0$ represent loss where the electromagnetic wave attenuates exponentially. Similarly $k' > 0$ represents propagation in the k direction for $\omega > 0$.

$$k' = k_0 \sqrt{\frac{|\tilde{\epsilon}| + \tilde{\epsilon}'}{2 \epsilon_0}} \quad (4.10)$$

$$k'' = k_0 \sqrt{\frac{|\tilde{\epsilon}| - \tilde{\epsilon}'}{2 \epsilon_0}}. \quad (4.11)$$

When considering the propagation of a plane electromagnetic wave, we can assume, without loss of generality, that the propagation is in the x -direction. Then we can write

$$e^{ikx - i\omega t} = e^{i(k' + ik'')x - i\omega t} = e^{-k''x} e^{ik'x - i\omega t}.$$

Evidently our electromagnetic wave attenuates exponentially with attenuation constant k'' while propagating with wave number k' .

Plasma complex permittivity and electromagnetic wave propagation

²⁴ Trivially, we have examined only some of the countless intricate properties of plasma. See F. F. Chen 1974; Bellan 2006; Goedbloed et al. 2004; Kulsrud 2005 for more detailed works. For a condensed matter physics perspective the reader might consult Marder 2010.

In the previous sections we have gained some²⁴ insight into the rapid oscillation of electrons in plasma and the Drude-Lorentz model for electrical conductivity, and appreciated the equivalence in representing uniform isotropic linear media. Here, we will apply these insights to the complex permittivity of plasma and the propagation of electromagnetic waves in plasma.

The electrical conductivity $\sigma(\omega)$ obtained through the Drude-Lorentz model is given by equation 4.7 and can be written as

$$\sigma(\omega) = \frac{\epsilon_0 \omega_p^2 \tau}{1 - i\omega\tau}$$

when we substitute the direct-current Drude conductivity σ_0 . Then the

equivalent complex permittivity $\tilde{\epsilon}$ given by equation 4.9 can be written as

$$\frac{\tilde{\epsilon}}{\epsilon_0} = 1 - \frac{n_0}{n_c} \frac{1}{1 + i \frac{\nu}{\omega}}$$

where we introduced the electron collision rate $\nu \equiv 1/\tau$ and the critical electron number density²⁵ $n_c \equiv \epsilon_0 m_e \omega^2 / e^2$. The real part of the equivalent complex permittivity $\tilde{\epsilon}$ can be written as

$$\frac{\tilde{\epsilon}'}{\epsilon_0} = 1 - \frac{n_0}{n_c} \frac{1}{1 + \left(\frac{\nu}{\omega}\right)^2}$$

while its imaginary part takes the form

$$\frac{\tilde{\epsilon}''}{\epsilon_0} = \frac{n_0}{n_c} \frac{\frac{\nu}{\omega}}{1 + \left(\frac{\nu}{\omega}\right)^2}.$$

The imaginary part makes it evident that a non-zero electron collision rate ν results, as expected, in loss represented by $\tilde{\epsilon}'' > 0$. The behaviour of an electromagnetic wave propagating through the plasma is easily obtained through equations 4.10 and 4.11 relating the real and imaginary parts of k and $\tilde{\epsilon}$.

We conclude this section by presenting in figure 4.1 the normalised²⁶ real and imaginary part k'/k_0 and k''/k_0 of wave number k , as a function of the normalised electron number density n_0/n_c and the normalised electron collision rate ν/ω . From these, two observations are noteworthy.

When electron collisions are negligible ($\nu = 0$) then, for electron number densities larger than the critical density ($n_0 > n_c$), the real part k' becomes zero, while the imaginary part k'' acquires a finite value. The equivalent complex permittivity turns negative, hence the wave number becomes purely imaginary and propagation is not possible. We speak of an evanescent wave. For electron number densities smaller than the critical density ($n_0 < n_c$) wave propagating is lossless with a phase velocity exceeding the speed of light in vacuum.

When electron collisions are present ($\nu \neq 0$) propagation is possible for all electron number densities. Intuitively this can be understood by realising that, due to their collisions, the electrons are limited in their movement and are no longer able to fully respond to the applied electromagnetic field.

²⁵ At a constant frequency ω the equivalent complex permittivity $\tilde{\epsilon}$ becomes zero when the electron number density n_0 is equal to the critical electron number density given by $n_c \equiv \epsilon_0 m_e \omega^2 / e^2$. Precisely at the critical electron number density we have $\omega_p = \omega$. See F. F. Chen 1974, p. 103.

²⁶ In figure 4.1 we normalised to k_0 and essentially present the real and imaginary part of the complex refractive index introduced earlier.

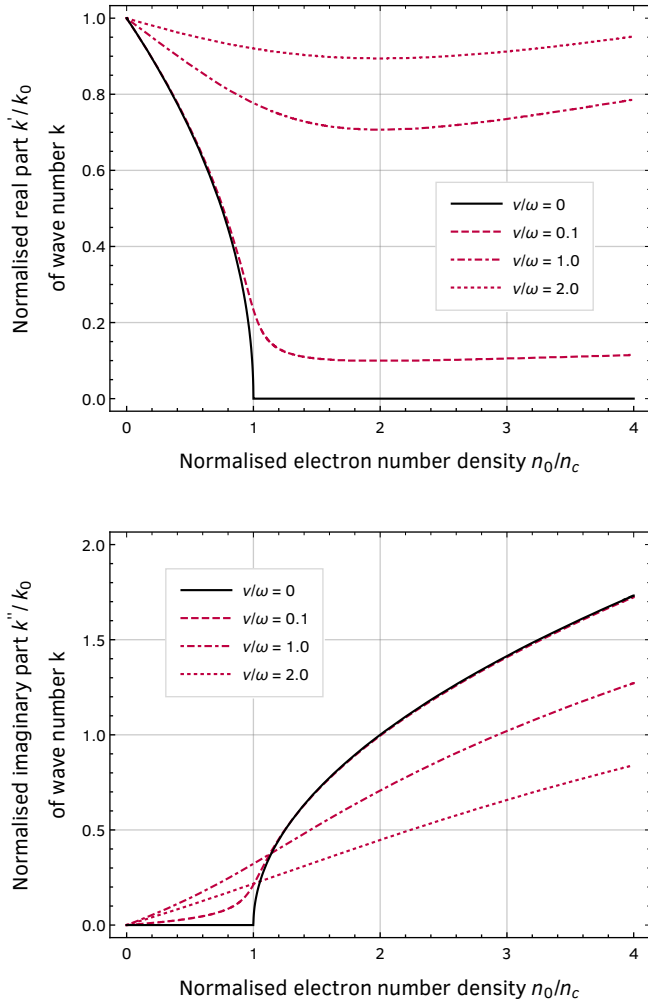


Figure 4.1: Normalised real part k'/k_0 and imaginary part k''/k_0 of wave number k , as a function of the normalised electron number density n_0/n_c and the normalised electron collision rate ν/ω .

4.3 Microwave analysis of transient toroidal helium plasmas

The prime plasma parameters of interest in any plasma experiment are the electron number density and the electron collision rate of the plasma under consideration. In this section we present microwave interferometric measurements at 57 GHz, aimed at obtaining these parameters, with high temporal resolution, for the whole evolution of our transient toroidal helium plasma. These measurements encode

information on the complex transmission coefficient for microwaves traversing our toroidal plasma, which in itself contains information about the complex permittivity of the plasma. From this, we can derive an estimate of the electron number density and the electron collision rate through the Drude-Lorentz model for electrical conductivity.

The propagation of electromagnetic waves through a voluminous plasma is straightforward, and for these plasmas the expressions presented in section 4.2 can be utilised safely to obtain the electron number density and the electron collision rate from the measured complex permittivity of the plasma. Unfortunately, this simple strategy is not applicable to our toroidal plasma. The wavelength of the utilised microwave radiation is 5.3 mm, which is of the same order of magnitude as the size of our toroidal plasma, as can be seen from our measurements presented in section 2.3. The complex transmission coefficient measured by the microwave interferometer therefore depends on the complex permittivity in a non-trivial way.²⁷

Our approach to solving this difficulty is to perform complex transmission measurements using a microwave interferometer, and to subsequently compare these measurements to electromagnetic full-wave finite-element calculations of the interferometric set-up, including a torus mimicking our toroidal plasma. The complex transmission coefficient calculated in this manner for a set of tori, each with a different complex permittivity, can be used as a map to obtain the complex permittivity of our toroidal plasma as a function of time.

Because the finite-element calculations already are computationally intensive, we have approximated our toroidal plasma by a torus of fixed dimensions and uniform complex permittivity. This necessarily is a coarse approximation, but it does provide, with high temporal resolution, a first estimate of the electron number density and the electron collision rate as a function of time.

Examination of the microwave interferometer

A simplified schematic²⁸ of the microwave interferometric set-up is presented in figure 4.2. Microwave radiation, generated using a 57 GHz 100 mW Gunn oscillator, is guided through rectangular TE₁₀ mode wave-guide with dimensions of 3.76 × 1.88 mm, to a 10 dB directional coupler, where it is split into a reference and transmission signal. The reference signal is guided through an adjustable attenuator while the transmission signal is fed into a copper pyramidal horn antenna with an apex-aperture distance of 45 mm and an aperture of 18 × 11 mm.

²⁷ The small separation of the horn antennas used for the transmission measurements further complicates the determination of the complex transmission coefficient, because of multiple reflections of the microwave radiation between these antennas.

²⁸ For a more lively impression of the experimental set-up we refer to photo 2 on page 104.

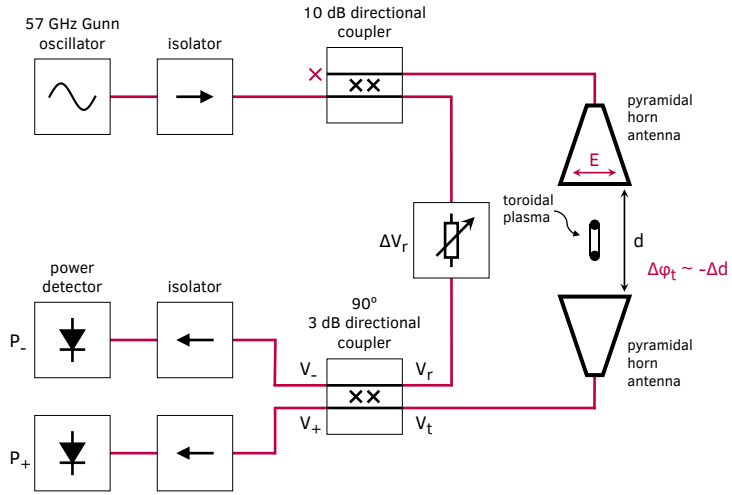


Figure 4.2: Simplified schematic of the microwave interferometric set-up used to measure the complex transmission coefficient of our transient toroidal helium plasma with high temporal resolution. See text for details. For a more lively impression of the experimental set-up we refer to photo 2 on page 104.

This horn antenna couples the microwave radiation into free space, which subsequently traverses the toroidal plasma before it is received by a second identical pyramidal horn antenna. The horn antennas are separated by a distance of 24.3 mm.

The reference and transmission signals are recombined using a 90° 3 dB directional coupler²⁹ whose output ports are equipped with a microwave power detector. The attenuator can be used to reduce the power of the reference signal, while the phase between the reference and transmission signals can be adjusted by changing the distance between the horn antennas. Microwave isolators have been used to prevent interference arising from reflections from the power detectors, the pyramidal horn antennas, and the toroidal plasma. The power detectors have been calibrated to correct for their non-linear power to voltage response.

We note that the whole microwave interferometric set-up has been mounted inside our plasma reactor. Because of the large number of components, degassing becomes an issue and long evacuation times are needed to remove the air from our plasma reactor. This is not the most ideal approach, but it proved to be the most practical means to integrate these measurements into our existing set-up for the generation of toroidal helium plasmas.

The central component of the interferometric set-up is the 90° 3 dB directional coupler. When all ports of a 90° 3 dB directional coupler are

²⁹ A directional coupler designed for a 3 dB power split is known as a hybrid coupler.

connected to matched wave-guides, and microwaves are assumed not to traverse the coupler in the reverse direction, implying ideal microwave isolators, then the voltages of the ports of the coupler are given by^{30,31,†}

$$\begin{bmatrix} V_+ \\ V_- \end{bmatrix} = \frac{1}{\sqrt{2}} \begin{bmatrix} 1 & i \\ i & 1 \end{bmatrix} \begin{bmatrix} V_t \\ V_r \end{bmatrix}$$

where V_+ and V_- are the power detector input voltages, V_t is the transmitted voltage after the microwave radiation has traversed the toroidal plasma, and V_r is the reference voltage. When we assume that the impedances are normalised to 1 Ohm, then for all voltages in our set-up, the time-averaged power is given by $P = \frac{1}{2}|V|^2$. The power received by the microwave detectors is then given by

$$P_+ = \frac{1}{4} |V_t + iV_r|^2$$

$$P_- = \frac{1}{4} |V_t - iV_r|^2.$$

The reference voltage V_r can be obtained in the following manner, while calibrating the interferometric set-up. Let us use a superscript label (cal) to denote an empty interferometer during this calibration. We can adjust the attenuation of the reference signal, and the phase between the reference and transmitted signals, in such a way that detector signal P_- becomes zero, implying we have $V_t^{cal} = iV_r^{cal}$. Consequently we have

$$P_t^{cal} = P_r^{cal} \quad (4.12)$$

and

$$P_+^{cal} = 2P_r^{cal}$$

$$P_-^{cal} = 0.$$

[†] In general the scattering matrix of a 3 dB directional coupler can be written as

$$[S] = \frac{1}{\sqrt{2}} \begin{bmatrix} 0 & 0 & 1 & e^{i\alpha} \\ 0 & 0 & -e^{-i\alpha} & 1 \\ 1 & -e^{-i\alpha} & 0 & 0 \\ e^{i\alpha} & 1 & 0 & 0 \end{bmatrix}$$

where $\alpha \in \mathbb{R}$ defines the phase difference between the output ports. Unfortunately the sign of α is not always known. Moreover, the sign convention used to represent a propagating wave affects the scattering matrix, specifically, a scattering matrix defined in one sign convention is the complex conjugate of the other (see Ye et al. 2018). More about sign conventions can be found in Muller 1969; Atkinson et al. 1992. Here we assume $\alpha = \frac{\pi}{2}$. The sign of α is not important, because in an interferometric set-up, where only the change in phase is relevant, all information can be distilled from the behaviour of the power difference $P_+ - P_-$ as a function of the distance d between the pyramidal horn antennas.

³⁰ Collin 2001, p. 413.

³¹ The matrix in this equation is a reduced scattering matrix, where the matrix elements representing microwaves traversing the directional coupler in the reverse direction have been omitted.

³²In an interferometric set-up only the phase between the reference and transmitted signals is a meaningful quantity.

Without loss of generality³² we may assume V_r^{cal} to be positive real valued, so we can write $V_r^{cal} = \sqrt{2P_r^{cal}} = \sqrt{P_+^{cal}}$.

An ideal directional coupler is a lossless component, therefore conservation of energy implies that $P_+ + P_- = P_t + P_r$. For a calibrated interferometer, the power of the microwave radiation traversing the toroidal plasma, and received by the pyramidal horn antenna, is thus

$$P_t = P_+ + P_- - P_r^{cal}. \quad (4.13)$$

Our toroidal plasma will not only attenuate the microwave radiation, it will also change its phase. This change in phase is encoded in the power difference $P_+ - P_-$ measured by the microwave detectors. Using the complex conjugate properties of complex numbers and realising we assumed V_r^{cal} to be positive real valued, we can derive

$$\text{Im}(V_t) = \frac{P_+ - P_-}{V_r^{cal}} \quad (4.14)$$

where $\text{Im}(V_t)$ denotes the imaginary part of V_t . Because $|V_t| = \sqrt{2P_t}$ the phase of V_t can be readily obtained.

Using the interferometer when P_- is adjusted to zero makes the complex transmission measurement insensitive to the sign of the change in phase. This is evident from the fact that when the phase of V_t changes, the transmitted power, and hence the sum $P_+ + P_-$, does not change. As a consequence, the power difference $P_+ - P_-$ will decrease irrespective of the sign of the change in phase.

Ideally this is resolved by setting up the interferometer in such a way that the power difference $P_+ - P_-$ is zero, which can be accomplished by adjusting the phase between the reference and transmitted signals through adjustment of the distance between the pyramidal horn antennas. In this case we immediately see from equation 4.14 that the sign of the power difference $P_+ - P_-$ will be equal to the sign of the change in phase of the transmitted signal. Experimentally this adjustment does not have to be accurate because, as we will show later, we can correct for a non-zero power difference $P_+ - P_-$ as long as $P_- \neq 0$.

Let us use a superscript zero (o) to denote an empty and calibrated microwave interferometer where the power difference $P_+ - P_-$ has been adjusted to zero. The detector signals so defined can be obtained straightforwardly from the recordings of the detector signals, just before a laser-induced breakdown plasma is generated. Realising that the transmitted power does not change while adjusting its phase, we have

$P_t^0 = P_t^{cal}$. Then, by making use of equations 4.12 and 4.13, we can write

$$P_t^0 = \frac{P_+^0 + P_-^0}{2}. \quad (4.15)$$

If we now normalise all power measurements to $P_t^0 = \frac{1}{2}|V_t^0|^2$ and denote these using a tilde (\sim) and furthermore define the normalised transmitted voltage as $\tilde{V}_t \equiv V_t/|V_t^0|$ we can write³³

$$\begin{aligned} |\tilde{V}_t| &= \sqrt{\tilde{P}_+ + \tilde{P}_- - 1} \\ \text{Im}(\tilde{V}_t) &= \frac{\tilde{P}_+ - \tilde{P}_-}{2}. \end{aligned}$$

The normalised transmitted voltage \tilde{V}_t is easily obtained from these relations and encodes information about the propagation of microwave radiation through our toroidal plasma.³⁴ When corrected for the phase of \tilde{V}_t^0 it is customary to denote this quantity in microwave technology as the complex transmission coefficient S_{21} .

The normalised transmitted voltage \tilde{V}_t is not uniquely defined through $|\tilde{V}_t|$ and $\text{Im}(\tilde{V}_t)$ because the sign of the real part of \tilde{V}_t is not known. In figure 4.3 we illustrate this ambiguity by showing the simulated normalised detector signals \tilde{P}_+ and \tilde{P}_- of a 90° 3 dB directional coupler as a function of the phase between V_t and V_r . The non-zero power difference $\tilde{P}_+^0 - \tilde{P}_-^0$ for the empty and calibrated microwave interferometer has been chosen arbitrarily. It is clear that

³³ Note that due to the chosen normalisation \tilde{V}_t^0 is complex for $P_+^0 - P_-^0 \neq 0$. Furthermore $|\tilde{V}_t^0| = 1$ and $\tilde{P}_t = |\tilde{V}_t|^2$.

³⁴ Due to the small separation of the pyramidal horn antennas, multiple reflections between these antennas inevitably affects the complex transmission coefficient determined in this experiment.

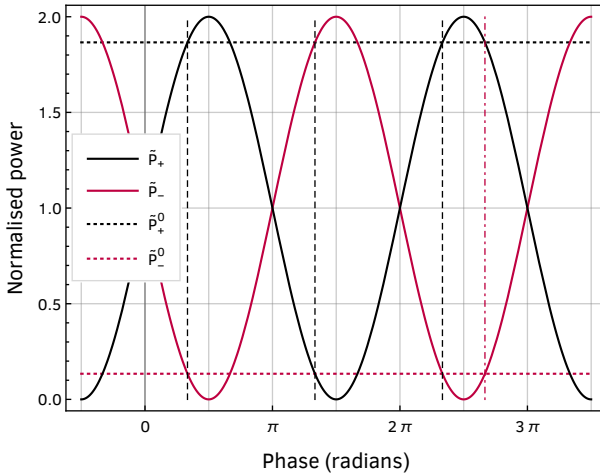


Figure 4.3: Illustration of the ambiguity in the determination of the phase of \tilde{V}_t due to the unknown sign of the real part of \tilde{V}_t . See text for a detailed discussion.

³⁵Note that exchanging the detector signals P_+ and P_- is equivalent to adding π to the phase between V_i and V_r . Furthermore, recall that the exact scattering matrix of the directional coupler, as well as the exact length of the guides, are not known. As a result, only changes in the phase between V_i and V_r due to our toroidal plasma, are a meaningful quantity. Without loss of generality we can therefore assume that $P_+ > P_-$.

the horizontal dashed black line \tilde{P}_+^0 intersects the black sine \tilde{P}_+ at two phase angles, reflecting the two possibilities for the real part of \tilde{V}_i . An experimental analysis of the behaviour of the power difference $\tilde{P}_+ - \tilde{P}_-$ as a function of the distance d between the pyramidal horn antennas will determine whether the real part is positive or negative. When the horn antenna distance is decreased, the phase between V_i and V_r increases. If at the same time $\tilde{P}_+ - \tilde{P}_-$ increases, the real part of \tilde{V}_i is positive.³⁵

Microwave interferometric complex transmission measurements

Using the experimental set-up and method set out in the previous subsection, we performed complex transmission measurements on our transient toroidal helium plasma, generated by a single laser-induced breakdown plasma. These breakdown plasmas have been created in quiescent atmospheric pressure helium gas at room temperature, with a laser pulse energy of 250 mJ, using a 1" plano-convex lens with a focal length of 50 mm. In section 2.3 it has been shown that the evolution of these plasmas is very reproducible. In order to increase the signal to noise ratio, most notably during the faint afterglow, therefore all

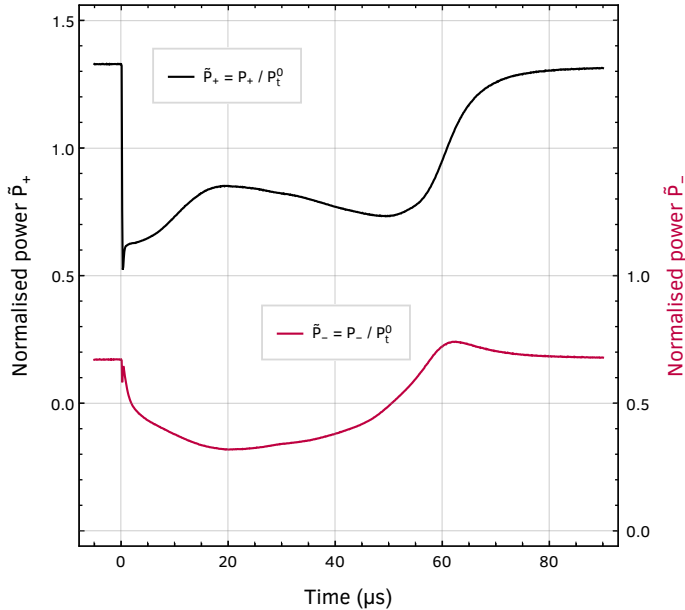


Figure 4.4: Normalised microwave detector signals \tilde{P}_+ and \tilde{P}_- recorded during a complex transmission measurement on a transient toroidal helium plasma, generated by a laser-induced breakdown plasma created in quiescent atmospheric pressure helium gas at room temperature. Laser pulse energy: 250 mJ, focal length focussing lens: 50 mm, helium gas pressure: 1000 mbar, microwave detector signal averaging: 100.

recordings of the microwave detector signals have been averaged over 100 repetitions.

In figure 4.4 we present the recorded microwave detector signals normalised to P_t^0 as defined in equation 4.15. The values for P_+^0 and P_-^0 have been obtained from the same recordings at 0 μs , just before a laser-induced breakdown plasma is created.

From these recordings, the magnitude and phase of the complex transmission coefficient S_{21} have been obtained using the method set out in the previous subsection, and are presented in figure 4.5. The fast response visible at 0 μs indicates that measurements can be obtained with high temporal resolution.

Near the end of the evolution, the complex transmission coefficient is seen to return to unity, with a slightly positive but monotonically decreasing phase. This is expected from an extinguishing plasma because, as was shown in section 4.2, plasma with a small electron number density exhibits a wave number k slightly smaller than k_0 , the wave number in free space.

Together with full-wave finite-element calculations, these complex transmission measurements will be used to provide, with high temporal

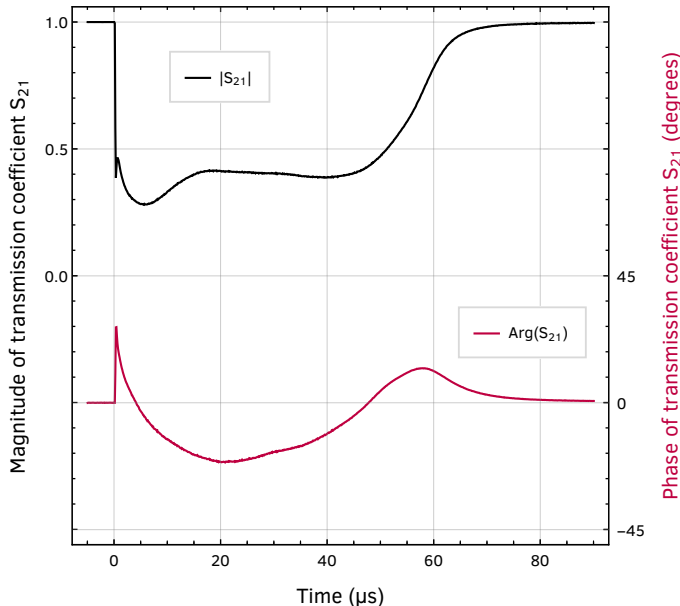


Figure 4.5: High temporal resolution complex transmission coefficient S_{21} obtained through microwave interferometric measurements on a transient toroidal helium plasma, generated by a laser-induced breakdown plasma created in quiescent atmospheric pressure helium gas at room temperature. The complex transmission coefficient has been derived from the recorded microwave detector signals presented in figure 4.4.

resolution, a first estimate of the electron number density and the electron collision rate as a function of time.

Full-wave finite-element complex transmission calculations

For a voluminous plasma the relation between the complex transmission coefficient S_{21} and the complex wave number k , and similar, to the complex permittivity ϵ , and hence to the electron number density and the electron collision rate, is straightforward, and our treatise on the propagation of electromagnetic waves in plasma presented in section 4.2 implies

$$S_{21} = e^{-k''d} e^{i(k_0 - k')d}$$

where k' and k'' are respectively the real and imaginary part of the complex wave number, d is the distance the microwave radiation propagates through the voluminous plasma, and k_0 is the wave number of the microwave radiation in free space.

However, as explained in the introduction, the dimensions of our toroidal plasma are of the same order of magnitude as the wavelength of the microwave radiation used to probe the plasma. Therefore, the limit for a voluminous plasma does not hold. Furthermore, because the separation of the pyramidal horn antennas is likewise small compared to the aperture of these antennas, multiple reflections between the horn antennas become important. Our only viable resort to obtain the plasma parameters from the presented complex transmission measurements are full-wave finite-element calculations of our microwave interferometric set-up, including a torus of uniform complex permittivity that is used to mimic our toroidal plasma.

In figure 4.6 we present the geometry used for the finite-element calculations, which shows the pyramidal horn antennas and the torus mimicking our toroidal plasma. A fully absorbing cylindrical surface around the horn antennas and the torus defines the region of free space.

Because the finite-element calculations already are computationally intensive, we have limited the calculation of the complex transmission coefficient to tori of two sizes that are representative for the evolution of our toroidal plasma. These sizes have been obtained from the optical measurements of our toroidal plasma presented in figure 2.8, at 30 μs and 50 μs . These moments respectively lie midway of the expanding phase, and towards the end of the evolution of the toroidal plasma. For each of these different sized tori, full-wave finite-element calculations have been performed for a range of values for the complex permittivity,

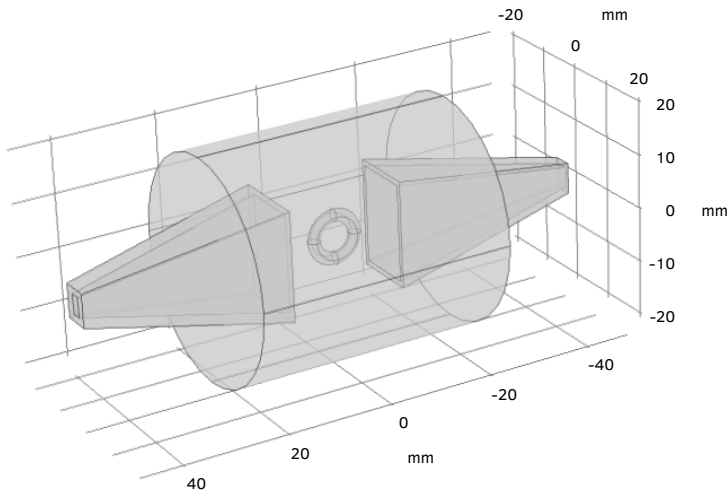


Figure 4.6: Geometry used for the full-wave finite-element calculations showing the pyramidal horn antennas and the torus mimicking our toroidal plasma. A fully absorbing cylindrical surface around the horn antennas and the torus defines the region of free space.

or equivalently, for a range of electron number densities and electron collision rates. These values have been guided by known estimates for atmospheric pressure plasmas generated in the laboratory.³⁶

The optical size of the toroidal plasma is expected to be similar to the electrical size determined by the free electrons in the toroidal plasma. However, as electrons are assumed to be responsible for the plasma emission, through collisional excitation of neutral atomic helium, low energy electrons, with insufficient energy to cause excitation of the helium atoms, can have a wider extent than optically observed.

Figure 4.7 presents the electric field strength of two representative finite-element calculations for a normalised electron collision rate ν/ω of 0.8 and a normalised electron number density n_0/n_c of 0.1 and 1.0. Here ν is the electron collision rate, ω is the frequency of the microwave radiation used to probe the toroidal plasma, n_0 is the electron number density, and n_c is the critical electron number density as defined in section 4.2. This figure clearly illustrates the complexity originating from the fact that the wavelength of the microwave radiation used is of the same order of magnitude as the dimensions of the toroidal plasma. It is evident that the behaviour of an electromagnetic wave propagating through such a plasma does not begin to compare with the propagation through a voluminous plasma.

In the presented full-wave finite-element calculations the complex permittivity has been assumed uniform throughout the torus. Ideally,

³⁶ Kabouzi et al. 2002;
F. F. Chen 1974;
Richardson 2019.

the poloidal radiant intensity profile, obtained through the three-dimensional tomographic reconstruction presented in section 2.5, is used as a measure for the dimensions and the electron number density of the toroidal plasma. However, the finite-element calculations already are computationally intensive, and with the course approximations applied we still are able to provide a first estimate for the plasma parameters of our toroidal plasma.

The full-wave finite-element calculations performed in the above manner relate the complex transmission coefficient S_{21} to pairs of the electron number density n_0 and the electron collision rate ν . For

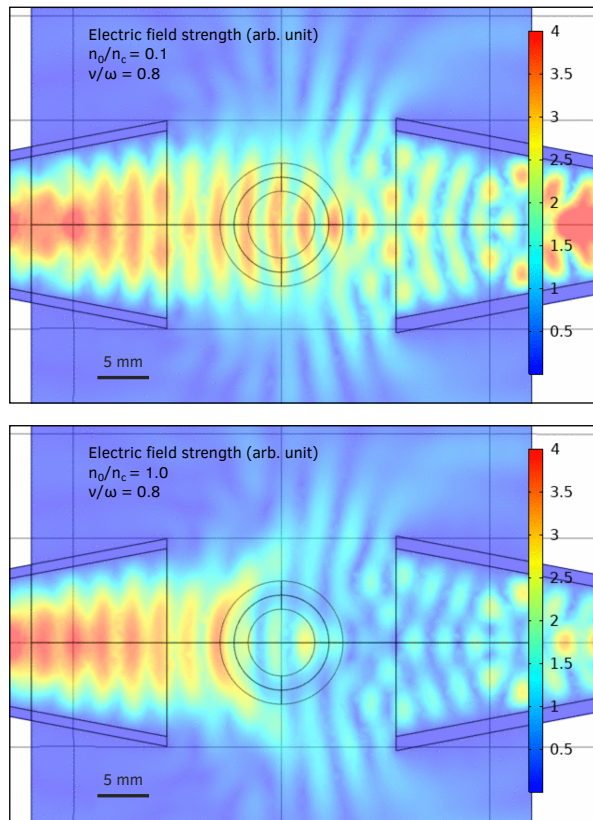


Figure 4.7: Electric field strength of two representative finite-element calculations for a normalised electron collision rate ν/ω of 0.8 and a normalised electron number density n_0/n_c of 0.1 and 1.0, showing the complexity originating from the fact that the wavelength of the microwave radiation used is of the same order of magnitude as the dimensions of the toroidal plasma. Here ν is the electron collision rate, ω is the frequency of the microwave radiation used to probe the toroidal plasma, n_0 is the electron number density, and n_c is the critical electron number density as defined in section 4.2. The torus used to mimic the toroidal plasma in these calculations is represented by the two concentric circles in the centre. The electric field strength is shown for the cross-sectional symmetry plane parallel to the long side of the aperture of the pyramidal horn antennas shown in figure 4.6. As a consequence of the employed TE₁₀ mode, the electric field is directed orthogonal to this symmetry plane.

reasons of readability, the presentation of this relation is postponed to the next subsection, where it will be presented together with high temporal resolution, complex transmission measurements, obtained through the microwave interferometric measurements on our transient toroidal helium plasma.

Electron number density and electron collision rate determination

In the previous sections we have presented high temporal resolution, complex transmission measurements on our transient toroidal helium plasma. We also presented full-wave finite-element calculations of the complex transmission coefficient of our entire experimental set-up, where our toroidal plasma has been mimicked by a uniform torus. In figure 4.8 we present, in the complex plane, the complex transmission coefficient obtained through both these methods. The continuous black curve represents the evolution of the complex transmission coefficient of our toroidal plasma for its entire evolution, while the coloured lines represent the finite-element calculations for different sized tori, and for different electron number densities and electron collision rates.

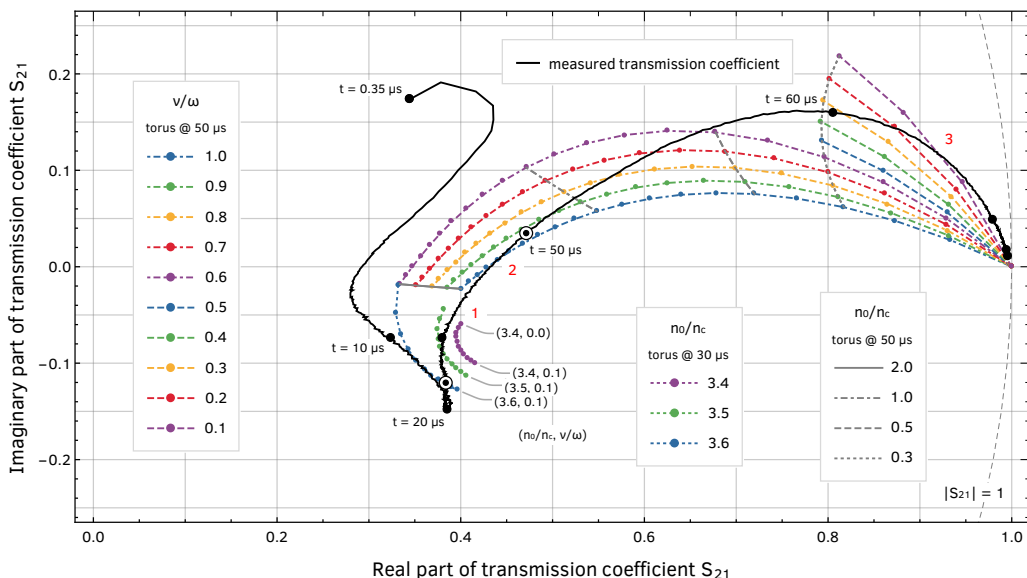


Figure 4.8: Complex transmission coefficient S_{21} obtained for our transient toroidal helium plasma through high temporal resolution complex transmission measurements using a microwave interferometer (continuous black curve with time markers) together with full-wave finite-element calculations of our entire experimental set-up in which our toroidal plasma has been mimicked by a torus of fixed size, and with uniform electron number density and electron collision rate (coloured lines). The bullseye time markers along the black curve, at $30 \mu\text{s}$ and $50 \mu\text{s}$, indicate when the two representative sizes for the evolution of the toroidal plasma have been obtained.

A first estimate of the electron number density and the electron collision rate can now be obtained in high temporal resolution, by regarding the finite-element calculations as a map from the complex plane to the two-dimensional space spanned by the electron number density and the electron collision rate, and subsequently applying this map to the complex transmission coefficient obtained by our microwave interferometric measurements. Because the map resulting from the finite-element calculations is discrete, a linear interpolation has been used to create a continuous map.

In figure 4.9 we present the normalised electron number density and the normalised electron collision rate of our transient toroidal helium plasma, as modelled by a uniform torus and obtained in the manner set out above. It is clear that in the first half of the evolution, the electron number density is well above cut-off. Towards the end of the evolution, the electron number density monotonically decreases to zero, which is, as explained earlier, expected for an extinguishing plasma. In this part of the evolution, the electron number density and the electron collision rate are of the order of 10^{19} m^{-3} respectively 10^{10} s^{-1} , which conforms to

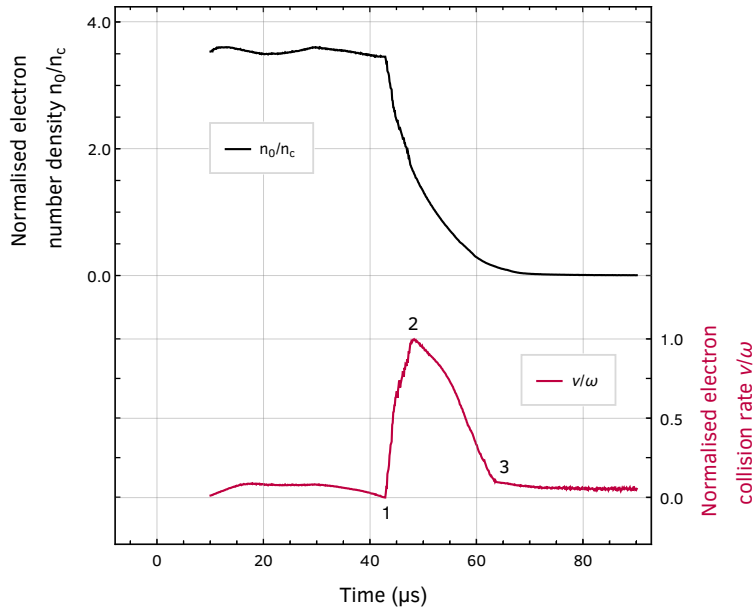


Figure 4.9: High temporal resolution, normalised electron number density and normalised electron collision rate of our transient toroidal helium plasma, as modelled by a uniform torus. Based on complex transmission measurements and full-wave finite-element calculations of our entire experimental set-up, where our toroidal plasma has been mimicked by a torus, these results have been obtained from figure 4.8 by regarding the finite-element calculations as a map for the complex transmission measurements of the toroidal plasma. For our experiment utilising 57 GHz microwave radiation we have $\omega = 3.58 \cdot 10^{11} \text{ s}^{-1}$ and $n_c = 4.03 \cdot 10^{19} \text{ m}^{-3}$.

known values for atmospheric pressure laboratory plasmas.³⁷

In the presented evolution of the plasma parameters, discontinuities in the first derivative are clearly visible. These discontinuities are a direct consequence of our choice of splitting the evolution of our toroidal plasma into two parts, and assuming a uniform torus of fixed size for each part. Evidently this is a very coarse approximation, as the size, and even more importantly, the spatial distribution of the emission from the toroidal plasma, has been seen to evolve considerably. This is supported by the observation that the size of the torus used to mimic our toroidal plasma in the finite-element calculations can have a significant effect on the obtained plasma parameters. Specifically, attributing vastly different plasma parameters (n_0/n_c , ν/ω) to differently sized tori can result in an almost identical complex transmission coefficient, as can be seen explicitly in figure 4.8 where the calculations for $n_0/n_c = 3.6$ and $\nu/\omega = 0.6$ intersect.

In order to better understand the cause of the discontinuities visible in the electron collision rate presented in figure 4.9, we will briefly discuss these discontinuities in what follows.

(1) This discontinuity arises as a result of the extreme sensitivity of the finite-element calculations on the size of the torus used to model our toroidal plasma. This sensitivity has already been mentioned in the preceding paragraph. In figure 4.8 this discontinuity corresponds precisely to the moment (red label 1) when the measured transmission coefficient leaves the domain in the complex plane spanned by the finite-element calculations for constant electron density (purple, green and blue dotted lines).

(2) When the measured transmission coefficient crosses the finite-element calculations for a constant normalised electron collision rate of 1.0 (blue dot-dashed line and red label 2 in figure 4.8), a discontinuity arises because, before this crossing, the electron collision rate increases after leaving the first discontinuity, and after this crossing, it decreases again, as the measured transmission coefficient continues to move through the domain spanned by the finite-element calculations for a constant electron collision rate (coloured dot-dashed lines). Note that to create a continuous map a linear interpolation has been used.

(3) This discontinuity arises because the measured transmission coefficient enters a region in the complex plane that is not bounded by a series of finite-element calculations, which renders the interpolation unreliable. This could be improved by performing additional finite-element calculations for lower values of the electron collision rate.

In conclusion of this section, we will assess the electron collision

³⁷ Kabouzi et al. 2002;
F. F. Chen 1974;
Richardson 2019.

rate presented in figure 4.9. We already noted that in the first half of the evolution of the toroidal plasma, the electron number density is well above cut-off. During this time, microwave radiation cannot significantly penetrate the toroidal plasma, and the resulting electron collision rate should therefore be interpreted with caution.

In the second half of the evolution, the electron collision rate decreases monotonically to a limit value. Because plasma emission is still observed during this time, it is not unreasonable to assume that the electrons still have an elevated temperature while cooling down. But, at the same time, the electron collision rate is seen to decrease a factor of ten. For weakly ionised plasmas the electron collision rate is given by³⁸

³⁸ Richardson 2019, p. 38.

$$\nu = n_n \sigma \sqrt{\frac{kT_e}{m_e}}$$

where n_n is the neutral density, σ is the scattering cross section, k is the Boltzmann constant, T_e is the electron temperature, and m_e is the electron mass. Therefore, we ought to conclude that the electron temperature should have been at least 30.000 K, assuming that the neutral density has already been restored. The latter is a reasonable assumption if we consider the density measurements presented in section 2.5. However, such an electron temperature is unreasonable at this time in the afterglow.³⁹

³⁹ Nedanovska et al. 2015.

If we reconsider the foregoing and bring to mind the optical images of the toroidal plasma presented in section 2.5, we may reasonably conclude that, because the toroidal plasma does not resemble a torus in this part of its evolution, the finite-element calculations cannot be considered representative during this time. As has been mentioned before in this section, considerable improvements can be expected when a tomographically reconstructed, poloidal radiant intensity profile, based on optical recordings, is used as a measure for the dimensions and the electron number density of the toroidal plasma.

4.4 Conclusion

In this chapter we have presented the electron number density and the electron collision rate for the entire evolution of a transient toroidal helium plasma. These plasmas have been generated by a single laser-induced breakdown plasma, in quiescent atmospheric pressure helium gas at room temperature, using a laser pulse energy of 250 mJ.

By combining interferometric measurements using 57 GHz microwave radiation with detailed full-wave finite-element calculations of our

interferometric set-up, we were able to obtain the plasma parameters with high temporal resolution.

In the second half of the evolution, where the toroidal plasma can be regarded as an afterglow, the electron number density and the electron collision rate are of the order of 10^{19} m^{-3} respectively 10^{10} s^{-1} , which conforms to known values for atmospheric pressure laboratory plasmas.

We discussed in detail the microwave interferometric set-up used to measure the complex transmission coefficient, and presented a method whereby the finite-element calculations can be used as a map between the measured transmission coefficient and the sought after plasma parameters. With this approach we overcame the biggest challenges in studying transient toroidal helium plasmas, namely their limited lifetime and their limited size.

Because the finite-element calculations already are computationally intensive, we have limited the calculation of the complex transmission coefficient to uniform tori of two sizes that are representative for the evolution of our toroidal plasma. For each of these different sized tori, full-wave finite-element calculations have been performed for a range of values for the complex permittivity.

In the presented evolution of the plasma parameters, discontinuities in the first derivative are clearly visible. These discontinuities are a direct consequence of our choice of splitting the evolution of our toroidal plasma into two parts, and assuming a uniform torus of fixed size for each part. Evidently this is a very coarse approximation, as the size and the spatial distribution of the emission from the toroidal plasma have been seen to evolve considerably.

We briefly discussed an improvement of this method by which a tomographically reconstructed, poloidal radiant intensity profile, based on optical recordings, can be used as a measure for the dimensions and the electron number density of the toroidal plasma, to better model the toroidal plasma in the finite-element calculations.

Finally, we note that the size of the torus used to mimic our toroidal plasma in the finite-element calculations can have a significant effect on the obtained plasma parameters. Specifically, attributing vastly different plasma parameters to differently sized tori can result in an almost identical complex transmission coefficient. This obviously complicates the method whereby the finite-element calculations are used as a map between the measured transmission coefficient and the sought after plasma parameters. This suggest that considerable improvements can be expected when utilising the aforementioned tomographically reconstructed, poloidal radiant intensity profile.

5

Pulsed magnetron heating experiments on transient toroidal helium plasmas

We experimentally studied the evolution of a transient toroidal helium plasma, subjected to a high power 2.46 GHz microwave pulse. We discuss in detail the design of the pulsed magnetron source and determine its electrical characteristics during these experiments. To apply the 1.75 kW high power microwave pulse to the toroidal plasma, we designed a 2.465 GHz iris coupled rectangular microwave cavity. We discuss the effect of the microwave pulse on the toroidal plasma, and elaborate on the dark space that is observable between the microwave generated plasma and the toroidal plasma. We determine that the 100 μ s long microwave pulse attains a sub-microsecond rise time and discuss the frequency droop during this pulse. Finally, we present a poloidal excitation temperature profile of the toroidal plasma by applying a standard Boltzmann analysis to two tomographic reconstructions of the toroidal plasma, obtained from images recorded at two different wavelengths.

5.1 Introduction

The endeavours presented in this work all have been carried out while keeping in mind the desire to realise self-organising knotted magnetic structures in plasma. So far, our main concern has been the study of transient toroidal helium plasmas, however, their limited lifetime, which is considerably less than 100 μ s, unfortunately hinders the realisation of these structures.

In this chapter we present our first experiments aimed at extending the lifetime of these toroidal plasmas, through heating of these structures using microwave radiation, and discuss the observations and preliminary steps made in this direction. The main difficulty with this venture is once more, the limited lifetime of these plasmas, which

necessitates a pulsed nature of these experiments if a detailed study of its effects is desired.

In what follows we present the design of the pulsed magnetron source used in our experiments on transient toroidal helium plasmas, and characterise its behaviour during these experiments. We discuss the integration of a 2.465 GHz microwave cavity into our existing set-up used to study the toroidal plasmas, and present optical recordings of the evolution of a toroidal plasma subjected to a high power 2.46 GHz microwave pulse. We discuss the observed effects, and elaborate on the additional plasma structure generated by the microwave field near the toroidal plasma.

Finally, we will present a poloidal excitation temperature profile of the toroidal plasma, including the surrounding microwave generated plasma structure, obtained from recordings captured 50 μs after the creation of the laser-induced breakdown plasma responsible for the generation of the toroidal plasma.

5.2 *Design of the pulsed magnetron source*

The microwave generators that are generally used, for example, for atomic emission spectroscopy and plasma ion sources, are continuous microwave generators. However, because we are investigating transient toroidal helium plasmas with a lifetime which is considerably less than 100 μs , we need a pulsed microwave source that matches this time-scale, in order to investigate the effects of heating at different moments during the evolution of our toroidal plasma. Additionally, due to the limited time available to add energy to the toroidal plasma, a high power source is mandatory. For this reason we have opted for a magnetron as the source of microwave radiation.

Trivially, the microwave pulses generated must have at least a short rise time, to be able to create short pulses. The physical processes at work in a magnetron unfortunately conflict with this requirement, because for a magnetron it takes time to start oscillating as a result of the stochastic nature of this process. The rising edge of the high-voltage pulse must therefore spend a finite time in the so-called Hartree region to ensure that the oscillations start properly in each pulse. Furthermore, because the magnetron typically operates at about 4 kV, driving the capacitance of the wiring, the transformers and the magnetron itself, poses limitations on the rise time of the pulse.

Our adopted solution is to continuously operate the magnetron on an extremely low power, such that the magnetron has the ability

to start oscillating properly. Subsequently, while the magnetron is oscillating at low power, we generate a high power pulse by very rapidly increasing the current through the magnetron. This significant increase in current is accompanied by just a small increase in the magnetron voltage due to the low dynamical resistance of the magnetron above the Hartree voltage. In radar applications, where high spatial resolution and minimum range coverage to within a few metres are required, for example, for active seekers for missiles, a magnetron is operated using a pedestal modulation technique,¹ improving upon our adopted scheme.

¹ Nyswander et al. 1976.

The high-voltage magnetron pulser

In figure 5.1 we present a simplified schematic of the high-speed high-voltage pulser used to drive the magnetron in the experiments presented in this chapter. Auxiliary components such as those used for voltage and current measurements have been omitted for reasons of readability. The high-voltage transformers and passive components, as well as the magnetron itself, are components that can be readily found in domestic microwave ovens. In this experiment a Samsung OM75P magnetron has been used. The filament transformer is a tailor-made low capacitance transformer. Standard variable auto-transformers have been used to vary the primary voltage of the high-voltage and filament transformers.

The pulser is designed around two Greinacher voltage doublers which double the secondary voltage of the two mains² connected high-voltage transformers. Depending on the settings of the auto-transformers, voltages of up to 5.5 kV can be generated. To be able to generate microwave pulses with sub-microsecond rise times, the

² The mains is also referred to as utility power.

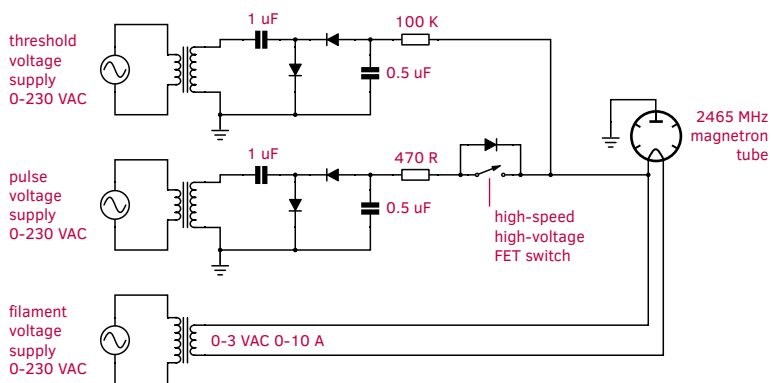


Figure 5.1: Simplified schematic of the high-speed high-voltage pulser used to drive the magnetron in the presented heating experiments on transient toroidal helium plasmas. Auxiliary components such as those used for voltage and current measurements have been omitted for reasons of readability.

magnetron voltage is biased using a 100 K resistor, which brings the magnetron voltage to a threshold voltage of approximately 4 kV.

A 470 Ω series resistor is used to create a rudimentary current source for driving the low dynamical resistance of the magnetron, and is switched using a high-speed high-voltage FET switch (Behlke HTS 81-12-B) whose trigger signal is generated by the same trigger system used for the generation and analysis of the toroidal plasmas. This system is build around a digital delay generator (Stanford Research Systems DG645) and an in-house designed FPGA (field-programmable gate array) based reconfigurable pulse generator. The particulars of the trigger system are explained in more detail in section 2.2.

Integration of a microwave cavity into the plasma reactor

The high power microwave pulses, generated by the high-voltage magnetron pulser, have to be applied to our toroidal plasma. In plasma research different approaches exist for the coupling of microwave radiation to a plasma.

³Spanel et al. 2004.

We initially started with a directly coupled monolithic rectangular microwave cavity,³ where the magnetron antenna is mounted directly into the resonant cavity. Although the approach is very appealing, primarily because of its simplicity, we ran into issues where the magnetron did not start to oscillate properly, or oscillated at an incorrect frequency, or with low power.

We attributed this to the fact that the magnetron starts to oscillate at a frequency different from the resonance frequency of the cavity. As a result, the power reflected off the cavity is injected into the magnetron, thereby influencing its start-up behaviour.

⁴Broekaert et al. 2004;
Matusiewicz 1992;
Hammer 2008.

Different improved approaches exist, where the resonant cavity is separated from the magnetron.⁴ These, we found, are bothered by similar start-up difficulties. In the end we opted for a more conventional set-up, whereby the magnetron is completely isolated from the rest of the microwave set-up using a microwave isolator, thereby preventing the injection of reflected power into the magnetron.

⁵For a more lively impression of the experimental set-up we refer to photo 3 on page 105.

In figure 5.2 we present a simplified schematic⁵ of the combined pulsed magnetron set-up and the pulsed high power optical set-up, used for the experiments presented in this chapter.

The pulsed magnetron set-up consists of a 2.465 GHz iris coupled TE₁₀₁ mode $\lambda_g/2$ rectangular microwave cavity, a tailor-made three stub tuner and a coaxial to wave-guide transition. The rectangular wave-guide stub tuner and the microwave cavity are mounted directly into

the plasma reactor. This is not the most ideal approach, because it necessitates the use of a vacuum sealed coaxial to wave-guide transition and a vacuum sealed wave-guide entrance into the plasma reactor. But just as with our 57 GHz diagnostic experiments presented in chapter 4, it proved to be the most practical means to integrate these experiments into our existing set-up.

The microwave cavity is positioned in such a way that the anti-node of the electric field of the TE₁₀₁ mode coincides with the focal point of the lens generating the laser-induced breakdown plasmas from which the toroidal plasmas emerge.

The microwave cavity is further equipped with beyond cut-off view ports (not shown) such that the laser pulses can safely enter and exit the cavity. In a similar fashion, side view images of the toroidal plasma can

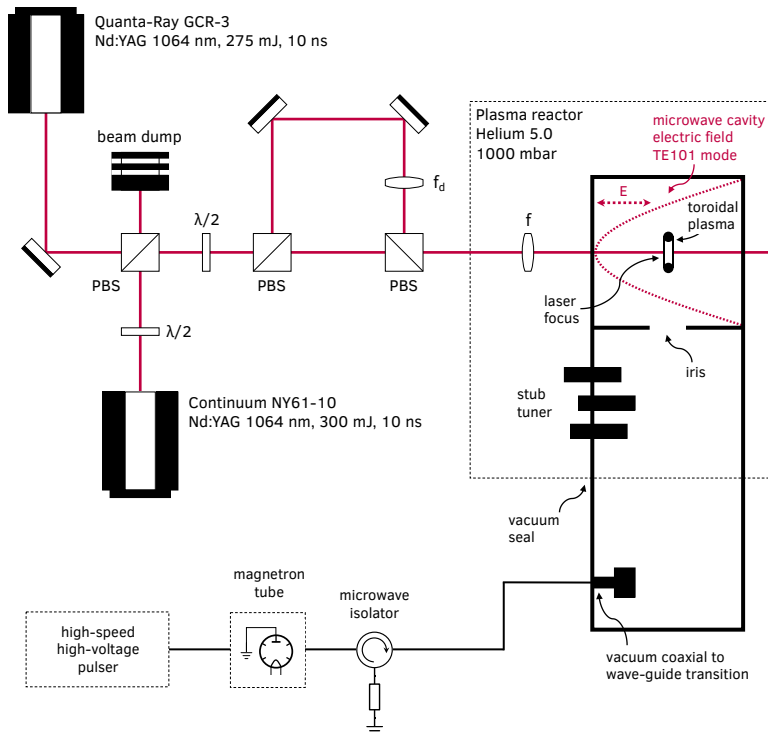


Figure 5.2: Simplified schematic of the combined pulsed magnetron set-up and the pulsed high power optical set-up used for the presented experiments. The pulsed magnetron set-up consists of a 2.465 GHz iris coupled TE₁₀₁ mode $\lambda_g/2$ rectangular microwave cavity, a tailor-made three stub tuner and a coaxial to wave-guide transition. The rectangular wave-guide stub tuner and the microwave cavity are mounted directly into the plasma reactor. The microwave cavity is positioned in such a way that the anti-node of the electric field of the TE₁₀₁ mode coincides with the focal point of the lens generating the laser-induced breakdown plasmas. The high power optical set-up is identical to the set-up used to investigate the transient toroidal helium plasmas as presented in chapter 2. For a more lively impression of the experimental set-up we refer to photo 3 on page 105.

be obtained, just like in the experiments presented in chapter 2.

The guide wavelength for our aluminium rectangular wave-guide, having internal dimensions of 90 x 40 mm, is approximately 165 mm. The $\lambda_g/2$ microwave cavity is coupled to the feeding wave-guide using an iris with an aperture diameter of 21 mm. The described vacuum seals in the plasma reactor wall, and in the coaxial to wave-guide transition, ensure that the experiments can be performed in a pure helium atmosphere.

High power 2.46 GHz microwave pulses of up to 1.75 kW have been generated using the high-voltage magnetron pulser described in the previous subsection. The microwave isolator protects the operation of the magnetron against power reflected off a possibly detuned microwave cavity, as a result of the presence of plasma in the cavity. The high power optical set-up is identical to the set-up used to investigate the transient toroidal helium plasmas, and for a detailed description thereof we refer to section 2.2.

5.3 *Pulsed magnetron heating experiments on transient toroidal helium plasmas*

Using the pulsed magnetron source presented in the previous section, we performed experiments on the transient toroidal helium plasmas studied extensively in chapter 2. In this section, we present an analysis of the optical recordings captured during these experiments, and characterise the behaviour of the magnetron pulser.

Optical analysis of the pulsed magnetron heating experiments

The transient toroidal helium plasmas studied in this section have been generated by a single laser-induced breakdown plasma, created in quiescent atmospheric pressure helium gas at room temperature. The laser pulse energy used to create the breakdown plasmas was 250 mJ.

For our optical analysis we recorded side view images through a view port in the microwave cavity as described in the previous section. All images have been captured using a fixed gate width of 250 ns and a fixed gain of 255. Because of the small fluctuations visible in the recordings, all images have been averaged over 50 repetitions, to increase the signal to noise ratio. Furthermore, all images have been corrected for flat field and background emission, and to aid in a quantitative analysis, all images have been captured through a 10 nm bandpass filter with a centre wavelength of 590 nm. For further experimental details, and a

motivation of the above, we refer to sections 2.2–2.3.

In figure 5.3 we present selected side view images of the evolution of a transient toroidal helium plasma, starting from 20 μs after the creation of a laser-induced breakdown plasma. The top row shows the familiar evolution in the absence of microwave radiation. The bottom row shows the same time span, whereby during the whole presented evolution the magnetron has been operational and microwave radiation was present in the cavity in which the toroidal plasma was generated. In figure 5.4 the spectral radiant intensity of the observed evolution is presented.

The microwave pulse in this experiment extends from 20 μs to 120 μs . The beginning of the microwave pulse does not leave any observable effect, neither in the optical images nor in the spectral radiant intensity. However, the end of the pulse is clearly visible in the sharp decline of the spectral radiant intensity at 120 μs .

In the optical recordings of figure 5.3, the toroidal plasma seems to be unaffected by the microwave field. However, from 52 μs onward, we observe that the microwave field generates additional plasma, and surprisingly, this microwave plasma is generated at a distance from the region where the toroidal plasma has been observed, even after the toroidal plasma itself already is extinguished. After 76 μs we see that this region is also filled with plasma generated by the microwave field.

The observed distance between the microwave generated plasma and the toroidal plasma is reminiscent of the dark spaces found in a glow discharge.⁶ In the Aston dark space of a glow discharge, the electrons

⁶ Fridman 2008, p. 175.

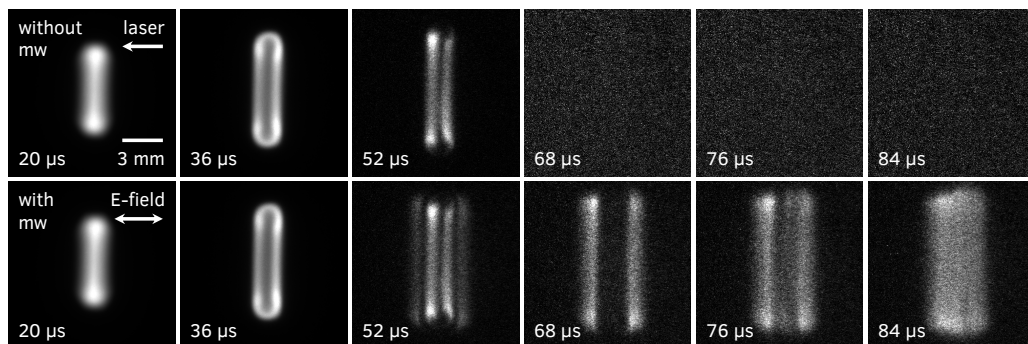


Figure 5.3: Selected side view images of the evolution of a transient toroidal helium plasma, starting from 20 μs after the creation of a laser-induced breakdown plasma. The top row shows the familiar evolution in the absence of microwave radiation, whereas the bottom row shows the same time span, whereby during the whole presented evolution the magnetron has been operational and microwave radiation was present in the cavity. All images have been averaged over 50 exposures and captured through a 10 nm bandpass filter with a centre wavelength of 590 nm. All images have been individually normalised to their maximum intensity to respect the large dynamic range in intensity of the entire evolution. Laser pulse energy: 250 mJ, focal length focussing lens: 50 mm, helium gas pressure: 1003 mbar, ICCD camera gate width: 250 ns, ICCD camera gain: 255.

ejected from the cathode, through secondary electron emission, do not have sufficient energy for the excitation of atoms, and therefore a dark space forms. The electrons are subsequently accelerated in the electric field of the glow discharge, and when they have gained sufficient energy to excite atoms, the dark space ends.

The dark space observed around the toroidal plasma can be explained when we assume that the electrons needed for the generation of the microwave plasma surrounding the toroidal plasma, are ejected from the toroidal plasma itself, but just like in the Aston dark space of a glow discharge, do not yet have sufficient energy for the excitation of helium atoms. Because of the quasi neutrality of the toroidal plasma, not all of its electrons can participate in this process, only the high energy electrons that manage to overcome the electrical potential of the ion charge density, can escape from the surface of the toroidal plasma. These electrons are then accelerated in the electric field of the microwave pulse, until they have gained sufficient energy for the excitation of the helium atoms surrounding the toroidal plasma.

A similar dark space has been observed in experiments where we subjected the toroidal plasma to a high-voltage pulse. In figure 5.5 we present the evolution of such a measurement, where the toroidal

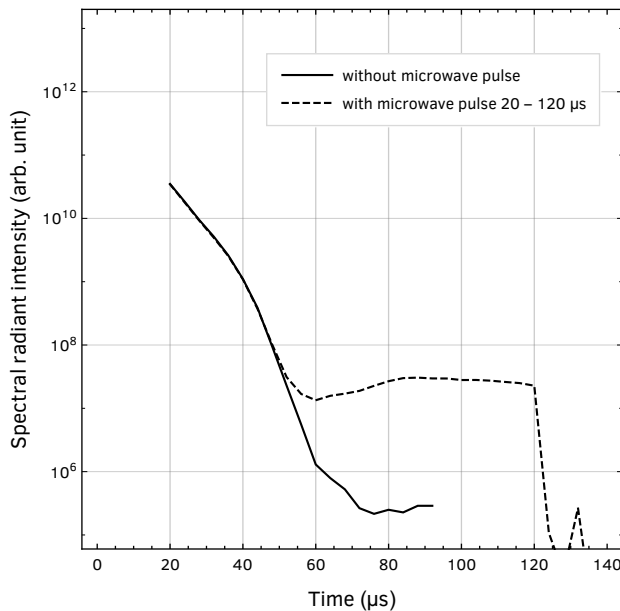


Figure 5.4: Spectral radiant intensity of the evolution presented in figure 5.3. Measurements have been recorded at a 4 μ s interval but for clarity only selected images have been presented in figure 5.3.

plasma has been subjected to a +4 kV high-voltage pulse, showing with nanosecond temporal resolution, the emission of an ionisation wave propagating away from the toroidal plasma. Prior, an ionisation channel can be seen to form, from the high-voltage tip to the toroidal plasma. Between the toroidal plasma and the ionisation wave, and similarly between the ionisation channel and the toroidal plasma, a dark space can clearly be observed.

These dark spaces can be explained on similar grounds as the dark space around the toroidal plasma in the presence of a microwave field. Because the high-voltage tip is positively charged, the toroidal plasma acts as a cathode, resulting in an Aston dark space between the ionisation channel and the toroidal plasma. Similarly, the dark space between the ionisation wave and the toroidal plasma can be regarded as the anode dark space of a glow discharge, where electrons are removed from the vicinity of the toroidal plasma as a result of its positive potential with respect to the plasma reactor.

The fact that the toroidal plasma seems to be unaffected by the microwave field could be anticipated for if we take into consideration the evolution of the electron number density obtained in chapter 4. The critical electron number density for 2.46 GHz radiation is more than a factor of 500 lower than for the 57 GHz radiation used in those experiments. An examination of the results presented in figure 4.9 reveals that the electron number density attains the same order of magnitude as the critical electron number density for 2.46 GHz radiation at around 75 μs . Before that time, the 2.46 GHz microwave field cannot be expected to penetrate the toroidal plasma, as is in clear agreement with the observations presented in figure 5.3.

We have to note that the results presented in chapter 4 have been obtained after a number of coarse approximations. Nevertheless, the consensus of the observations presented here and the electron number density obtained in chapter 4 seems trustworthy.

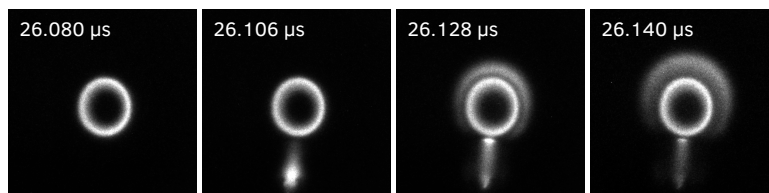


Figure 5.5: Evolution of a representative measurement where the toroidal plasma has been subjected to a +4 kV high-voltage pulse, showing with nanosecond temporal resolution, the emission of an ionisation wave propagating away from the toroidal plasma. Prior, an ionisation channel can be seen to form, from the high-voltage tip (at the bottom of the image, but not visible) to the toroidal plasma.

Characterisation of the pulsed magnetron source

In the remainder of this section we present the electrical characteristics of the pulsed magnetron source, determined during the experiments presented in the previous subsection.

As explained in section 5.2 on the design of the pulsed magnetron source, before the actual generation of high power microwave pulses, the magnetron is brought into the Hartree region, to ensure that the magnetron starts to oscillate properly, but does so with minimal power. In the described experiments this has been realised by increasing the pulser threshold voltage to 4.1 kV. At this voltage the current through the magnetron was measured to be 8.1 mA.

Obviously, before a magnetron can oscillate, as it is just a kind of vacuum tube, the magnetron filament has to be heated in order to ensure that thermal electron emission can occur. In our experiments we used a filament voltage of 2.6 VAC resulting in a filament current of 7.1 A. We found that by slightly adjusting the filament current during an experiment, the oscillation frequency of the magnetron could be tuned to an optimal frequency for our microwave cavity.

The pulse voltage used to generate the high power pulses was set to

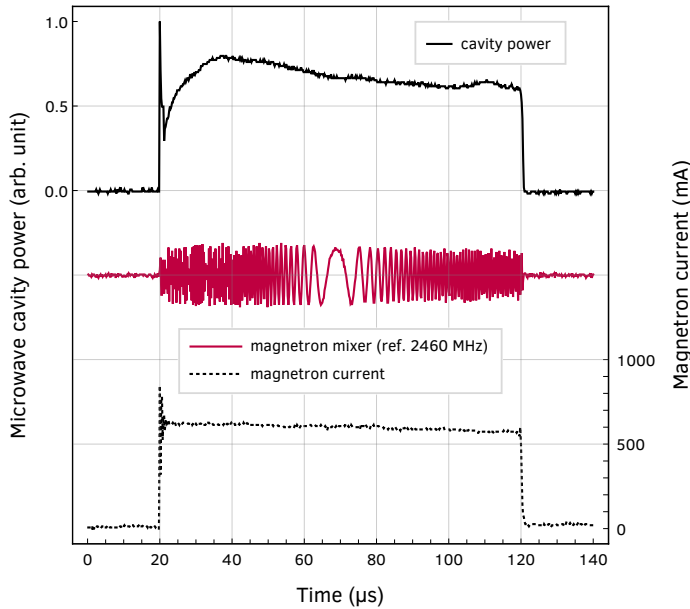


Figure 5.6: Evolution of the microwave cavity power and the magnetron current for the experiment whose optical evolution is presented in figure 5.3, together with a magnetron mixer signal, obtained by mixing stray radiation emitted by the magnetron and received by a simple loop antenna, with a fixed reference frequency of 2460 MHz.

5.2 kV. Note that this voltage is measured before the 470 Ω series resistor, so that the actual magnetron voltage is considerably lower due to its low dynamical resistance above the Hartree voltage.

In figure 5.6 we present, for the experiment described in the previous subsection, the evolution of the microwave cavity power and the magnetron current, together with a magnetron mixer signal, obtained by mixing stray radiation emitted by the magnetron and received by a simple loop antenna, with a fixed reference frequency of 2460 MHz.

From the magnetron mixer signal, we derived the evolution of the magnetron frequency during the experiment, by analysing its zero-crossings. The evolution thus obtained is presented in figure 5.7.

The slight decline in the magnetron frequency can be understood from the observed decline in current through the magnetron. In order to mitigate this change in frequency, the generation of the toroidal plasmas has been synchronised with the mains, such that both capacitors of the Greinacher voltage doubler will be used as an energy source for the magnetron pulse, thereby limiting the current droop through the magnetron. Operating the pulsed magnetron source synchronised with the mains thereby reduces the experimental fluctuations that would be caused by the generation of the magnetron pulse at arbitrary times

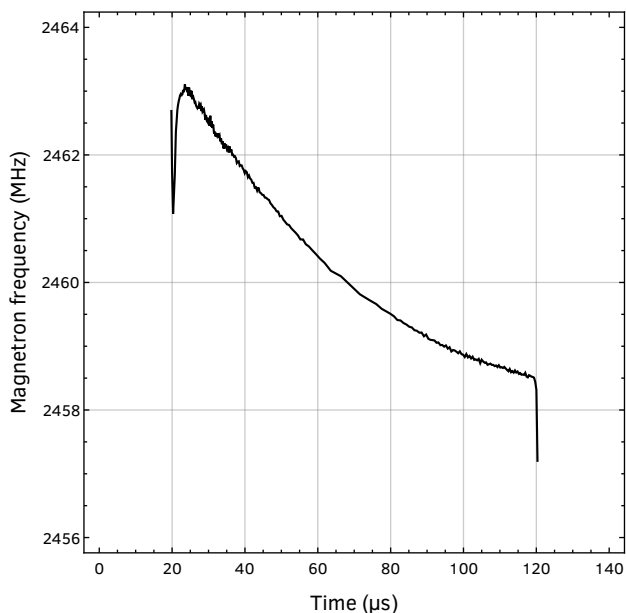


Figure 5.7: Evolution of the magnetron frequency during the generated high power microwave pulse, obtained by analysing the zero-crossings of the magnetron mixer signal presented in figure 5.6.

during a mains voltage cycle. A possible improvement of the stability of the magnetron frequency can be obtained by injection-locking the magnetron to an external low-power frequency reference.⁷

⁷ Tahir et al. 2006.

From the recordings presented in figure 5.6 we can see that the average current through the magnetron is approximately 600 mA. Combined with a magnetron voltage of about 4.1 kV we find that the electrical power delivered to the magnetron is approximately 2.5 kW. The efficiency of the magnetron has been measured⁸ to be approximately 70% which implies a microwave pulse power of 1.75 kW. Unfortunately, we did not have the ability yet to measure the absolute power inside the microwave cavity, so we could not quantitatively obtain a value for the microwave cavity power.

⁸ The efficiency of the magnetron has been determined in an isolated set-up, disconnected from the microwave cavity, where the power of the pulse has been measured using a 50 dB attenuator.

The recorded evolution of both the magnetron current and the microwave cavity power, indicates that the rise and fall times of the microwave pulses are very fast, and that sub-microsecond rise times are attained.⁹ The cavity power shows complicated behaviour that needs further analysis, but it is tenable to conclude that the cavity power is affected by the varying magnetron frequency, through the frequency response of the cavity, as well as by the presence of plasma in the cavity.

⁹ During the determination of the magnetron efficiency mentioned above, we generated microwave pulses with a length of 10 μ s and observed rise and fall times of less than 500 ns.

The observed detuning of the cavity resonance frequency of about 5 MHz is caused by the presence of plasma in the cavity. Inserting a small amount of dielectric material into a resonant cavity is known to cause the resonance frequency to shift slightly.¹⁰ For our toroidal plasma this can be understood when considering the toroidal plasma to be a conductor situated in parallel to the cavity walls, perpendicular to the direction of the electric field, thereby acting as a capacitor which lowers the resonance frequency of the microwave cavity.

¹⁰ Waldron 1960.

5.4 *Poloidal excitation temperature profile of transient toroidal helium plasmas*

The observation that the microwave generated plasma surrounding the toroidal plasma, and the toroidal plasma itself, are essentially two distinct plasmas, raises the question of how these plasmas differ in their optical properties and how they are spatially distributed.

In a first attempt to answer these questions, we recorded images during the aforementioned experiments using two different 10 nm bandpass filters that enclose the atomic helium emission lines at 587.6 nm and 706.5 nm, motivated by the same reasoning set out in section 2.3. In addition to a filter with a centre wavelength of 590 nm

(Thorlabs FB590-10) used for most images presented in this work, additional images have been recorded through a filter with a centre wavelength of 710 nm (Thorlabs FB710-10).

To be able to spatially discern from where the emission of both plasmas originate, and even more importantly, because we set out to determine an estimate of the excitation temperature of both plasmas, it is instrumental to tomographically reconstruct the poloidal radiant intensity profile of both plasmas using the method described in section 2.5. Because the excitation temperature will be determined using a standard Boltzmann analysis,¹¹ which utilises relative intensities, or ratios, of the atomic helium emission lines, it is evident that a tomographic reconstruction is necessary.

In figure 5.8 we present side view images of the microwave generated plasma surrounding the toroidal plasma, and the toroidal plasma itself, recorded through two different bandpass filters as explained above, together with their poloidal radiant intensity profile obtained through a tomographic reconstruction. The poloidal radiant intensity profiles are presented in black and white, as well as in contrast enhanced false colour, to better visualise the core of the toroidal plasma.

The side view images have been captured 50 μ s after the creation of the laser-induced breakdown plasma responsible for the generation of the toroidal plasma. To further increase the signal to noise ratio, the gate width has been increased to 1 μ s and all recordings have been averaged

¹¹ Griem 1997, p. 279; Monfared et al. 2011; Gulec et al. 2015.

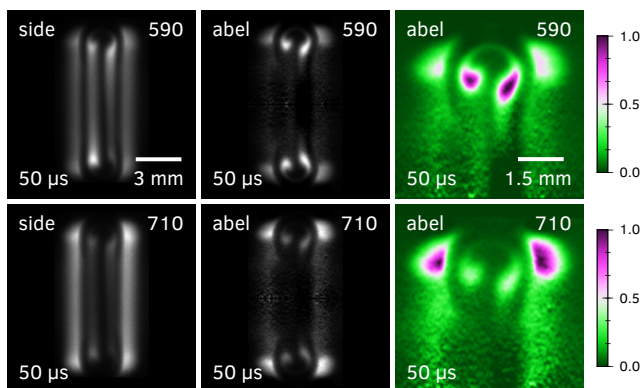


Figure 5.8: Side view images of the microwave generated plasma surrounding the toroidal plasma, and the toroidal plasma itself, recorded through two different 10 nm bandpass filters with a centre wavelength of 590 nm resp. 710 nm, together with their poloidal radiant intensity profile obtained through a tomographic reconstruction. The side view images (left) have been captured 50 μ s after the creation of the laser-induced breakdown plasma responsible for the generation of the toroidal plasma. The poloidal radiant intensity profiles are presented in black and white (centre) as well as in contrast enhanced false colour (right) to better visualise the core of the toroidal plasma. Note that the images have been individually normalised to their maximum intensity to respect their large dynamic range, and that the contrast enhanced false colours do not share the same absolute scale between the 590 nm and 710 nm recordings.

over 1000 repetitions. The experimental conditions are otherwise similar to those presented in section 5.3.

It is clear that the side view images exhibit a slight asymmetry between their top and bottom halves, which influences the tomographic reconstruction as explained in section 2.4. An assessment of the obtained poloidal radiant intensity profiles nevertheless indicates that this effect seems to be limited for these reconstructions.

From the presented images it is evident that the toroidal plasma is the brightest in the images recorded at 590 nm, whereas this is the converse for the images recorded at 710 nm. This is an indication that the excitation temperature of the microwave generated plasma surrounding the toroidal plasma, and the toroidal plasma itself, are different.

Using the tomographically reconstructed images from the recordings captured through the 590 nm and 710 nm bandpass filters, we can obtain, by applying a standard Boltzmann analysis to each and every pair of pixels, a poloidal excitation temperature profile of our toroidal plasma at 50 μ s. The result of this analysis is shown in figure 5.9, where we present a contour plot of the poloidal excitation temperature profile, and an image showing the same temperature contours combined with the poloidal radiant intensity profile of the 590 nm recording presented in figure 5.8.

The combined temperature contour plot in figure 5.9 shows that the core of the toroidal plasma reaches excitation temperatures in excess of 4500 K. These high temperature regions coincide with the high intensity regions visible in the poloidal radiant intensity profile. A small misalignment can be observed, which we attribute to a possible image

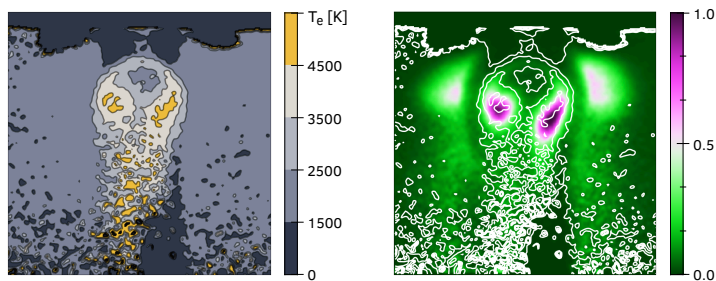


Figure 5.9: (left) Contour plot of the poloidal excitation temperature profile of the microwave generated plasma surrounding the toroidal plasma, and the toroidal plasma itself, obtained from recordings captured 50 μ s after the creation of the laser-induced breakdown plasma responsible for the generation of the toroidal plasma. (right) An image showing the same temperature contours combined with the poloidal radiant intensity profile of the 590 nm recording presented in figure 5.8. The structure visible above the toroidal plasma, across the width of the image, is an artefact of the tomographic reconstruction. The poloidal excitation temperature profile has been obtained by applying a standard Boltzmann analysis to each and every pair of pixels of the poloidal radiant intensity profiles presented in figure 5.8.

displacement between the 590 nm and 710 nm recordings as a result of slightly tilted optical filters, but this requires further investigation.

The microwave generated plasma surrounding the toroidal plasma seems to attain a uniform excitation temperature of the order of 2000 K. In the temperature contour plot the microwave generated plasma is not discernible, instead the entire region outside the toroidal plasma seems to have a uniform temperature. This can be understood when we realise that the optical components used to image the toroidal plasma scatter slightly, and that this scattered light, however minimal, ends up in regions where there is no plasma emission at all. Applying the Boltzmann analysis to these regions, however weak they are, will result in the temperature of the closest source of plasma emission.

Although the excitation temperatures found seem reasonable,¹² a better approach would be to determine the temperature through a Boltzmann analysis based on multiple intensity ratios, obtained from additional atomic helium emission lines.

As a first step towards this approach, we determined the excitation temperature through an additional measurement using a 10 nm bandpass filter with a centre wavelength of 670 nm (Thorlabs FL670-10) enclosing the atomic helium emission line at 667.8 nm. Unfortunately, we found that the obtained temperature was highly sensitive to our spectral amplitude calibration. Although only line intensity ratios are a relevant measure, the bandpass filters still need to be calibrated against a known amplitude calibrated spectrum.¹³ In this process we found that the optical components used in our imaging set-up significantly filter the light captured from our plasma, further complicating this calibration.

Finally, we note that the above analysis provides very reasonable results, compared to the findings in related works, but for detailed and high temperature resolution imaging we need to further substantiate the applicability of the Boltzmann analysis,¹⁴ for example, whether it is permissible to assume local thermodynamic equilibrium and whether the presence of metastable helium affects the analysis.

5.5 Conclusion and discussion

In this chapter we have presented optical recordings of the evolution of a transient toroidal helium plasma subjected to a high power 2.46 GHz microwave pulse, and discussed the electrical characteristics of the pulsed magnetron source during these experiments. We discussed, in detail, the design of the pulsed magnetron source as well as the integration of a 2.465 GHz iris coupled rectangular microwave cavity

¹² Gulec et al. 2015; Monfared et al. 2011; Quintero et al. 1997.

¹³ Specifically, the optical transmission of the bandpass filters needs to be determined precisely at the wavelength of the atomic helium emission lines.

¹⁴ Quintero et al. 1997; Ohno et al. 2006; Boivin et al. 2001; Griem 1997, p. 279.

into our existing set-up for the generation and analysis of toroidal helium plasmas. The microwave cavity has been designed to apply the high power microwave pulses to the toroidal plasma and is mounted directly into the plasma reactor.

The toroidal plasmas studied have been generated by a single laser-induced breakdown plasma, created in quiescent atmospheric pressure helium gas at room temperature. The laser pulse energy used to create the breakdown plasmas was 250 mJ.

We found that the toroidal plasma is unaffected by the microwave pulse, and attributed this to the observation, based on the earlier performed diagnostics experiments at 57 GHz, that the electron number density is far above the critical electron number density for 2.46 GHz radiation. From approximately 52 μs onward, we observed that the microwave pulse generated additional plasma at a distance to the toroidal plasma.

We discussed the dark space between the toroidal plasma and the microwave generated plasma, and presented an experiment whereby the toroidal plasma has been subjected to a +4 kV high-voltage pulse, and where a similar dark space has been observed between the generated ionisation wave and the toroidal plasma.

The evolution of the microwave cavity power and the magnetron current indicate that sub-microsecond rise times are attained and that 2.46 GHz microwave pulses of up to 1.75 kW can be generated. During the 100 μs long microwave pulse, a frequency droop of 5 MHz is observable. We proposed a possible improvement of the stability of the magnetron frequency by injection-locking the magnetron to a low power reference frequency.

We presented a poloidal excitation temperature profile of the microwave generated plasma surrounding the toroidal plasma, and the toroidal plasma itself, obtained from recordings captured through two different 10 nm bandpass filters, captured 50 μs after the creation of the laser-induced breakdown plasma responsible for the generation of the toroidal plasma.

Because the excitation temperature has been determined through a standard Boltzmann analysis, the recorded images have been tomographically reconstructed, to ensure that the intensity ratios of the atomic helium emission lines are a meaningful quantity. We found that the microwave generated plasma and the toroidal plasma are two distinct plasmas. The core of the toroidal plasma has been determined to reach temperatures in excess of 4500 K, whereas the microwave generated plasma appears to have a uniform temperature of

about 2000 K. We discussed the applicability of the Boltzmann analysis, motivated by the sensitivity of the excitation temperature on the spectral amplitude calibration of the imaging set-up.

The results presented above indicate that microwave heating of a region near the toroidal plasma with the developed pulsed magnetron source is feasible. However, reheating of the actual toroidal plasma does not occur. Currently, new microwave cavity designs are being developed, in order to investigate reheating through induction. The use of a cylindrical microwave cavity mode is of particular interest here and experiments are currently underway to implement this mode, in order to sustain the toroidal plasma and realise the sought after magnetic field configurations.

These kinds of sustainable plasma configurations, combined with toroidal fluid flow, are currently also considered in collaboration with the Dutch Institute for Fundamental Energy Research (DIFFER), in order to realise a chemical reactor in which the burning of fuel is replaced by a microwave heated plasma powered by renewable energy, therewith connecting to the quest to reduce CO₂ emission.

Photographs of selected experimental set-ups

To give a more vivid impression of the research presented in this dissertation, we present photographs of selected experimental set-ups used for this research. References are given to the research in this dissertation to which these photos relate.



Photo 1: The pulsed high power optical set-up used to generate the transient toroidal helium plasmas studied in this work. On the left, the Quanta-Ray GCR-3 Q-switched Nd:YAG laser is visible, capable of generating high power 10 ns laser pulses with a wavelength of 1064 nm and with energies up to 275 mJ. On the right, the Continuum NY61-10 laser is visible, similarly capable of generating laser pulses with energies up to 300 mJ. At the top of the photo, a circular aperture is visible in the black aluminium plate, through which the high power laser pulses are guided on their way into the plasma reactor. The dimensions of the breadboard on which the optical set-up has been built is 600 x 450 mm in size. This photo is referenced on page 15 and in figure 2.2.

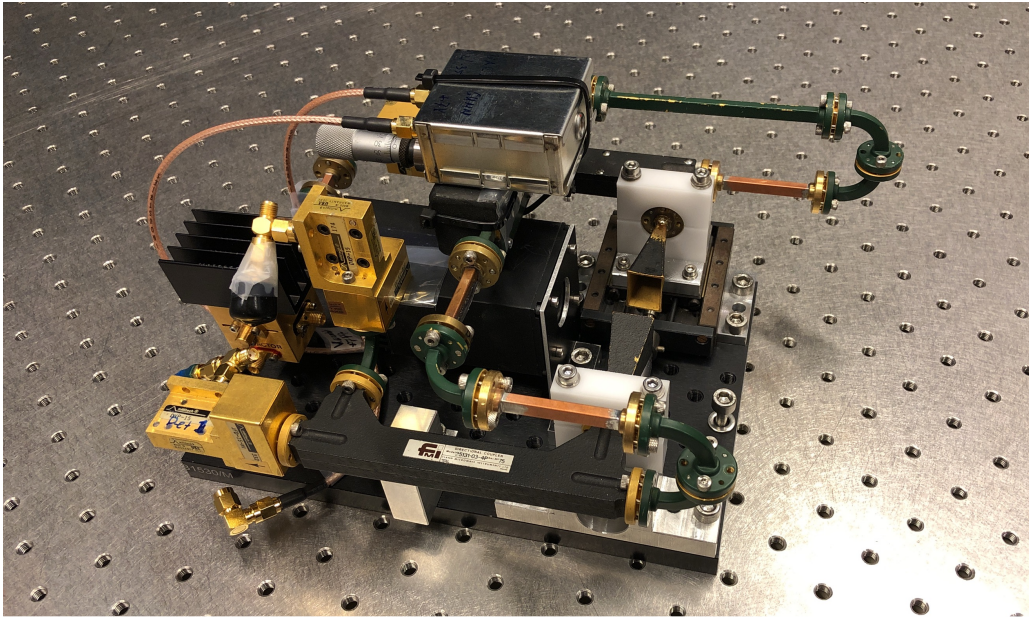


Photo 2: The sub-microsecond temporal resolution, microwave interferometric set-up, used to measure the complex transmission coefficient of 57 GHz microwave radiation traversing a transient toroidal helium plasma. The dimensions of the breadboard on which the interferometer has been built is approximately 230 x 150 mm in size. The copper pyramidal horn antennas, between which the toroidal plasma will be generated, are visible to the right of the breadboard. The central component of the interferometer is the black four-port 90° 3 dB directional coupler visible at the bottom of the breadboard. The microwave radiation is guided through rectangular TE₁₀ mode wave-guide with dimensions of 3.76 x 1.88 mm. During measurements, the whole interferometric set-up will be mounted inside the plasma reactor. This photo is referenced on page 69 and in figure 4.2.

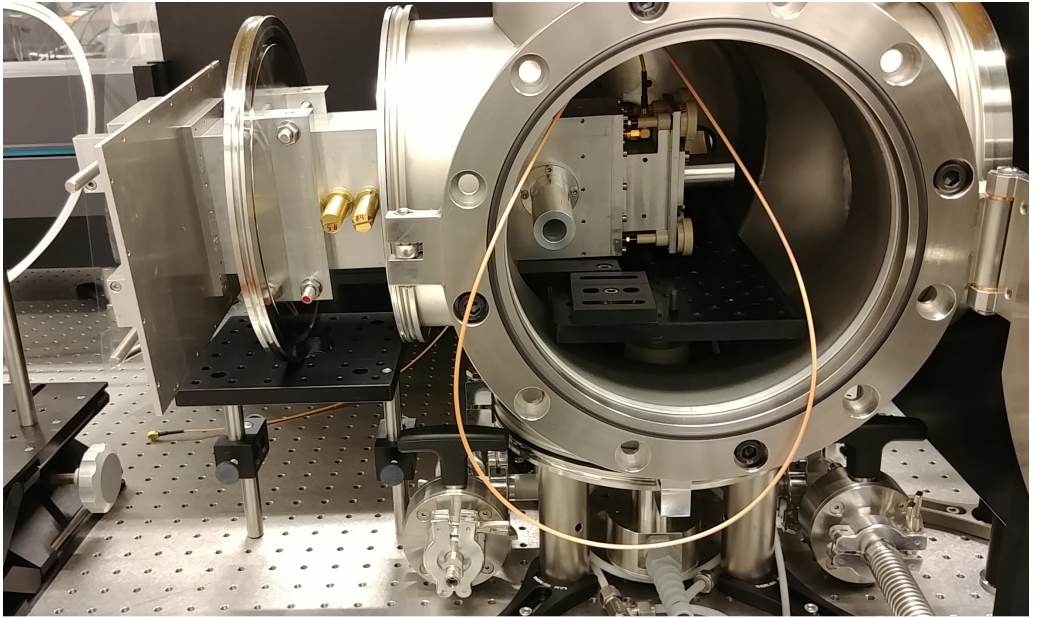


Photo 3: The tailor-made 2.465 GHz iris coupled TE₁₀₁ mode $\lambda_g/2$ rectangular microwave cavity during integration into the plasma reactor. The microwave cavity will be positioned in such a way that the anti-node of the electric field of the TE₁₀₁ mode coincides with the focal point of the lens creating the laser-induced breakdown plasmas from which the toroidal plasmas emerge. The brass stubs just visible to the left of the plasma reactor form the tailor-made three stub tuner. The aluminium beyond cut-off view ports used to let the laser pulses safely enter and exit the microwave cavity, and to image the toroidal plasma from the side, are visible on that part of the microwave cavity, that is already inside the plasma reactor. The microwave cavity goes straight through the left flange of the plasma reactor, and is vacuum sealed to ensure that experiments can be performed in a helium atmosphere. The guide wavelength for the rectangular wave-guide with internal dimensions of 90 x 40 mm is approximately 165 mm. This photo is referenced on page 88 and in figure 5.2.

Bibliography

- Abel N. H. (1826). Auflösung einer mechanischen aufgabe. *Journal für die reine und angewandte Mathematik* 1, 153–157. DOI: [10/dtp6wf](https://doi.org/10/dtp6wf) (cited on p. 26).
- Abramowitz M. and Stegun I. (1972). *Handbook of mathematical functions*. Dover Publications (cited on p. 66).
- Akhmetov D. G. (2009). *Vortex rings*. Springer-Verlag Berlin Heidelberg (cited on p. 22).
- Alberti A., Munafò A., Koll M., Nishihara M., Pantano C., Freund J. B., Elliott G. S. and Panesi M. (2020). Laser-induced non-equilibrium plasma kernel dynamics. *Journal of Physics D: Applied Physics* 53, 025201. DOI: [10/dnkg](https://doi.org/10/dnkg) (cited on pp. 46, 48, 57).
- Alberti A., Munafò A., Pantano C., Freund J. B. and Panesi M. (2019a). Modelling of air breakdown by single-mode and multi-mode lasers. *AIAA Scitech 2019 Forum*, 1250. DOI: [10/dbtn](https://doi.org/10/dbtn) (cited on pp. 22, 46, 48, 57, 58).
- Alberti A., Munafò A., Pantano C., Freund J. B. and Panesi M. (2019b). Radiation supported plasma waves in non-equilibrium laser discharges. *2019 Working Group Radiation of High Temperature Gas, March 26th* (cited on pp. 46, 48, 57).
- Arfken G. B. and Weber H. J. (1995). *Mathematical methods for physicists*. 4th edition. Academic Press (cited on pp. 26, 27).
- Ashcroft N. W. and Mermin N. D. (1976). *Solid state physics*. Saunders College Publishing (cited on pp. 63, 65).
- Atkinson R. and Lissberger P. H. (1992). Sign conventions in magneto-optical calculations and measurements. *Applied Optics* 31, 6076–6081. DOI: [10/fgwh6m](https://doi.org/10/fgwh6m) (cited on p. 71).
- Bak M. S., Im S. and Cappelli M. A. (2014). Successive laser-induced breakdowns in atmospheric pressure air and premixed ethane-air mixtures. *Combustion and Flame* 161, 1744–1751. DOI: [10/f56s6n](https://doi.org/10/f56s6n) (cited on pp. 10, 14, 22, 45, 53).

- Bak M. S., Wermer L. and Im S. (2015). Schlieren imaging investigation of successive laser-induced breakdowns in atmospheric-pressure air. *Journal of Physics D: Applied Physics* 48, 485203. DOI: [10/dbg5](#) (cited on pp. [10](#), [14](#), [22](#), [23](#), [45](#), [53](#)).
- Bellan P. M. (2006). *Fundamentals of plasma physics*. Cambridge University Press (cited on p. [66](#)).
- Besant W. H. (1859). *A treatise on hydrostatics and hydrodynamics*. Deighton, Bell, and Co. (cited on p. [33](#)).
- Bethe H. A., Fuchs K., Hirschfelder J. O., Magee J. L., Peierls R. E. and Von Neumann J. (1958). *Blast wave*. Los Alamos Scientific Laboratory New Mexico (cited on p. [53](#)).
- Boivin R. F., Kline J. L. and Scime E. E. (2001). Electron temperature measurement by a helium line intensity ratio method in helicon plasmas. *Physics of Plasmas* 8, 5303. DOI: [10/b4mcnd](#) (cited on p. [99](#)).
- Bracewell R. N. (1956). Strip integration in radio astronomy. *Australian Journal of Physics* 9, 198–217. DOI: [10/fvr5xr](#) (cited on p. [27](#)).
- Bradley D., Sheppard C. G. W., Suardjaja I. M. and Woolley R. (2004). Fundamentals of high-energy spark ignition with lasers. *Combustion and Flame* 138, 55–77. DOI: [10/fqfq3b](#) (cited on pp. [10](#), [14](#), [22](#), [45](#), [54](#)).
- Broekaert J. A. C. and Siemens V. (2004). Recent trends in atomic spectrometry with microwave-induced plasmas. *Spectrochimica Acta Part B: Atomic Spectroscopy* 59, 1823–1839. DOI: [10/dz45kv](#) (cited on p. [88](#)).
- Candel S. M. (1981). An algorithm for the fourier-bessel transform. *Computer Physics Communications* 23, 343–353. DOI: [10/cdp6t5](#) (cited on p. [27](#)).
- Carbone E. A. D., Schregel C. G. and Czarnetzki U. (2016). Ignition and afterglow dynamics of a high pressure nanosecond pulsed helium micro-discharge: ii. rydberg molecules kinetics. *Plasma Sources Science and Technology* 25, 054004. DOI: [10/dmqd](#) (cited on pp. [21](#), [45](#)).
- Chanin L. M., Phelps A. V. and Biondi M. A. (1962). Measurements of the attachment of low-energy electrons to oxygen molecules. *Physical Review* 128, 219. DOI: [10/fjf4r7](#) (cited on pp. [42](#), [44](#), [45](#)).
- Chen F. F. (1974). *Introduction to plasma physics*. Plenum Press (cited on pp. [9](#), [10](#), [61](#), [63](#), [66](#), [67](#), [77](#), [81](#)).
- Chen Y., Lewis J. W. L. and Parigger C. (2000). Spatial and temporal profiles of pulsed laser-induced air plasma emissions. *Journal of Quantitative Spectroscopy and Radiative Transfer* 67, 91–103. DOI: [10/b95r8g](#) (cited on pp. [23](#), [33](#), [48](#)).
- Chorin A. J. and Marsden J. E. (1993). *A mathematical introduction to fluid mechanics*. 3rd edition. Springer-Verlag New York (cited on pp. [61–63](#)).

- Cioffi D. F. (1990). Supernova remnants as probes of the interstellar medium. *Physical Processes in Hot Cosmic Plasmas*, 1–16. DOI: [10/dvt2](https://doi.org/10/dvt2) (cited on pp. 53, 54).
- Collin R. E. (2001). *Foundations for microwave engineering*. 2nd edition. Wiley-IEEE Press (cited on p. 71).
- Cooper J. (1966). Plasma spectroscopy. *Reports on Progress in Physics* 29, 35–130. DOI: [10/fw3p5n](https://doi.org/10/fw3p5n) (cited on pp. 21, 26, 27, 29).
- Cristoforetti G., Legnaioli S., Pardini L., Palleschi V., Salvetti A. and Tognoni E. (2006). Spectroscopic and shadowgraphic analysis of laser induced plasmas in the orthogonal double pulse pre-ablation configuration. *Spectrochimica Acta Part B: Atomic Spectroscopy* 61, 340–350. DOI: [10/bcvs2j](https://doi.org/10/bcvs2j) (cited on pp. 54, 57).
- de Klerk A. J. J. M., van der Veen R. I., Dalhuisen J. W. and Bouwmeester D. (2017). Knotted optical vortices in exact solutions to maxwell's equations. *Physical Review A* 95, 053820. DOI: [10/fbfc](https://doi.org/10/fbfc) (cited on p. 10).
- Dribinski V., Ossadtchi A., Mandelshtam V. A. and Reisler H. (2002). Reconstruction of abel-transformable images: the gaussian basis-set expansion abel transform method. *Review of Scientific Instruments* 73, 2634–2642. DOI: [10/d7pm4v](https://doi.org/10/d7pm4v) (cited on pp. 26, 27).
- Drude P. (1900). Zur elektronentheorie der metalle. *Annalen der Physik* 306, 566. DOI: [10/cmck9z](https://doi.org/10/cmck9z) (cited on p. 63).
- Dumitrache C., VanOsdol R., Limbach C. M. and Yalin A. P. (2017). Control of early flame kernel growth by multi-wavelength laser pulses for enhanced ignition. *Scientific Reports* 7, 10239. DOI: [10/gbwm93](https://doi.org/10/gbwm93) (cited on pp. 10, 14, 22, 45).
- Fridman A. (2008). *Plasma chemistry*. Cambridge University Press (cited on p. 91).
- Gharib M., Mendoza S., Rosenfeld M., Beizai M. and Pereira F. J. A. (2017). Toroidal plasmoid generation via extreme hydrodynamic shear. *Proceedings of the National Academy of Sciences* 114, 12657–12662. DOI: [10/gcn523](https://doi.org/10/gcn523) (cited on pp. 10, 14).
- Ghosh S. and Mahesh K. (2008). Numerical simulation of the fluid dynamic effects of laser energy deposition in air. *Journal of Fluid Mechanics* 605, 329–354. DOI: [10/fkqmf7](https://doi.org/10/fkqmf7) (cited on pp. 22, 23, 39, 45, 48).
- Glasstone S. and Dolan P. J. (1977). *The effects of nuclear weapons*. 3rd edition. Department of Defense Washington D.C. (cited on p. 57).
- Goedbloed J. P. and Poedts S. (2004). *Principles of magnetohydrodynamics, with applications to laboratory and astrophysical plasmas*. Cambridge University Press (cited on p. 66).

- Griem H. R. (1997). *Principles of plasma spectroscopy*. Cambridge University Press (cited on pp. 27, 29, 97, 99).
- Griffiths D. J. (1999). *Introduction to electrodynamics*. 3rd edition. Prentice Hall (cited on p. 64).
- Gulec A., Bozduman F. and Hala A. M. (2015). Atmospheric pressure 2.45-ghz microwave helium plasma. *IEEE Transactions on Plasma Science* 43, 786–790. DOI: [10/f67rzc](https://doi.org/10/f67rzc) (cited on pp. 97, 99).
- Hammer M. R. (2008). A magnetically excited microwave plasma source for atomic emission spectroscopy with performance approaching that of the inductively coupled plasma. *Spectrochimica Acta Part B: Atomic Spectroscopy* 63, 456–464. DOI: [10/dx7qkc](https://doi.org/10/dx7qkc) (cited on p. 88).
- Hanson K. M. (1993). Special topics in test methodology: tomographic reconstruction of axially symmetric objects from a single dynamic radiograph. *Progress in Astronautics and Aeronautics* 155, 687–698 (cited on pp. 26, 29).
- Harilal S. S., Brumfield B. E. and Phillips M. C. (2015). Lifecycle of laser-produced air sparks. *Physics of Plasmas* 22, 063301. DOI: [10/f7jffs](https://doi.org/10/f7jffs) (cited on pp. 10, 14, 22, 23, 33, 45, 48).
- Haynes W. M. (2014). *CRC handbook of chemistry and physics*. 95th edition. CRC Press (cited on pp. 23, 32, 34, 45).
- Hutchinson I. H. (2002). *Principles of plasma diagnostics*. 2nd edition. Cambridge University Press (cited on pp. 21, 26, 27).
- IEA (2017). *World energy balances: data and statistics*. International Energy Agency, Paris (cited on p. 9).
- Irvine W. T. M. and Bouwmeester D. (2008). Linked and knotted beams of light. *Nature Physics* 4, 716–720. DOI: [10/d23t2b](https://doi.org/10/d23t2b) (cited on p. 10).
- Jackson J. D. (1998). *Classical electrodynamics*. 3rd edition. John Wiley & Sons (cited on p. 64).
- Jeans J. H. (1940). *An introduction to the kinetic theory of gases*. Cambridge University Press (cited on pp. 22, 32).
- Kabouzi Y., Calzada M. D., Moisan M., Tran K. C. and Trassy C. (2002). Radial contraction of microwave-sustained plasma columns at atmospheric pressure. *Journal of Applied Physics* 91, 1008. DOI: [10/ccpkj2](https://doi.org/10/ccpkj2) (cited on pp. 77, 81).
- Kamchatnov A. M. (1982). Topological solitons in magnetohydrodynamics. *Soviet Physics Journal of Experimental and Theoretical Physics* 55, 69–73 (cited on p. 10).
- Kedia H., Bialynicki-Birula I., Peralta-Salas D. and Irvine W. T. M. (2013). Tying knots in light fields. *Physical Review Letters* 111, 150404. DOI: [10/ggh6pb](https://doi.org/10/ggh6pb) (cited on p. 10).

- Kopp G. and Lean J. L. (2011). A new, lower value of total solar irradiance: evidence and climate significance. *Geophysical Research Letters* 38, L01706. DOI: [10/b9tkk2](https://doi.org/10.1029/2010GL014601) (cited on p. 9).
- Kramida A., Ralchenko Y., Reader J. and NIST ASD Team (2019). NIST atomic spectra database. *National Institute of Standards and Technology*. DOI: [10/dmk4](https://doi.org/10.18130/20190001) (cited on p. 21).
- Krehl P. (2011). Shock wave physics and detonation physics - a stimulus for the emergence of numerous new branches in science and engineering. *The European Physical Journal H* 36, 85–152. DOI: [10/bsdwtq](https://doi.org/10.1051/epjh/2011361001) (cited on p. 57).
- Krehl P. and Van der Geest M. (1991). The discovery of the mach reflection effect and its demonstration in an auditorium. *Shock Waves* 1, 3–15. DOI: [10/bb23dx](https://doi.org/10.1007/BF01614800) (cited on p. 57).
- Kulsrud R. M. (2005). *Plasma physics for astrophysics*. Princeton University Press (cited on p. 66).
- Landau L. D. and Lifshitz E. M. (1987). *Fluid mechanics*. 2nd edition. Pergamon Press Oxford (cited on pp. 23, 34).
- Mach E. and Mach L. (1890). Ueber die interferenz der schallwellen von grosser excursion. *Annalen der Physik* 277, 140–143. DOI: [10/bvq5gs](https://doi.org/10.1007/BF02111400) (cited on p. 57).
- Marder M. P. (2010). *Condensed matter physics*. 2nd edition. John Wiley & Sons (cited on p. 66).
- Matusiewicz H. (1992). A novel microwave plasma cavity assembly for atomic emission spectrometry. *Spectrochimica Acta Part B: Atomic Spectroscopy* 47, 1221–1227. DOI: [10/dcmfcb](https://doi.org/10.1016/0883-2927(92)90001-8) (cited on p. 88).
- Miziolek A. W., Palleschi V. and Schechter I. (2006). *Laser induced breakdown spectroscopy*. Cambridge University Press (cited on pp. 23, 48).
- Moffatt H. K. (1969). The degree of knottedness of tangled vortex lines. *Journal of Fluid Mechanics* 35, 117–129. DOI: [10/fh75pf](https://doi.org/10.1017/jfm.1969.100) (cited on pp. 9, 13).
- Monfared S. K., Graham W. G., Morgan T. J. and Huwel L. (2011). Spectroscopic characterization of laser-produced atmospheric pressure helium microplasmas. *Plasma Sources Science and Technology* 20, 035001. DOI: [10/d8xg6g](https://doi.org/10.1088/0963-0252/20/3/035001) (cited on pp. 97, 99).
- Morsy M. H. and Chung S. H. (2002). Numerical simulation of front lobe formation in laser-induced spark ignition of ch₄/air mixtures. *Proceedings of the Combustion Institute* 29, 1613–1619. DOI: [10/fmp2ht](https://doi.org/10.1016/S0081-8993(02)00021-1) (cited on pp. 22, 39, 45).
- Muller R. H. (1969). Definitions and conventions in ellipsometry. *Surface Science* 16, 14–33. DOI: [10/c3674v](https://doi.org/10.1016/0039-2909(69)90001-1) (cited on p. 71).

- Nassif D. and Hüwel L. (2000). Appearance of toroidal structure in dissipating laser-generated sparks. *Journal of Applied Physics* 87, 2127–2130. DOI: [10/dp3n7c](#) (cited on pp. 10, 14, 22, 23, 45).
- Nedanovska E., Nersisyan G., Morgan T. J., Huwel L., Murakami T., Lewis C. L. S., Riley D. and Graham W. G. (2015). Investigating the dynamics of laser induced sparks in atmospheric helium using rayleigh and thomson scattering. *Journal of Applied Physics* 117, 013302. DOI: [10/fj4v](#) (cited on pp. 45, 60, 82).
- Nishihara M., Freund J. B., Glumac N. G. and Elliott G. S. (2018). Influence of mode-beating pulse on laser-induced plasma. *Journal of Physics D: Applied Physics* 51, 135601. DOI: [10/dbmd](#) (cited on pp. 22, 46).
- Nyswander R. E. and Auger G. J. (1976). Nanosecond pulse generators for magnetron operation. *Naval Weapons Center China Lake CA*, ADA636968 (cited on p. 87).
- Ohno N., Razzak M. A., Ukai H., Takamura S. and Uesugi Y. (2006). Validity of electron temperature measurement by using boltzmann plot method in radio frequency inductive discharge in the atmospheric pressure range. *Plasma and Fusion Research* 1, 028. DOI: [10/dm7xwq](#) (cited on p. 99).
- Pokrzywka B., Mendys A., Dzierzega K., Grabiec M. and Pellerin S. (2012). Laser light scattering in a laser-induced argon plasma: investigations of the shock wave. *Spectrochimica Acta Part B: Atomic Spectroscopy* 74–75, 24–30. DOI: [10/fkxc](#) (cited on p. 60).
- Pretzler G. (1991). A new method for numerical abel-inversion. *Zeitschrift für Naturforschung A* 46, 639–641. DOI: [10/dmzs](#) (cited on p. 27).
- Pretzler G., Jäger H., Neger T., Philipp H. and Woisetschläger J. (1992). Comparison of different methods of abel inversion using computer simulated and experimental side-on data. *Zeitschrift für Naturforschung A* 47, 955–970. DOI: [10/gfz8fs](#) (cited on pp. 26, 27, 30).
- Quintero M. C., Rodero A., Garcia M. C. and Sola A. (1997). Determination of the excitation temperature in a nonthermodynamic-equilibrium high-pressure helium microwave plasma torch. *Applied Spectroscopy* 51, 778–784. DOI: [10/d3qzqb](#) (cited on p. 99).
- Raizer Y. P. (1991). *Gas discharge physics*. Springer-Verlag Berlin Heidelberg (cited on pp. 23, 42, 44, 48).
- Rañada A. F. (1989). A topological theory of the electromagnetic field. *Letters in Mathematical Physics* 18, 97–106. DOI: [10/b3c4jr](#) (cited on p. 10).

- Rayleigh L. (1917). On the pressure developed in a liquid during the collapse of a spherical cavity. *The London, Edinburgh, and Dublin Philosophical Magazine and Journal of Science* 6, 94–98. DOI: [10/fwxkvm](https://doi.org/10/fwxkvm) (cited on p. 33).
- Richardson A. S. (2019). *NRL Plasma Formulary*. Naval Research Laboratory, Washington, DC (cited on pp. 77, 81, 82).
- Rybicki G. B. and Lightman A. P. (1979). *Radiative processes in astrophysics*. John Wiley & Sons (cited on p. 21).
- Schregel C. G., Carbone E. A. D., Luggenholscher D. and Czarnetzki U. (2016). Ignition and afterglow dynamics of a high pressure nanosecond pulsed helium micro-discharge: i. electron, rydberg molecules and he (23s) densities. *Plasma Sources Science and Technology* 25, 054003. DOI: [10/dmqc](https://doi.org/10/dmqc) (cited on pp. 21, 45).
- Sedov L. I. (1959). *Similarity and dimensional methods in mechanics*. Academic Press (cited on pp. 53, 54).
- Settles G. S. (2001). *Schlieren and shadowgraph techniques*. Springer-Verlag Berlin Heidelberg (cited on pp. 18, 51, 55).
- Seward C. (2014). Ball lightning events explained as self-stable spinning high-density plasma toroids or atmospheric spheromaks. *IEEE Access* 2, 153–159. DOI: [10/dkxt](https://doi.org/10/dkxt) (cited on pp. 10, 14).
- Shu F. H. (1992). *The physics of astrophysics: gas dynamics*. University Science Books (cited on p. 53).
- Sinibaldi G., Occhicone A., Alves Pereira F., Caprini D., Marino L., Michelotti F. and Casciola C. M. (2019). Laser induced cavitation: plasma generation and breakdown shockwave. *Physics of Fluids* 31, 103302. DOI: [10/dpvz](https://doi.org/10/dpvz) (cited on p. 33).
- Smerlak M. (2011). A blackbody is not a blackbox. *European Journal of Physics* 32, 1143. DOI: [10/bcznd2](https://doi.org/10/bcznd2) (cited on p. 21).
- Smiet C. B. (2017). *Knots in plasma*. Casimir PhD series Leiden Delft (cited on pp. 10, 59).
- Smiet C. B., Candelaresi S., Thompson A., Swearngin J., Dalhuisen J. W. and Bouwmeester D. (2015). Self-organizing knotted magnetic structures in plasma. *Physical Review Letters* 115, 095001. DOI: [10/dkts](https://doi.org/10/dkts) (cited on pp. 10, 11, 14).
- Smiet C. B., de Blank H. J., de Jong T. A., Kok D. N. L. and Bouwmeester D. (2019). Resistive evolution of toroidal field distributions and their relation to magnetic clouds. *Journal of Plasma Physics* 85, 905850107. DOI: [10/fbwt](https://doi.org/10/fbwt) (cited on pp. 10, 59).
- Smith L. M., Keefer D. R. and Sudharsanan S. I. (1988). Abel inversion using transform techniques. *Journal of Quantitative Spectroscopy and Radiative Transfer* 39, 367–373. DOI: [10/fhzgsq](https://doi.org/10/fhzgsq) (cited on pp. 26, 27).

- Spanel P., Hall E. F. H., Workman C. T. and Smith D. (2004). A directly coupled monolithic rectangular resonator forming a robust microwave plasma ion source for sift-ms. *Plasma Sources Science and Technology* 13, 282–284. DOI: [10/bsphgx](#) (cited on p. 88).
- Stepanyan S., Minesi N., Tibère-Inglesse A., Salmon A., Stancu G. D. and Laux C. O. (2019). Spatial evolution of the plasma kernel produced by nanosecond discharges in air. *Journal of Physics D: Applied Physics* 52, 295203. DOI: [10/dkxs](#) (cited on pp. 10, 14).
- Stevelfelt J. and Johansson J. (1971). Measurements of the spectral light emission from decaying high pressure helium plasmas. *AB Atomenergi, Nykoeping, Sweden, AE-418* (cited on p. 45).
- Tahir I., Dexter A. and Carter R. (2006). Frequency and phase modulation performance of an injection-locked cw magnetron. *IEEE Transactions on Electron Devices* 53, 1721–1729. DOI: [10/c52h72](#) (cited on p. 96).
- Taylor G. I. (1950a). The formation of a blast wave by a very intense explosion i. theoretical discussion. *The Proceedings of the Royal Society of London A* 201, 159–174. DOI: [10/fj2s7h](#) (cited on p. 53).
- Taylor G. I. (1950b). The formation of a blast wave by a very intense explosion. ii. the atomic explosion of 1945. *The Proceedings of the Royal Society of London A* 201, 175–186. DOI: [10/b7v6cp](#) (cited on p. 53).
- Taylor J. B. (1974). Relaxation of toroidal plasma and generation of reverse magnetic fields. *Physical Review Letters* 33, 1139–1141. DOI: [10/cnczw2](#) (cited on p. 10).
- Thompson A., Swearingin J. and Bouwmeester D. (2014). Linked and knotted gravitational radiation. *Journal of Physics A: Mathematical and Theoretical* 47, 355205. DOI: [10/fbfd](#) (cited on p. 10).
- Tonks L. and Langmuir I. (1929). Oscillations in ionized gases. *Physical Review* 33, 195. DOI: [10/bjfr8n](#) (cited on p. 61).
- Wagner W. G. and Lengyel B. A. (1963). Evolution of the giant pulse in a laser. *Journal of Applied Physics* 34, 2040. DOI: [10/brrss4](#) (cited on p. 48).
- Waldron R. A. (1960). Perturbation theory of resonant cavities. *Proceedings of the IEE - Part C: Monographs* 107, 272–274. DOI: [10/d6khgq](#) (cited on p. 96).
- Wesson J. (2004). *Tokamaks*. 3rd edition. Clarendon Press Oxford (cited on p. 61).
- Williams T. C. and Shaddix C. R. (2007). Simultaneous correction of flat field and nonlinearity response of intensified charge-coupled devices. *Review of Scientific Instruments* 78, 123702. DOI: [10/ft2r97](#) (cited on p. 17).

- Woltjer L. (1958). A theorem on force-free magnetic fields. *Proceedings of the National Academy of Sciences* 44, 489–491. DOI: [10/btg2w8](https://doi.org/10/btg2w8) (cited on pp. 9, 13).
- Ye Y., Spina D., Xing Y., Bogaerts W. and Dhaene T. (2018). Numerical modeling of a linear photonic system for accurate and efficient time-domain simulations. *Photonics Research* 6, 560–573. DOI: [10 / d3hz](https://doi.org/10/d3hz) (cited on p. 71).
- Zel'dovich Y. B. and Raizer Y. P. (1966). *Physics of shock waves and high-temperature hydrodynamic phenomena*. Academic Press (cited on pp. 53, 54).

Samenvatting

In slechts veertig minuten is de hoeveelheid energie die wij op aarde van de zon ontvangen meer dan het jaarlijkse energieverbruik van de gehele wereld. Deze simpele observatie is de belangrijkste motivatie geweest voor de wereldwijde inspanningen voor kernfusie. Een halve eeuw toegewijd onderzoek heeft echter niet geresulteerd in een betrouwbare en rendabele kernfusiecentrale.

Toch biedt kernfusie een mogelijk antwoord in de zoektocht naar duurzame energie, in het algemeen beschouwd als een van de grootste uitdagingen waarmee de mensheid in de komende decennia wordt geconfronteerd. Om de thermonucleaire reacties voor kernfusie te kunnen laten plaatsvinden zijn plasma's met een temperatuur van in de orde van 100 miljoen graden Celsius noodzakelijk. Om deze thermonucleaire reacties in stand te houden is het van belang dat het hete plasma voldoende lang en met voldoende hoge dichtheid wordt opgesloten. In hedendaags kernfusieonderzoek is magnetische opsluiting de meest gevolgde strategie hiervoor.

Al in de jaren vijftig bedachten fysici in de Sovjet-Unie de tokamak. Deze apparaten gebruiken sterke magnetische velden om het plasma met een hoge temperatuur in de vorm van een torus op te sluiten en vormen het leidende ontwerp voor een economisch levensvatbare kernfusiereactor.

Het begrijpen van de stabiliteit van magnetisch opgesloten plasma's is derhalve van fundamenteel belang voor een succesvolle kernfusiereactor op basis van magnetische opsluiting. De topologie van de gebruikte magnetische velden blijkt daarin een cruciale rol te spelen.

Het verband tussen stabiliteit en topologie werd in 1969 gelegd toen Moffatt ontdekte dat helicititeit, een door Woltjer gevonden behouden grootheid in een plasma met oneindige geleidbaarheid, in feite een maat is in hoeverre magnetische veldlijnen geknoopt en geschakeld zijn.

Kamchatnov construeerde, uitgaande van de topologische aard van deze invariant, een magnetische veldconfiguratie die bestaat uit

gesloten magnetische veldlijnen die allemaal met elkaar geschakeld zijn. Daarmee verkreeg hij een analytische oplossing van de vergelijkingen van de magnetohydrodynamica voor een ideaal plasma.

Recent is het verband tussen stabiliteit en topologie bevestigd in magnetohydrodynamische simulaties die aantonen dat een magnetisch veld met heliceit zichzelf herconfigureert tot een structuur van gelaagde toroïdale oppervlakken. Deze zelforganiserende geknoopte magnetische structuren zijn intrinsiek stabiel en hun configuratie verschilt wezenlijk van die van de tokamak. Hun hydrostatische druk is namelijk minimaal op de centrale cirkel van de gelaagde toroïdale oppervlakken. De magnetische energiedichtheid van deze geknoopte plasmastructuren is sterk gelokaliseerd, waarbij de magnetische druk gecompenseerd wordt door de hydrostatische druk.

De door de wetenschappers uit de Sovjet-Unie bedachte tokamak zou theoretisch een stabiel plasma moeten opleveren, maar experimenteel is het evenwicht instabiel en leidt het tot chaotische plasmadynamica. Het beheersen van deze chaotische dynamica speelt een belangrijke rol in de hedendaagse experimenten met magnetische opsluiting van plasma's.

In plaats van proberen deze chaos te beheersen kunnen de zelforganiserende geknoopte magnetische structuren wellicht uitkomst bieden omdat zij uit zichzelf de gewenste stabiliteit bieden. Bovendien suggereert hun schijnbare universaliteit dat deze stabiele structuren eveneens in astrofysische omgevingen kunnen ontstaan, wat duidt op een meer fundamentele rol.

Toroïdale plasmastructuren zijn waargenomen in een breed scala van experimenten, variërend van krachtige elektrische bogen tot laser-geïnduceerde plasma's. Het onderzoek gepresenteerd in dit proefschrift vindt zijn oorsprong bij de waarneming van toroïdale plasmastructuren die veel symmetrischer zijn dan de eerder waargenomen structuren. Deze plasmastructuren werden gegenereerd met behulp van laser-geïnduceerde plasma's, gecreëerd in atmosferisch helium gas bij kamertemperatuur. De zelforganiserende toroïdale structuur, maar ook de atmosferische omgevingscondities van deze laser-gegenereerde toroïdale plasma's, bieden een interessante setting voor het onderzoeken van de numeriek voorspelde, en intrinsiek stabiele, zelforganiserende geknoopte magnetische structuren.

Het lange-termijn doel is de realisatie van zulke zelforganiserende geknoopte magnetische structuren in het laboratorium. Dit proefschrift is een verslag van de eerste stappen in die richting en bespreekt de belangrijkste kenmerken die verantwoordelijk zijn voor de ontwikkeling

van de laser-gegenereerde toroïdale heliumplasma's, tezamen met hun voornaamste plasmaparameters. Tevens wordt het onderzoek naar het tegengaan van hun tijdelijke aard besproken, een eigenschap die evident de realisatie van zelforganiserende magnetische structuren belemmert.

Het onderzoek vangt aan in hoofdstuk 2, waar voor de gehele evolutie van een toroïdaal plasma, tomografisch gereconstrueerde, poloidale, intensiteitsprofielen worden getoond die duidelijk de vormende gasstroom van de toroïdale structuur zichtbaar maken. De waarnemingen tonen tevens een nieuwe opsplitsing van het toroïdale plasma gedurende de laatste fase van de plasma evolutie. Op basis van elementaire thermodynamische principes wordt een model ontwikkeld dat een karakteristieke tijdschaal bepaalt waarmee structuur zich naar verwachting zal ontwikkelen. Deze tijdschaal wordt bevestigd door metingen van de dichtheid van de heliumatomen in het centrum van het toroïdale plasma. Door de symmetrie van de gasstroom die verantwoordelijk is voor de ontwikkeling van de toroïdale structuur opzettelijk te breken wordt het model voor de vorming van deze structuur bevestigd. De pulsaties die zijn waargenomen tijdens het ontsteken van een lasergeïnduceerd plasma worden als laatste besproken. Deze zich herhalende dynamiek draagt mogelijk bij aan de vorming van de dubbele structuur die zichtbaar is in de plasmakern.

In hoofdstuk 3 wordt een nieuwe interpretatie van snelle Schlierenafbeeldingen gepresenteerd, waarin een Mach-reflectie van schokgolven zichtbaar is die gevormd wordt door de dubbele structuur van de plasmakern van een lasergeïnduceerd plasma. De sterkte van deze Mach-reflectie wordt gerelateerd aan de asymmetrische gasstroming die noodzakelijk is voor de ontwikkeling van de toroïdale plasma's. De voortplanting van de schokgolf wordt gevisualiseerd met een nieuwe techniek waarbij een tweede lasergeïnduceerd plasma gebruikt wordt als een sonde. Hiermee wordt ook het bestaan van een holte met lage dichtheid bevestigd die in het kielzog van de schokgolf wordt gevormd.

Hoofdstuk 4 behandelt de plasmaparameters van de toroïdale plasma's. Door interferometrische metingen met 57 GHz microgolffstraling te combineren met gedetailleerde eindige-elementen berekeningen, wordt voor de gehele evolutie en met sub-microseconde temporele resolutie, de elektronendichtheid en de elektronen botsingsfrequentie van een toroïdaal plasma geschat. De microgolf interferometrische opstelling die gebruikt is om de complexe transmissiecoëfficiënt te bepalen wordt in detail besproken. Verder wordt er een methode besproken waarbij de eindige-elementen berekeningen gebruikt worden

om uit de gemeten transmissiecoëfficiënt de gezochte plasmaparameters te bepalen. Als ondersteuning worden er een aantal fundamentele concepten uit de plasmafysica behandeld.

Om de tijdelijke aard van de toroïdale heliumplasma's tegen te gaan is er een 1,75 kW gepulseerde magnetronbron met een stijgtijd van minder dan een microseconde ontworpen, waarvan in hoofdstuk 5 het ontwerp in detail wordt besproken. Deze magnetronbron is gebruikt in verkennende experimenten gericht op het verhitten van het plasma door de absorptie van microgolfstraling. Gedurende deze experimenten zijn de elektrische eigenschappen van de magnetronbron bepaald. In deze experimenten is het toroïdale plasma onderworpen aan een sterke microgolfpuls van 2,460 GHz, een frequentie die algemeen gebruikt wordt door industriële microgolfbronnen. Om het toroïdale plasma aan de microgolfpuls te onderwerpen is er een 2,465 GHz iris gekoppelde rechthoekige microgolf trilholtte ontworpen. De 5 MHz verschuiving anticipeert op een verstemming van de trilholtte als gevolg van de aanwezigheid van plasma. Het effect van de microgolfpuls op het toroïdale plasma, alsmede het donkere gebied dat waarneembaar is tussen het door de microgolven gegenereerde plasma en het toroïdale plasma, worden besproken. Als laatste wordt er een poloïdaal excitatie temperatuurprofiel gepresenteerd van het toroïdale plasma, inclusief de extra plasmastructuur gegenereerd door de microgolfpuls. Het temperatuurprofiel is bepaald door toepassing van een standaard Boltzmann analyse op twee tomografisch gereconstrueerde poloïdale intensiteitsprofielen, welke verkregen zijn uit afbeeldingen gemaakt bij twee verschillende golflengten.

De gepresenteerde resultaten geven aan dat microgolfverwarming van een gebied nabij het toroïdale heliumplasma met de ontwikkelde gepulste magnetronbron mogelijk is. Opwarming van het eigenlijke toroïdale plasma vindt echter niet plaats, waardoor de gezochte gelinkte magnetische structuren nog niet gerealiseerd kunnen worden. Momenteel worden er nieuwe ontwerpen voor microgolf trilholtes ontwikkeld om verwarming door inductie te onderzoeken. Dit soort plasmaconfiguraties, gecombineerd met toroïdale gasstroming, worden momenteel ook overwogen in samenwerking met het Dutch Institute for Fundamental Energy Research (DIFFER) om een chemische reactor te realiseren waarin het verbranden van brandstof wordt vervangen door een microgolfverwarmd plasma. In het geval deze chemische reactoren gevoed zouden worden uit hernieuwbare energiebronnen, dan wordt de CO₂-uitstoot van deze processen significant gereduceerd.

Curriculum Vitae

Vincent Kooij

Education

Leiden University

Doctor of Philosophy (PhD), Experimental Physics
2015 – 2020 | *Leiden, The Netherlands*

Leiden University

Master of Science (MSc), Theoretical Physics, cum laude
1998 – 2003 | *Leiden, The Netherlands*

Institute for Advanced Electronics Rens & Rens

Ingenieursdiploma, Electronic Engineering, cum laude
1992 – 1997 | *Hilversum, The Netherlands*

Technical Secondary School Dominicus Savio

Secondary education, Electro-technical
1988 – 1992 | *Amsterdam, The Netherlands*

Corporate and academic experience

Founder and Principal

Silicon Research
December 1997 – Present | Amsterdam, The Netherlands

Founded a management and engineering consultancy specialising in bespoke solutions for the renewable energy, environmental, automotive, and other specialist industries requiring highly innovative products and services. Clients include governmental organisations in the Caribbean and the Netherlands, as well as corporations in the broadcasting services and maritime sector.

Doctoral Researcher

Huygens-Kamerlingh Onnes Laboratory (Leiden University)
July 2015 – October 2020 | Leiden, The Netherlands

Worked towards a PhD in experimental physics in the group of Spinoza laureate prof. dr. Dirk Bouwmeester. Studied laser-generated toroidal

*Corporate and
academic experience
(cont.)*

helium plasmas, as part of a larger study on self-organising knotted magnetic structures in plasma, which may find their application in nuclear fusion and astrophysical research.

Served as a teaching assistant for the quantum mechanics lecture series for four consecutive years.

Dissertation: Laser-generated toroidal helium plasmas.

Supervisors: prof. dr. D. Bouwmeester and dr. M. de Dood.

Interim Plant Manager

ContourGlobal

July 2010 – March 2014 | Bonaire, Netherlands Antilles

Provided operational and technical leadership to the \$56 million hybrid wind diesel power plant, with full day-to-day responsibility for its \$20 million annual operations, first at Ecopower Bonaire, and after its acquisition in 2013, at ContourGlobal Bonaire. Led the commissioning of the hybrid wind diesel power plant in 2010. Recovered the plant from a near bankruptcy. Participated in the arbitration against the government-owned distribution company over a tariff dispute. Award granted on all material grounds, thereby transforming the power plant into a profitable and reliable business. Participated in the successful share transfer to ContourGlobal in 2013.

Research Student

University of Oxford (Merton College and Dept. of Theoretical Physics)

September 2002 – February 2003 | Oxford, United Kingdom

Thesis: Emergent gravity from strongly correlated quantum systems.

Supervisors: prof. dr. J.J. Binney FRS and dr. S. Sarkar.

Research Student

Kamerlingh Onnes Laboratory (Leiden University)

July 2001 – December 2001 | Leiden, The Netherlands

Thesis: Measuring the thermal conductivity of normal liquid ^3He in a restricted geometry.

Supervisor: dr. R. Jochemsen.

Internship

National Aerospace Laboratory NLR

January 1996 – December 1996 | Amsterdam, The Netherlands

Internship as electronics engineer responsible for developing parts of a test system for the Data Link Processor Unit and the Avionics Data Link Processor used in modern aircraft.

Acknowledgements

I would like to thank my promotor Dirk Bouwmeester for giving me the opportunity to pursue a doctorate in physics, especially after having spent many years in the corporate world. I equally would like to thank my parents for their everlasting patience and support.

With pleasure I have worked with several students, who all helped to shape our understanding of the toroidal helium plasmas. I would like to thank Timo Blom, Thom Boudewijn, Tim Kortekaas, Vasco Ramalho, Naor Scheinowitz, Daan van Seters, and Steven Zwaan.

As a teaching assistant for the quantum mechanics lectures series by Michiel de Dood and Peter Denteneer, I have enjoyed guiding many students, whose questions have in turn deepened my understanding of this topic.

I would like to thank Michiel de Dood, Wolfgang Löffler, and Martin van Exter for their support during my time in the Leiden Quantum Matter and Optics group.

After a few years of solitary labour, Felix Smits joined the search for toroidal plasmas and I would like to thank him for his efforts and expertise. He also managed to interest the Dutch Institute for Fundamental Energy Research, in particular Waldo Bongers, in our project, for which they made available most microwave components used in our experiments.

I would like to thank Chris Smiet for explaining the many aspects of his simulations of the self-organising knotted magnetic structures in plasma, and for the moments when we joined forces in the lab.

I am grateful for the pleasant cooperation and technical support from Harmen van der Meer from the fine mechanical department, and equally from Harry Visser, Ko Koning, Jos Disselhorst, and many others from the electronics department.

Finally, I would like to thank Jan Willem Dalhuisen for our numerous discussions on the foundational aspects of theoretical physics, which kept me sane during all those months of experimental work.

Casimir PhD series, Delft-Leiden 2021-01

ISBN 978-90-8593-467-7